

Constructing quantum many-body scar Hamiltonians from Floquet automata

Pierre-Gabriel Rozon, Department of physics,
McGill University, Montreal

A thesis submitted to McGill University
in partial fulfillment of the requirements of the degree of

Master of science

©Pierre-Gabriel Rozon

December 5, 2022

Contents

1	Introduction	10
2	Quantum scars	12
2.1	Definitions	12
2.1.1	Scarred eigenstates	12
2.1.2	Eigenstate thermalization hypothesis (ETH)	12
2.1.3	Entanglement entropy	15
2.2	The Bunimovich stadium	16
2.3	The PXP model	18
2.3.1	Forward scattering approximation	20
2.4	Proximity to integrability	22
2.4.1	Distribution of eigenvalues and relations to integrability	22
2.4.2	Proximity to integrability in the PXP model	23
2.5	Shiraishi-Mori embedded scar states	25
2.6	Connection to unstable classical orbits	28
2.7	Towers of scar states	31
3	Quantum cellular automata	35
3.1	Classical cellular automata	35
3.2	Quantum cellular automata	36
3.2.1	Concrete example of a quantum cellular automaton	39
3.2.2	Floquet driving and quantum cellular automata	40

4	Prethermalization	43
4.1	Generalized Gibbs ensemble	44
4.1.1	Quantum Newton’s cradle	44
4.2	Floquet prethermalization	46
5	QMBS from quantum cellular automata	49
5.1	Underlying cellular automaton and associated Hamiltonian	52
5.1.1	Physical setting	52
5.1.2	Eigenstates and eigenvalues of U_F	55
5.1.3	Local Hamiltonians from quantum cellular automata	56
5.1.4	Distinction between U_F and $e^{-i(A+B)}$	56
5.2	Rules that guarantee the presence of quantum scars	58
5.2.1	Writing H as a linear superposition of powers of simple unitary gates	58
5.2.2	Global rules	58
5.2.3	Local rules of type I	60
5.2.4	Local rules of type II	62
5.3	Building models that satisfy local rules	63
5.3.1	Explicit model search	63
5.3.2	PXP model	64
5.4	Numerical signature of quantum scars	64
5.4.1	Revival strength and signs of quantum scarring	64
5.4.2	R-statistic and effective Hilbert space dimension	67
5.5	BCH expansion and revivals	70
5.5.1	Amplitude of BCH terms and possible prethermal behavior in the PXP model	72
5.5.2	Prethermal behavior in the PXP model	73
5.5.3	BCH terms in the PXP model	77
5.5.4	PXP with and without phase	79
5.6	Discussion and outlook	79
5.7	Acknowledgements	83

6	Conclusion and outlook	84
A	Permutation and phase map representation	89
B	Total number of relevant rules	91
C	Decomposing Hamiltonian's in terms of powers of simple unitary matrices	93
D	QMBS-C as an embedded spectrum generating algebra	96
E	Symmetry sectors of QMBS-A/B	98
F	Exact PXP BCH terms	100
	F.0.1 Classification of the BCH terms	103
G	Closing condition for $h_{0,j}$	104
H	Spin representation of the models	106

List of Figures

3.1	Illustration of the time evolution of a classical cellular automaton	37
3.2	Illustration of the action of a local quantum cellular automaton	40
5.1	Structure of the quantum cellular automaton studied in this work, illustration of global rules and local rules of type I/II.	53
5.2	Illustration of the permutation nature of the gates U_0	54
5.3	Example of a cycle of length 4 produced by the quantum cellular automaton U_F	54
5.4	Illustration of the proof that local rules are sufficient for ensuring the embedding of common eigenstates.	61
5.5	Revivals of the Néel states in the model studied in this work as seen from the PR.	66
5.6	The maximum and minimum PR of the time evolved Néel states in the time range $t \in (10, 300)$ versus the effective Hilbert space dimension N_{eff}	68
5.7	Scatter plot of IPR vs. eigenstate energy	69
5.8	Non-integrability of model QMBS-A and QMBS-B as seen from the suppression of $P(r)$ at small r values.	70
5.9	Leakage from orbit states, characterized by $\ (I - P_0)C_n P_0\ $ and norm of the neglected terms C_n projected to the subspace of generic-states and orbit states.	75
5.10	PR of generic states evolved in time and time evolution of $ \langle Z_i(t) \rangle - \langle Z_i \rangle_{\text{m.c}} ^2$	76
5.11	Revivals seen in models with additional BCH terms C_n added to $A + B$	78
5.12	Overlap amplitude squared of $ \mathbb{Z}_2\rangle$ with $e^{(A+B)t} \mathbb{Z}_2\rangle$ for models where phase is trivial vs non-trivial.	80

List of Tables

5.1	Characteristics of the models	65
H.1	Spin representation of the models	107

Abstract

Most strongly interacting many-body quantum systems are expected to satisfy the eigenstate thermalization hypothesis (ETH), which is often used to justify the use of statistical mechanics to describe the thermal properties of quantum systems. However, the ETH does not always hold, and it is of great interest to identify the mechanisms responsible for such anomalies. In this work, by relating quantum cellular automata to Hamiltonian systems, a method is proposed to construct local many-body Hamiltonians that host predetermined high-energy states that do not thermalize in an otherwise thermalizing spectrum. This construction allows the identification of key mechanisms responsible for the emergence of quantum scars and provides insight into the mechanisms responsible for ETH breakdown in general. In particular, the method provides an intuitive explanation for the emergence of quantum scars in the well-known PXP model.

Abrégé

La plupart des systèmes quantiques à plusieurs corps qui interagissent fortement satisfont l'ETH (eigenstate thermalization hypothesis) qui est souvent utilisée pour justifier l'utilisation de la mécanique statistique pour décrire les propriétés thermales de systèmes quantiques. L'ETH n'est par contre pas toujours respectée. Une question de grand intérêt est alors de déterminer quels mécanismes sont responsables pour l'émergence de propriétés non-thermales observées au sein de certains systèmes quantiques. Dans ce travail, une méthode permettant de construire des systèmes quantiques Hamiltoniens qui pour lesquels il existe certains états quantiques prédéterminés ayant des propriétés non-thermales est proposée. La méthode est basée sur un lien établi entre les automates quantiques et les systèmes quantiques Hamiltoniens. De plus, cette construction permet d'identifier des mécanismes clés responsables de l'émergence de propriétés non-thermales en général. En particulier, la méthode permet d'expliquer les propriétés du modèle PXP qui est reconnu pour ses remarquables propriétés non-thermales.

Acknowledgments

First of all, I would like to thank my thesis advisor, Kartiek Agarwal, for his guidance throughout this journey through graduate school. His ideas and methods have truly shaped the way I solve complex physics problems and communicate my results in writing.

Next, I would like to thank my parents, my in-laws, my sisters, my godmother Nathalie and her husband Martin, my aunt Lize and my uncle Jacque, and finally my cousins Geneviève and Élizabeth who have always supported me in my relentless quest for physical truths. Their love and support is what gives me the strength to continue to pursue this goal, and I am forever grateful to them.

I would like to thank my friends Louis-Michael Duceppe, Anne-Sophie Lavoie, Émilie Levesque and Antoine Martel for the many fun outdoor escapades that give me the energy and peace of mind to pursue my research in this very demanding field.

Without any exaggeration, I could never have gotten where I am today without all the love and support I have received from my soul mate Camille Rose, who has been my life partner for as long as I can remember.

I would like to thank my friends Alexandre Caron, Carl Lévesque, Julien Leissner-Martin, Rémi Ligez, Eugène Sanscartier, Audrey Masse, François-Olivier Gagnon-Bistodeau and Valérie Monette who have been my partners in crime during all these years. I am grateful for the many restaurants, bars, study sessions, projects, sports, chess games and many other things we did together that really broke the monotony of a life that would otherwise have

consisted of an inadequate work/fun ratio.

Finally, I would like to acknowledge the support of my friends Brett Min, Ivan Martinez, and Bill Truong, with whom I shared the online graduate school experience during the Covid 19 pandemic.

Chapter 1

Introduction

Reprinted excerpt with permission from Pierre-Gabriel Rozon, Michael J. Gullans, and Kartiek Agarwal. Constructing quantum many-body scar hamiltonians from floquet automata, Volume number 106, Page number 184304, Nov 2022. [52]. Copyright (2022) by the American Physical Society. Understanding how thermalization arises from unitary evolution remains a fundamental challenge in the study of non-equilibrium quantum dynamics. The Eigenstate Thermalization Hypothesis [14, 61] (ETH) postulates that eigenstates of many-body quantum systems themselves encode thermal correlations when viewed by a local observer. Although ETH has been numerically verified in a wide variety of quantum systems [50, 49, 30], several important exceptions are known that challenge its associated dogma. The most prominent of these are integrable systems which occur in models with fine-tuned parameters [62], and many-body localized systems [6, 47, 45, 3] where more robust local integrals of motion [26] emerge due to strong disorder. These systems exhibit a lack of level repulsion at all energies, a hallmark of non-ergodicity, and have certain persistent quantum correlations [31, 55, 59].

More recently, an experiment in a chain of Rydberg atoms found dramatic revivals in many-body quantum correlations after apparent relaxation, only when the system is initialized in *specific states* [7]. It is now understood that certain quantum systems can break ergodicity weakly [64], by only violating the ETH over a sub-extensive number of eigenstates. These systems have been dubbed quantum many-body scars [63] (QMBS), generalizing the phenomenon well known in the single-particle setting [23]. Since the initial findings, low

entanglement eigenstates in the middle of the spectrum have been discovered in well known models [41, 2] and a number of theoretical proposals for constructing new QMBS Hamiltonians have been put forth, with the aid of spectrum generating algebras [42, 37, 13, 46], projective constructions [58], matrix product state representations [25], among others; see Ref. [40] for a more exhaustive list of references.

Crucially, these proposals yield Hamiltonians where the scar eigenstates are known *exactly*. These scar eigenstates appear in group of degenerate eigenstates called *towers*, where adjacent towers are separated in energy by the same amount ΔE . Low entanglement states can generally be constructed from these scar eigenstates and are seen to exhibit perfect revivals in correlations with a period $T \sim 1/\Delta E$ indefinitely. This is in contrast to the experimentally motivated PXP model [64, 63, 56] which hosts approximate scar eigenstates and in which many body revivals decay over a long but finite duration. The corresponding scar towers are only approximately equidistant in energy, implying that low entanglement states obtained from a superposition of scarred eigenstates don't show perfectly regular revivals due to slow dephasing. Although weak perturbations may be added to exact QMBSs to obtain such a decay of revivals, it remains a challenge to explain the existence of QMBS Hamiltonians such as the PXP model that have no small parameter, as well as uncover what sets the timescale for the decay of quantum revivals.

In this work, we illustrate general principles to derive (both exact and approximate) QMBS *Hamiltonians* without any small parameters, starting from Floquet automaton (*unitary*) *circuits*, and show how a timescale for the decay of revivals naturally emerges in this setting.

Chapter 2

Quantum scars

2.1 Definitions

2.1.1 Scarred eigenstates

At present, there is no univocal definition of scarred eigenstates, which makes their identification and discussion ambiguous. They do, however, share a common property: they all violate the predictions of the ETH (in other words, they have anomalous properties that contradict what one would expect from a typical thermal state). Using this fact, scarred eigenstates are referred to in this work as any excited eigenstate with anomalous thermal properties that cannot be explained from the presence of symmetries in the system (some examples are given in the following sections). In general, scarred eigenstates are detected in a given symmetry sector of the model using metrics such as entanglement entropy, or by comparing expected thermal averages to averages obtained from the high-energy eigenstate suspected to be a scarred eigenstate. Before presenting examples of quantum scars, we provide a more formal definition of the ETH and entanglement entropy, as these concepts are essential for understanding and detecting the presence of scarred eigenstates.

2.1.2 Eigenstate thermalization hypothesis (ETH)

The eigenstate thermalization hypothesis (ETH) is a set of ideas that were designed to justify the use of statistical equilibrium mechanics to describe isolated quantum systems. Consider

a Hamiltonian H describing a quantum system with a finite Hilbert space of dimension d^L for some constant d , as well as a complete basis for this Hamiltonian $|E_\alpha\rangle$ such that

$$H |E_\alpha\rangle = E_\alpha |E_\alpha\rangle, \quad (2.1)$$

where E_α is the eigenvalue of the eigenstate $|E_\alpha\rangle$. L here will be referred as the size of the system. Further assume that there is no degeneracy and that there is a finite number of eigenstates. From there, one can write down any quantum-mechanical observable A in the eigenstate basis

$$A_{\alpha,\beta} = \langle E_\alpha | A | E_\beta \rangle \quad (2.2)$$

Starting from a generic state at time $t = 0$ given by

$$|\psi(0)\rangle = \sum_{\alpha} c_{\alpha} |E_{\alpha}\rangle \quad (2.3)$$

and assuming that the energy uncertainty ΔE of the state is algebraically small in L where $(\Delta E)^2 = \sum_{\alpha} |c_{\alpha}|^2 (E_{\alpha} - \bar{E})^2$ and $\bar{E} = \sum_{\alpha} |c_{\alpha}|^2 E_{\alpha}$ (this restriction ensures that the state is not a quantum superposition of distinct macro-states), one can compute the long-time average value of the observable A which is given by

$$\bar{A} = \lim_{\tau \rightarrow \infty} \frac{1}{\tau} \int_0^{\tau} \langle \psi(t) | A | \psi(t) \rangle dt \quad (2.4)$$

For a time independent Hamiltonian, $|\psi(t)\rangle$ is simply given by

$$|\psi(t)\rangle = \sum_{\alpha} c_{\alpha} e^{-iE_{\alpha}t} |E_{\alpha}\rangle \quad (2.5)$$

Here \hbar is taken to be 1 throughout this work. Replacing equation 2.5 into equation 2.4, one obtains

$$\bar{A} = \sum_{\alpha=1}^N |c_{\alpha}|^2 A_{\alpha\alpha} + \frac{1}{2} \lim_{\tau \rightarrow \infty} \left[\sum_{\alpha \neq \beta}^N \frac{ic_{\alpha}^* c_{\beta} A_{\alpha\beta}}{E_{\beta} - E_{\alpha}} \left(\frac{e^{-i(E_{\beta} - E_{\alpha})\tau} - 1}{\tau} \right) + \text{h.c} \right], \quad (2.6)$$

where N denotes the Hilbert space dimension. The second term of equation 2.6 goes to 0 and one is left with

$$\bar{A} = \sum_{\alpha=1}^N |c_{\alpha}|^2 A_{\alpha,\alpha} \quad (2.7)$$

This result is problematic since it depends on the coefficients c_α which determine the initial state, whilst the micro-canonical average (the average over all the eigenstates lying in an energy window W centered around the average energy $\bar{E} = \langle \psi | H | \psi \rangle$) yields

$$\langle A \rangle_{\text{mc}, \bar{E}, W} = \frac{1}{N_W} \sum_{E_{\alpha'} \in [\bar{E}-W, \bar{E}+W]} A_{\alpha'\alpha'} \quad (2.8)$$

which is devoid of any connection to an initial state. In the above equation, N_W refers to the number of eigenstates lying within the energy window $[\bar{E} - W, \bar{E} + W]$.

To solve this apparent paradox, the ETH postulates conditions on $A_{\alpha,\alpha'}$ designed to ensure that equation 2.8 and 2.7 yield the same result up to fluctuations that decay exponentially with system size as well as ensuring that the time dependant average $\langle \psi(t) | A | \psi(t) \rangle$ relaxes towards 2.8 up to exponentially small corrections. A sufficient set of conditions is to ask that 1) the diagonal matrix elements $A_{\alpha,\alpha}$ are a smooth function of E_α , with the distance between adjacent diagonal terms decaying exponentially with system size and 2) that the off-diagonal matrix elements of $A_{\alpha,\beta}$ decay exponentially with the energy difference $|E_\alpha - E_\beta|$.

Intuitively, the first condition ensures that the operator A does not fluctuate much in a given energy window. The second condition ensures that the operator A does not have large matrix elements connecting states that are widely separated in energy (this condition is there to ensure relaxation). Under the restrictions 1), one obtains

$$\bar{A} = \sum_{\alpha=1}^N |c_\alpha|^2 A_{\alpha\alpha} \approx A_{i,i} \quad \sum_{E_\alpha \in [\bar{E}-W, \bar{E}+W]} |c_\alpha|^2 \approx A_{i,i} \quad (2.9)$$

$$\langle A \rangle_{\text{mc}, \bar{E}, W} = \frac{1}{N_W} \sum_{E_{\alpha'} \in [\bar{E}-W, \bar{E}+W]} A_{\alpha'\alpha'} \approx \frac{1}{N_W} \sum_{E_{\alpha'} \in [\bar{E}-W, \bar{E}+W]} A_{i,i} = A_{i,i}, \quad (2.10)$$

where exponentially small corrections have been neglected and the index i is chosen such that $E_i \approx \bar{E}$. The energy window W is chosen large enough such that the $|c_\alpha|$ have most of their weight within the range $[\bar{E} - W, \bar{E} + W]$. Furthermore, one may show that

$$\overline{(\langle \psi(t) | A | \psi(t) \rangle - \bar{A})^2} = \sum_{\alpha \neq \alpha'} |c_\alpha| |c_{\alpha'}| A_{\alpha,\alpha'} \quad (2.11)$$

which, using condition 2), decays exponentially with system size. These results show that the two averages are now in agreement under the assumptions from ETH, and that the system relaxes towards the micro-canonical ensemble. It turns out, these conditions are in fact satisfied for most isolated quantum systems provided that the operator A only involves a small number of particles/system constituents (the operator need not be local, e.g the occupation number of a given momentum mode is an example of a non-local operator expected to satisfy the ETH criterion given a non-integrable Hamiltonian H). Although the ETH appears to be a reasonable set of assumptions to make about a strongly interacting many-body system, a growing number of exceptions have renewed interest in issues related to thermalization and chaos, especially in isolated quantum systems. Note that under the ETH assumptions, it has been showed above that thermal averages may be extracted from a single matrix element, i.e a single eigenstate. This directly implies that the eigenstates themselves should appear as thermal states themselves. Using this fact, one may then detect violations of the ETH by searching for the the presence of eigenstates with non-thermal properties, or alternatively one may search for excited states with unusual dynamical properties. Several examples of such anomalies will be discussed in the following sections.

2.1.3 Entanglement entropy

The entanglement entropy may be interpreted as a tool to measure the amount of quantum correlations (entanglement) between sub-regions of a wave-function. To compute the entanglement entropy between a region \mathcal{A} of a system and it's complement \mathcal{A}^c , one writes down the Schdmit decomposition of the wave-fuction $|\psi\rangle$, i.e

$$|\psi\rangle = \sum_{m=1}^{\alpha} \lambda_m |\psi_m\rangle_A |\psi_m\rangle_{A^c}. \quad (2.12)$$

The states $|\psi_m\rangle_A, |\psi_m\rangle_{A^c}$ form a basis for the region A and it's complement A^c respectively. The index α is known as the Schdmit rank. The λ_m are the Schdmit coefficients and they satisfy the relation $\sum_{m=1}^{\alpha} \lambda_m^2 = 1$ provided the state $|\psi\rangle$ is normalized. The von Neumann entropy $S_{\mathcal{A}}$ of the sub-region \mathcal{A} is defined as

$$S_{\mathcal{A}} \equiv - \sum_{m=1}^{\alpha} \lambda_m^2 \log \lambda_m^2 = - \text{Tr } \rho_{\mathcal{A}} \log \rho_{\mathcal{A}} \quad (2.13)$$

Note that it is clear from this definition that the entanglement entropy of the sub-region \mathcal{A}^c yields the same result. In the above equation, $\rho_{\mathcal{A}}$ is the reduced density matrix over the sub-region \mathcal{A} . The von Neumann entropy is a very versatile object, with multiple uses in various domains of condensed matter physics [16]. For instance, it is well known that the ground states of gapped quantum many-body systems usually satisfy an area law, which is to say that the von Neumann entropy scales as the boundary of the region \mathcal{A} , so in $2D$ it scales as the perimeter, in $3D$ it scales as the surface, etc. Moreover, it may be showed from the above discussion about the ETH that for generic non-integrable models, the excited states of the systems are expected to follow a volume law, i.e the von Neuman entropy scales as the volume of the region \mathcal{A} . As a consequence, the von Neumann entropy provides a natural tool for detecting the presence of quantum scars, i.e high energy eigenstates that have a von Neumann entropy that scales slower than a volume-law may be identified as scarred eigenstates. Such states are easily identified when the von Neuman entropy of all the eigenstates of the system is plotted against energy, in which case the scarred eigenstates will appear to have low von Neumann entropy when compared to other eigenstates with similar energy.

2.2 The Bunimovich stadium

As a first example of quantum scars, consider the Bunimovich stadium [10] which is a classical system describing a single particle bouncing elastically off the boundaries of a “billiard table” that has the shape of a stadium, see Box 1 in [10]. It has been demonstrated that this classical system is ergodic, which implies that if the particle is initiated in any state (except for an infinitesimal set of states corresponding to unstable orbits), then its trajectory will explore uniformly the whole phase space. The exact mathematical meaning of “unstable periodic orbits” is not crucial for the discussion here. Within the context of the Bunimovich stadium, an “unstable periodic orbit” refers here to a trajectory in phase space that follows a periodic orbit instead of exploring uniformly the entire phase space (i.e instead of being ergodic), but such that an infinitesimal change of the initial conditions is enough to render the trajectory ergodic. An example of such an unstable periodic orbit would be a particle initiated in the

middle of the stadium with a velocity that is perfectly vertical, in which case the particle remains indefinitely on a single vertical line, bouncing up and down forever. However, if the initial velocity deviates only slightly from being perfectly vertical, then the particle starts to bounce erratically and it eventually explores the entire phase space uniformly. This is what is showed in Box 1 of [10] panel **b**), which shows that a small deviation of the direction of the velocity induces erratic bounces. If the simulation had been run for a longer time, the trajectory would have started to look like the trajectory showed in Box 1 of [10] panel **a**).

The quantization of classically chaotic systems such as the Bunimovich stadium usually produces a quantum system that exhibits strong energy level repulsion (which is usually associated with non-integrability and thermal behavior, this is discussed in more depth in section 2.4), in addition to producing thermal eigenstates devoid of any structure (their probability density should appear approximately uniform throughout the phase space). It turns out, however, that the story is quite different when it comes to systems such as the Bunimovich stadium, which host anomalous eigenstates that exhibit a significant increase in probability density around certain trajectories in phase space [23], which happen to correspond with unstable periodic orbits of the underlying classical system. Such a phenomenon is an example of quantum scarring.

Quantum scarring in this system can be observed dynamically. For instance, by initiating a Gaussian wave-packet near an unstable classical orbit (e.g initiating the wave-packet with a velocity directed upward, and with an average position centered in the middle of the stadium, see Box 1 in [10] panel **b**)), one observes revivals in the sense that the quantum state tends to return to its initial state. In contrast, a Gaussian wave-packet initiated far from these unstable orbits does not exhibit such revivals. This is illustrated in Box 1 in [10], panel **e**) which shows the auto-correlation of two wave-packets, one that starts near an unstable classical orbit (blue curve) and one that doesn't (red curve).

The presence or absence of revivals for a given Gaussian wave-packet can be attributed to its spectral decomposition. Box 1 in [10], panel **f**) illustrates the spectral decomposition

of both a wave-packet initiated near an unstable orbit (blue curve) and another initiated in a configuration far from an unstable orbit (red curve). The blue curve shows that the weight is concentrated on eigenstates that are approximately equidistant in energy, while the red curve shows a more uniform spectral decomposition. As one will observe in the next sections, the appearance of scarred eigenstates that are approximately equidistant in energy is a recurring phenomenon in the many-body setting as well (scar-like phenomena in many-body quantum systems).

Finally, quantum scarring can also be noticed by looking at properties of the eigenstates themselves. For instance, scar eigenstates should deviate from the expected uniform probability density over the whole of phase space. Such a deviation is depicted in Box 1 in [10] panel **d**) which shows an eigenstate with a clear increase in probability density near an unstable orbit (as defined above). This is in contrast to typical eigenstates that appear to be a random superposition of plane waves, as depicted in Box 1 in [10] panel **c**).

One might be thinking at this point that the presence of scarring in the Bunimovich stadium is merely a consequence of the fact that only one particle is involved, and that a generalization of the scarring phenomenon to the many-body setting is hopeless due to interactions which arguably make the system “more” chaotic. The next section shows that the reality is otherwise. Indeed, even in the presence of strong interactions, there is a possibility for the emergence of quantum scars.

2.3 The PXP model

One of the most striking examples of a many-body quantum scar comes from recent experiments on arrays of Rydberg atoms. The particular system presented in this section hosts special scarred eigenstates which, similarly to the Bunimovich stadium, are approximately equidistant in energy.

Rydberg arrays are composed of atoms that can, under the right restrictions, be modeled as

particles residing in a Hilbert space composed of two states, $|\circ\rangle, |\bullet\rangle$ which respectively denotes the ground state and a highly excited state of the atom. The atoms can be subjected to a microwave field that induces Rabi-oscillations between the two states $|\circ\rangle, |\bullet\rangle$. If the atoms are placed in close proximity, the configurations composed of neighboring excited states $|\bullet, \bullet\rangle$ are energetically unfavorable due to the repulsive Van der Waal interactions resulting from the overlapping of the enhanced electron cloud of the excited atoms (this is known as the Rydberg blockade). This effectively enforces a dynamical constraint on the system, allowing a Rydberg atom to oscillate between $|\bullet\rangle$ and $|\circ\rangle$ only if the two neighboring atoms are in the $|\circ\rangle$ state.

Now consider states such as

$$|\mathbb{Z}_k\rangle = |\underbrace{\bullet \circ \dots \circ}_k \underbrace{\bullet \circ \dots \circ}_k \dots\rangle. \quad (2.14)$$

It has been observed in [7] that the dynamics of states such as $|\mathbb{Z}_2\rangle \equiv |\circ \bullet \circ \dots\rangle$ and $|\mathbb{Z}_3\rangle \equiv |\bullet \circ \circ \dots\rangle$ has revivals instead of relaxing exponentially fast to a thermal state, as can be seen in figure 6 of [63]. Most other blockade free states were observed to relax to thermal states, suggesting the existence of many-body quantum scars in an otherwise chaotic system. Furthermore, these special non-thermal states do not correspond to low energy excitations, ruling out this possible explanation for the unusual revivals. Projecting the full Hamiltonian onto the subspace of blockade free states, one obtains the celebrated PXP model

$$H_{\text{PXP}} = \sum_j P_{j-1} X_j P_{j+1} \quad (2.15)$$

where X_j induces a transition between the $|\bullet\rangle_j, |\circ\rangle_j$ states and captures the Rabi-oscillations. The projectors are given by $P_j = I - Z_j$ with $Z_j = |\bullet\rangle_j \langle \bullet|_j - |\circ\rangle_j \langle \circ|_j$. The structure of the projector ensures that the blockade constraint is satisfied.

Many different observables can be used to detect the presence of non-thermal behavior. For example, one can study the overlap of eigenstates of H_{PXP} with the $|\mathbb{Z}_2\rangle$ state. Figure 3 panel **b)** of [63] shows the presence of eigenstates exhibiting anomalously large overlap with the $|\mathbb{Z}_2\rangle$ state, which is surprising as one would expect the high energy eigenstates of H_{PXP}

to be thermal states (they should be approximately uniform superposition of blockade free states, analogously to the Bunimovich stadium thermal eigenstates, which are uniform superposition of plane waves). The anomalous eigenstates can also be detected by computing their half-chain entanglement entropy. This is illustrated in figure 3 panel **a**) of [63] which shows several excited states in the middle of the spectrum with low entanglement entropy. Such states simultaneously have a low half-chain entanglement and a large overlap with the $|\mathbb{Z}_2\rangle$ state.

2.3.1 Forward scattering approximation

The scarred eigenstates can be approximated using a method called forward scattering approximation (FSA). See [63] for an in-depth application of this method to the PXP model. The FSA is based on the Lanczos algorithm which is used to find an orthonormal basis of some given Krylov subspace. Krylov subspaces are defined as follows

$$\mathcal{K}_k(H, v) = \text{span} \left\{ v, Hv, \dots, H^{k-1}v \right\} \quad (2.16)$$

for a given initial state v and an integer k . Here H represents an arbitrary Hamiltonian matrix. The Lanczos algorithm is defined as follows

$$\beta_{i+1}v_{i+1} = Hv_i - \alpha_i v_i - \beta_i v_{i-1}, \quad i = 1, \dots, k \quad (2.17)$$

where β_{i+1} is chosen such that $\|v_{i+1}\|^2 = 1$ and α_i is equal to $(Hv_i)^\dagger \cdot v_i$. In matrix form, the algorithm reads

$$HV_k = V_k T_k + \beta_{k+1} v_{k+1} e_k^T \quad (2.18)$$

where $V_k = [v_1, \dots, v_k]$, $e_k^T = (0, 0, 0, \dots, 1)$ and the matrix T_k is given by

$$T_k = \begin{bmatrix} \alpha_1 & \beta_2 & & & \\ \beta_2 & \ddots & \ddots & & \\ & \ddots & \ddots & \beta_k & \\ & & & \beta_k & \alpha_k \end{bmatrix} \quad (2.19)$$

The v_i form an orthonormal basis of the Krylov subspace, and it can be shown that the eigenvectors of T_k can be used to construct eigenvectors of H provided that the Krylov

subspace closes on itself once the integer k is reached in equation 2.16. Indeed, one has that 2.18 can be rewritten as follows

$$V_k^\dagger H V_k = T_k \quad (2.20)$$

which comes from the fact that $V_k^\dagger V_k = I_k$ and the orthogonality of the v_i . Suppose now that x is an eigenstate of T_k with eigenvalue λ , and define $y = V_k x$. Given those conditions, one has that

$$H V_k x = V_k V_k^\dagger H V_k x = V_k T x = \lambda V_k x \quad (2.21)$$

which shows that $V_k x$ is an eigenstate of H . Note that $V_k V_k^\dagger$ is an orthogonal projector onto span V_k , not the identity matrix on the entire Hilbert space, which explains why the Kyrlov subspace closure condition is essential. Thus, by computing the elements of the matrix T_k , which will produce a k by k tridiagonal matrix, one can extract eigenstates and eigenvalues of H . Now consider the PXP Hamiltonian H_{PXP} and its decomposition into a forward and backward propagating part $H_{\text{PXP}} = H_{\text{PXP}}^+ + H_{\text{PXP}}^-$

$$H_{\text{PXP}}^\pm = \sum_{j \in \text{even}} P_{j-1} \sigma_j^\pm P_{j+1} + \sum_{j \in \text{odd}} P_{j-1} \sigma_j^\mp P_{j+1} \quad (2.22)$$

in analogy to the paramagnet Hamiltonian for which

$$H_X^\pm = \sum_{j \in \text{even}} \sigma_j^\pm + \sum_{j \in \text{odd}} \sigma_j^\mp, \quad H_X = \sum_i X_i \quad (2.23)$$

In the case of the para-magnet, using the state $|\mathbb{Z}_2\rangle$ to construct a Kyrlov subspace generates a closed subspace composed of $L + 1$ states, where L is the size of the system. Moreover, it can be shown that the Lanczos algorithm simplifies to

$$\beta_{j+1} v_{j+1} = H_X^+ v_j \quad (2.24)$$

The resulting T_k matrix turns out to be the $2S^x$ operator for a spin of size $L/2$, which produces $L + 1$ evenly spaced eigenvalues.

$$T_{L+1} = \begin{pmatrix} 0 & \beta_2 & & & \\ \beta_2 & 0 & \beta_3 & & \\ & \beta_3 & 0 & \ddots & \\ & & \ddots & \ddots & \beta_{L+1} \\ & & & \beta_{L+1} & 0 \end{pmatrix} \quad \beta_{j+1} = \sqrt{j(L-j+1)} \quad (2.25)$$

Turning to the PXP model, one could go on and try to obtain a closed Krylov subspace from the state $|\mathbb{Z}_2\rangle \equiv |\circ\bullet\dots\rangle$. It turns out however that the Krylov subspace does not close after $L + 1$ steps, and the integer k required for the Krylov subspace to close can be extremely large. The FSA then consists in neglecting the backward propagating part (H_{PXP}^-), which amounts to applying the recursion relation given in 2.24 to the PXP model, even if it is not satisfied exactly. This still produces a set of orthonormal vectors since H_{PXP}^+ always increases the Hamming distance from the state $|\mathbb{Z}_2\rangle$. The recursion ends after $L + 1$ steps as in the case of the para-magnet and produces a corresponding T_{L+1} matrix. The eigenvalues and eigenvectors of this matrix yield a set of approximate eigenvectors and eigenvalues of H_{PXP} that approximate the observed scarred eigenstates. The error resulting from the FSA can be estimated from $[H_{\text{PXP}}^+, H_{\text{PXP}}^-]$ and is discussed thoroughly in [63].

The fact that scarring is observed only for very specific states bears some resemblance to the single quantum particle confined in the Bunimovich stadium. Indeed, in both cases, it seems that the initial conditions are crucial to observe the scars. In the case of a single particle, the scarring behavior comes from the proximity to an unstable classical orbit. It is therefore natural to ask whether similar analogies can be drawn from the many-body case by relating the scars to an underlying classical orbit. It turns out that such a connection can be made and will be discussed in section 2.6.

2.4 Proximity to integrability

2.4.1 Distribution of eigenvalues and relations to integrability

It is well known that in models that lack symmetries, the distinct energy levels tend to repel each other. This simple observation can be leveraged to develop a method for determining if a given model is integrable or not based on the statistics of the energy levels. Indeed, if one defines an energy spacing distribution $p(s)$, which yields the probability density for two consecutive levels to have an energy difference of s , then provided the model is non-integrable, $p(s)$ is known to follow a Wigner-Dyson distribution [5]. However, this prediction for the

probability distribution $p(s)$ assumes a flat density of states in the vicinity of the levels, which requires an unfolding of the spectrum at hand when it is discrete, which can be difficult to implement reliably. To avoid this issue, one can consider instead the level spacing ratios. Given a set of eigenvalues E_n , $E_n \leq E_{n+1}$ associated with eigenstates within a symmetry sector of the Hamiltonian, then r_n is defined as $r_n = \min(\Delta E_{n+1}/\Delta E_n, \Delta E_n/\Delta E_{n+1})$ where $\Delta E_n = E_n - E_{n-1}$. The probability distribution $p(r)$ has the advantage of not requiring an unfolding of the spectrum and can be computed directly from the discrete spectrum. It is known that in thermal systems, the average value of the set of r_n flows with system size to the GUE ensemble (Gaussian unitary ensemble) average value of 0.6 when time reversal symmetry is broken, and tends towards the GOE (Gaussian orthogonal ensemble) average of 0.53 if time reversal symmetry is respected. For integrable systems, the eigenvalues don't repel and the average value of the set r_i flows towards the average value associated with the Poisson ensemble (POI) of 0.39.

2.4.2 Proximity to integrability in the PXP model

A mechanism that can be responsible for the emergence of quantum scars is proximity to a parent integrable model. This section provides a summary of the results presented in [29] where small deformations of the PXP model have been shown to make it “more” integrable (more in the sense that the distribution of the energies of the system becomes closer to being a Poisson rather than being closer to a Wigner-Dyson distribution), which hints at the possibility that the PXP model might have a close parent integrable model responsible for the emergence of scarred eigenstates.

The symmetries of the PXP model H_{PXP} are anti-commutation with the operator $\mathcal{P} = \prod_{j=1}^L Z_j$, time reversal symmetry and spatial inversion symmetry about the center bond. There is a total of 11 independent range-four operators in the blockade-free subspace given

by [29]

$$\begin{aligned}
& \sum_j Z_j, \quad \sum_j Z_j Z_{j+2}, \quad \sum_j Z_j Z_{j+3} \\
& \sum_j P_{j-1} X_j P_{j+1} \quad \sum_j P_{j-1} Y_j P_{j+1} \quad \sum_j P_{j-1} X_j P_{j+1} Z_{j+2} \\
& \sum_j Z_{j-2} P_{j-1} X_j P_{j+1} \quad \sum_j P_{j-1} Y_j P_{j+1} Z_{j+2} \quad \sum_j Z_{j-2} P_{j-1} Y_j P_{j+1} \\
& \sum_j P_{j-1} S_j^+ S_{j+1}^- P_{j+2} \quad \sum_j P_{j-1} S_j^- S_{j+1}^+ P_{j+2}
\end{aligned} \tag{2.26}$$

and a natural choice of deformation which was inspired by the intuition that the above symmetries are an essential ingredient for the emergence of quantum scars, is the deformation [29]

$$\sum_j h_{XZ} (P_{j-1} X_j P_{j+1} Z_{j+2} + Z_{j-2} P_{j-1} X_j P_{j+1}) \tag{2.27}$$

which is the only choice that satisfies all symmetries of the PXP model.

Furthermore, one can add a perturbation that breaks the time reversal symmetry (which here is just complex conjugation) in order to illustrate in a two-dimensional phase diagram the contrast between regions where the model is close to being integrable versus regions where it is not. Thus, one can study the following family of models [29]

$$\begin{aligned}
H = H_0 - \sum_j h_{XZ} (P_{j-1} X_j P_{j+1} Z_{j+2} + Z_{j-2} P_{j-1} X_j P_{j+1}) \\
- h_{YZ} (P_{j-1} Y_j P_{j+1} Z_{j+2} + Z_{j-2} P_{j-1} Y_j P_{j+1}).
\end{aligned} \tag{2.28}$$

where H_0 is the usual PXP model and h_{XZ}, h_{YZ} are free parameters. The proximity of the models to an integrable point for given values of h_{XZ} and h_{YZ} is assessed by computing the level statistics. In [29], the average value of the r_i is computed for various values of h_{YZ} and h_{XZ} and it is found that the level statistics are closest to a Poisson distribution when $h_{YZ} = 0$ and $h_{XZ} = -0.02$, as can be observed in figure 1 of [29]. The close proximity of the PXP model to a system that is nearly integrable suggests that the PXP scars might be a result of this proximity. Section 5.5 shows how terms similar to 2.27 can be derived for the PXP model by making use of the methods developed in this work.

2.5 Shiraishi-Mori embedded scar states

Another method for constructing QMBS is to explicitly embed non-thermal eigenstates into an otherwise chaotic Hamiltonian. This method is due to Shiraishi and Mori [58]. A description of the method and some examples are presented in this section. Section 5.3 presents a system (dubbed QMBS-C) that hosts embedded scar eigenstates. This model was constructed using the method presented in this work.

Consider a quantum system on a discrete set of lattice sites labeled by j and P_j a set of local projectors acting on a neighborhood of the lattice site j . Given a Hilbert space \mathcal{H} , one can define a subspace $\mathcal{T} \subset \mathcal{H}$ of dimension d spanned by a set of d orthonormal states $|\Psi_\alpha\rangle \in \mathcal{H}$, $\alpha \in \{1, 2, \dots, d\}$ which satisfy

$$P_j |\Psi_\alpha\rangle = 0 \quad (2.29)$$

This subspace is the one that the Shiraishi-Mori method aims at embedding. Consider now a Hamiltonian H' that satisfies $[H', P_j] = 0$ for all j . Further define a set of local Hamiltonians h_j that can be chosen arbitrarily. From there, one can then construct the following Hamiltonian [58]

$$H = \sum_j P_j h_j P_j + H' \quad (2.30)$$

The key feature of this Hamiltonian is that it preserves the subspace \mathcal{T} . To see this, one can show that the Krylov subspace generated by H remains in \mathcal{T} if the starting state v used to generate the Krylov subspace is an element of \mathcal{T} .

Recall that the Krylov subspace is defined as

$$\mathcal{K}_k(H, v) = \text{span} \left\{ v, Hv, H^2v, \dots, H^{k-1}v \right\} \quad (2.31)$$

where k is assumed here to be large enough so that the Krylov subspace closes on itself. Let's now show that any vector that appears in this Krylov subspace is contained in \mathcal{T} . It is easy to see that a sufficient condition for this property to be satisfied is to have that

$P_j H |\Psi_\alpha\rangle = 0$ for all states $|\Psi_\alpha\rangle \in \mathcal{T}$. By expanding $P_j H |\Psi_\alpha\rangle$ one obtains

$$P_j H |\Psi_\alpha\rangle = \sum_k P_j P_k h_k P_k |\Psi_\alpha\rangle + P_j H' |\Psi_\alpha\rangle = H' P_j |\Psi_\alpha\rangle = 0 \quad (2.32)$$

which shows that the Krylov subspace is contained in \mathcal{T} . One can further see that the dynamical properties of the states within the subspace \mathcal{T} are fully determined by H' . Indeed,

$$e^{-i(\sum_j P_j h_j P_j + H')t} |\Psi_\alpha\rangle = \sum_n \frac{(At - iH't)^n}{n!} |\Psi_\alpha\rangle = \sum_i \frac{(-iH't)^n}{n!} |\Psi_\alpha\rangle = e^{-iH't} |\Psi_\alpha\rangle \quad (2.33)$$

where $A = -i \sum_j P_j h_j P_j$. This identity follows from the fact that any product of powers of A and $-iH't$ containing at least one A will vanish when acting on $|\Psi_\alpha\rangle$, and thus only powers composed exclusively of H' remain. From there, we see that if the model H' has non-thermal eigenstates within \mathcal{T} (for instance, H' might be an integrable model), then such states are automatically eigenstates of H and will appear as scar eigenstates in an otherwise thermalizing spectrum (since the full H can always be made non-integrable due to the freedom in the choice of h_j), and will thus violate the ETH. Let's now consider an example of an embedding that was constructed in [58]

Assume a chain of L spins $1/2$ with site index $j \in (1, 2, \dots, L)$ and periodic boundary conditions. Local spin operators are denoted $\vec{S}_j = (S_j^x, S_j^y, S_j^z)$ and the total spin operator of three consecutive spins centered at j is given by

$$\vec{S}_j^{\text{tot}} = \vec{S}_{j-1} + \vec{S}_j + \vec{S}_{j+1} \quad (2.34)$$

The total spin operator squared $(\vec{S}_j^{\text{tot}})^2$ has two eigenvalues, $3/4$ and $15/4$ for the quantum numbers $l = 1/2$ and $l = 3/2$ respectively. Let's now construct an operator that has an eigenvalue of 0 when acting on an $l = 1/2$ state and an eigenvalue of 1 when acting on an $l = 3/2$ state (the projector onto the $l = 3/2$ sector). This yields

$$P_j = \frac{1}{3}((\vec{S}_j^{\text{tot}})^2 - 3/4) \quad (2.35)$$

Using the fact that $(\vec{S}_j^{\text{tot}})^2 = \vec{S}_{j-1}^2 + \vec{S}_j^2 + \vec{S}_{j+1}^2 + 2(\vec{S}_{j-1} \cdot \vec{S}_j + \vec{S}_{j-1} \cdot \vec{S}_{j+1} + \vec{S}_j \cdot \vec{S}_{j+1}) = 9/4 + 2(\vec{S}_{j-1} \cdot \vec{S}_j + \vec{S}_{j-1} \cdot \vec{S}_{j+1} + \vec{S}_j \cdot \vec{S}_{j+1})$ and replacing in the above equation, one obtains

$$P_j = \frac{2}{3} \left(\vec{S}_{j-1} \cdot \vec{S}_j + \vec{S}_j \cdot \vec{S}_{j+1} + \vec{S}_{j-1} \cdot \vec{S}_{j+1} \right) + \frac{1}{2} \quad (2.36)$$

The Hamiltonian composed of such projectors on all sites j will have for ground states the states that locally minimize all the projectors, i.e states such that $(\vec{S}_j^{\text{tot}})^2 = 3/4$ on all group of 3 adjacent spins. It is known that only two such states exist [11], and are given by

$$|\Psi_1\rangle \equiv \bigotimes_{n=1}^{L/2} |v_{2n-1,2n}\rangle, \quad |\Psi_2\rangle \equiv \bigotimes_{n=0}^{L/2-1} |v_{2n,2n+1}\rangle \quad (2.37)$$

with

$$|v_{i,j}\rangle \equiv \frac{1}{\sqrt{2}} \left(|\uparrow\rangle_i |\downarrow\rangle_j - |\downarrow\rangle_i |\uparrow\rangle_j \right) \quad (2.38)$$

These states are easily seen to be ground states by considering any groups of 3 adjacent spin 1/2. For all such group, one always has that two of the spins form a singlet pair which implies that the three spins together can only form a total spin-1/2 state which is always annihilated by the local projector acting on those 3 spins. One can then proceed to embed these two low entanglement states in a thermal spectrum by constructing a Hamiltonian of the form

$$H = \sum_{j=1}^L P_j h_j P_j \quad (2.39)$$

where the h_j can be chosen arbitrarily. In [58], h_j was chosen to be

$$h_j = \sum_{\alpha=x,y,z} \left[J_\alpha \left(S_{j-1}^\alpha S_j^\alpha + S_j^\alpha S_{j+1}^\alpha \right) + J'_\alpha \left(S_{j-2}^\alpha S_j^\alpha + S_j^\alpha S_{j+2}^\alpha \right) - h_\alpha S_j^\alpha \right] \quad (2.40)$$

with $J_x = J_y = 1, J_z = -0.6, J'_x = -0.8, J'_y = J'_z = 0, h_x = 0.3, h_y = 0, h_z = 0.1$. To detect the scar eigenstates embedded in the spectrum, one can compute $(1/L) \sum_j \langle \phi_n | P_j | \phi_n \rangle$ for a given eigenstate $|\phi_n\rangle$ of H with energy E_n , see the left panel of Figure 1 in [58], which shows that the embedded states are outliers in a otherwise thermalizing spectrum. Since P_j is not a conserved operator of the system [58] and only acts non-trivially on 3 sites, the ETH should apply (the ETH should apply to any few body operators as discussed above) and expectation values with respect to the eigenstates $|\phi_n\rangle$ should agree with the micro-canonical expectation value computed within an energy window centered around E_n . A useful metric to detect deviations from this expected behavior is given by

$$r[O, E_0, \Delta E_0] \equiv \max_{E_n \in [E_0 - \Delta E_0, E_0 + \Delta E_0]} \left| \langle \phi_n | O | \phi_n \rangle - \langle O \rangle_{\text{mc}}^{E_n, \Delta E} \right| \quad (2.41)$$

$\langle O \rangle_{\text{mc}}^{E_n, \Delta E}$ is the microcanonical average of O as defined in equation 2.9, and the energy range used to compute it was chosen in [58] to be $\Delta E = \frac{1}{100} \sqrt{L}$ spanning the energy interval $[E_n - \Delta E, E_n]$. Provided the ETH is satisfied, r should tend towards 0 with system size. By computing r for various system sizes with $E_0 = 0$, $\Delta E_0 = \frac{1}{10} L$ (r for this choice of E_0 and ΔE_0 is denoted r_1) and choosing to include or not the embedded scar eigenstates in the calculation, one obtains Figure 1 of [58] which shows that r_1 goes to 0 when the embedded states are excluded, but remains finite when they are included which are signs that the ETH is not satisfied in this system.

Finally, note that it is even possible to embed an exponential number of scarred eigenstates using this method. This can be done by choosing P_j that have a 0 eigenspace of dimension d larger than 1 and such that $[P_j, P_k] = 0$ for all sites. In such a case, the dimension of \mathcal{T} is d^L which scales exponentially with system size. If all the states in \mathcal{T} show non-thermal behavior, the ETH is strongly violated. For a concrete example of this, see section 5.3 or [58].

2.6 Connection to unstable classical orbits

It was showed in [25] that a connection between the PXP scars and an underlying classical system can be established by making use of matrix product states and the the time-dependent variational principle (TDVP). In this section, the method used to establish this connection is reviewed.

Ref. [25] introduces a set of Hamiltonians given by

$$H = \Omega \sum_j \mathcal{P} S_j^x \mathcal{P} \quad (2.42)$$

composed of L individual spin- s particles on a ring. A basis for each site j is spanned by the states $|n_j\rangle$, $n = 0, 1, \dots, 2s$ which are assumed to be the $2s + 1$ eigenstates of the local spin- s operator in the z direction S_j^z such that $S_j^z |n_j\rangle = (-s + n) |n_j\rangle$. The projector $\mathcal{P} = \prod_j \mathcal{P}_{j,j+1}$ is a product of commuting local projectors $\mathcal{P}_{j,j+1} = I_j \otimes I_{j+1} - Q_j \otimes Q_{j+1}$, with $Q_j = I_j - P_j$

and $P_j = |n=0\rangle_j \langle n=0|_j \equiv |0\rangle_j \langle 0|_j$ which ensures that the dynamics is constrained to a subspace where at least one of two neighboring spins is in state $|0\rangle$. For the rest of this section, only the case of $s = 1/2$, $\Omega = 1$ is considered which corresponds to the PXP model.

The motivation for using MPS methods comes from the fact that the quantum many-body scarred eigenstates that compose the $|\mathbb{Z}_2\rangle$ states in the PXP model have low entanglement entropy. This suggests that an MPS representation of the state $e^{-iH_{\text{PXP}}t} |\mathbb{Z}_2\rangle$ should be highly efficient. Starting with a set of product states of the form $\otimes_j |\vartheta_j, \varphi_j\rangle \equiv \otimes_j \left[\cos(\vartheta_j/2) |0\rangle_j - ie^{i\varphi_j} \sin(\vartheta_j/2) |1\rangle_j \right]$, one can produce an ansatz state for the true time evolution by projecting this product state onto the blockade-free subspace (no configurations with two consecutive $|0\rangle$ state). One then obtains [25]

$$|\psi(\boldsymbol{\vartheta}, \boldsymbol{\varphi})\rangle = \mathcal{P} \bigotimes_j \left| (\vartheta_j, \varphi_j) \right\rangle \quad (2.43)$$

where \mathcal{P} is the projector onto the PXP blockade-free subspace, $\boldsymbol{\vartheta} = (\vartheta_1, \vartheta_2, \dots, \vartheta_L)$ and $\boldsymbol{\varphi} = (\varphi_1, \varphi_2, \dots, \varphi_L)$. Provided the non linear mapping $(\boldsymbol{\vartheta}, \boldsymbol{\varphi}) \rightarrow (\boldsymbol{\theta}, \boldsymbol{\phi})$, $|\psi(\boldsymbol{\vartheta}, \boldsymbol{\varphi})\rangle / \|\psi(\boldsymbol{\vartheta}, \boldsymbol{\varphi})\| = |\psi(\boldsymbol{\theta}, \boldsymbol{\phi})\rangle$, one can massage Equation 2.43 to obtain the following MPS state [25]

$$\begin{aligned} |\psi(\boldsymbol{\theta}, \boldsymbol{\phi})\rangle &= \text{Tr}(A_1 A_2 \cdots A_L) \\ A_j(\theta_j, \phi_j) &= \begin{pmatrix} P_j \left| (\theta_j, \phi_j) \right\rangle & Q_j \left| (\theta_j, \phi_j) \right\rangle \\ |0\rangle_j & 0 \end{pmatrix} \end{aligned} \quad (2.44)$$

where $P_j = |0\rangle_j \langle 0|_j$, $Q_j = I_j - P_j$, $\left| (\theta_j, \phi_j) \right\rangle = e^{i\phi_j \frac{1}{2}} e^{i\phi_j S_j^z} e^{-i\theta_j S_j^x} |0\rangle_j$, $\boldsymbol{\theta} = (\theta_1, \theta_2, \dots, \theta_L)$ and $\boldsymbol{\phi} = (\phi_1, \phi_2, \dots, \phi_L)$. Once the ansatz MPS state is established, the next step is to describe its time evolution inside of the variational manifold parametrized here by $\boldsymbol{\theta}, \boldsymbol{\phi}$ and if possible establish an error bound at different points on this Manifold (some metric that will determine how far we are from the true time evolution). This can be achieved by making use of the TDVP which aims at generating a trajectory contained within the variational manifold that minimizes the error with respect to the exact time evolution. To determine which trajectory is optimal, one needs to minimize at any time t and for any set of coordinates $z = (\boldsymbol{\theta}, \boldsymbol{\phi})$ the difference between the exact infinitesimal time evolution and the infinitesimal time evolution restricted to the manifold. The vector describing the actual infinitesimal time evolution at

a given point on the variational manifold is given by $\lim_{\delta t \rightarrow 0} (e^{-iH_{\text{PXP}}(\delta t)} - I) |\psi(z)\rangle / \delta t = -iH_{\text{PXP}} |\psi(z)\rangle$ while the vector characterizing the infinitesimal time evolution within the variational manifold is given by $\lim_{\delta t \rightarrow 0} (|\psi(z + \delta t)\rangle - |\psi(z)\rangle) / \delta t = \dot{z} \partial_z |\psi(z)\rangle$. Thus, the optimal choice for z is found whenever the difference between these two vectors is minimized, which can be expressed mathematically as

$$\min_{\dot{z}} \|\dot{z} \partial_z |\psi(z)\rangle + iH |\psi(z)\rangle\| \quad (2.45)$$

This is minimized provided $z(t)$ is such that the quantity $\dot{z} \partial_z |\psi(z)\rangle$ is the projection of the proper infinitesimal time evolution onto the variational manifold. Mathematically, one then obtains the following equation of motion

$$\sum_k \langle \partial_{z_l} \psi(z) | \partial_{z_k} \psi(z) \rangle \dot{z}_k + i \langle \partial_{z_l} \psi(z) | H |\psi(z)\rangle = 0 \quad (2.46)$$

The quantity $\langle \partial_{z_l} \psi(z) | \partial_{z_k} \psi(z) \rangle$ is called the Gram matrix where the indexes l, k run over the components of z . This also provides an instantaneous error given by

$$\Gamma(z) = \|\dot{z} \partial_z |\psi(z)\rangle + iH |\psi(z)\rangle\| \quad (2.47)$$

and can be used to quantify how well the variational manifold actually captures the exact time evolution of the system. Furthermore, the error of the time evolution is upper bounded by $\|e^{-iHt} |\psi(z(0))\rangle - |\psi(z(t))\rangle\| \leq \int_0^t \Gamma(z(t)) dt$. Solving this set of equations for the above MPS ansatz yields $\dot{\phi}_i = 0$ [25]. Furthermore, since the state of interest is translationally invariant when shifted by two sites, one can assume that $\theta_i = \theta_{i+2}$ throughout the time evolution. As a consequence, one is only left with two variational parameters θ_o and θ_e for odd and even sites respectively. Making use of the TDVP method presented above, one then obtains $\dot{\theta}_e = f(\theta_e(t), \theta_o(t))$ and $\dot{\theta}_o = f(\theta_o(t), \theta_e(t))$ with [25]

$$\begin{aligned} f(x, y) = \Omega \left[1 - \cos^{4s-2} \left(\frac{x}{2} \right) + \cos^{4s-2} \left(\frac{x}{2} \right) \cos^{2s} \left(\frac{y}{2} \right) \right. \\ \left. + 2s \sin \left(\frac{x}{2} \right) \cos^{6s-1} \left(\frac{x}{2} \right) \tan \left(\frac{y}{2} \right) \right], \end{aligned} \quad (2.48)$$

where $s = 1/2$. This equation is a complicated coupled non-linear differential equation that cannot be solved exactly, but the flow diagram shows the existence of a single unstable

periodic orbit that captures oscillations between the Néel states, as can be seen in Fig. 1 of [25]. This is reminiscent of the Bunimovich stadium in which the observed revivals arise from a connection to unstable orbits of a corresponding classical system. Indeed, we have arrived at a faithful description of the real time evolution in terms of a set of differential equations that can be interpreted as describing the motion of a classical particle in a two-dimensional variational manifold defined by θ_e, θ_0 . The time evolution of the Neel states is characterized by the motion of such a classical particle along an unstable orbit that oscillates between the two Neel states, see Fig. 1 of [25] for an illustration of this phenomenon.

2.7 Towers of scar states

Another striking example of quantum scars comes from systems that exhibit multiple degenerate scarred eigenstates called scar towers. An exact tower of scarred states is a set of degenerate non-thermal eigenstates embedded in an otherwise thermalizing spectrum (i.e a set of degenerate eigenstates that violate the ETH even if they are contained in a symmetry sector that hosts other eigenstates with similar energy that are thermal). Section 5.3 presents an example of a system (found using the methods developed in this work) dubbed QMBS-C that hosts scar towers. An efficient way to show the presence of scar towers and to obtain them explicitly was presented in [37]. The main ideas behind this method and an example of a system where this formalism applies is presented in this section.

First assume the existence of a Hamiltonian H , a linear subspace W of the Hilbert space, an eigenstate of H , $|\Phi_0\rangle \in W$ with energy E_0 , an operator Q^\dagger such that $Q^\dagger W \subset W$ and [37]

$$([H, Q^\dagger] - \omega Q^\dagger)W = 0. \quad (2.49)$$

where ω is some constant. Provided the above requirements are fulfilled, one has that as long as $(Q^\dagger)^n |\Psi_0\rangle$ is a non-zero vector, then the resulting state is an eigenstate of H with eigenvalue $E_0 + n\omega$. As an example of a system for which this formalism applies, consider the 1D spin 1 AKLT model which has the following Hamiltonian

$$\hat{H} = \sum_{j=1}^L \left(\frac{1}{3} + \frac{1}{2} \vec{S}_j \cdot \vec{S}_{j+1} + \frac{1}{6} (\vec{S}_j \cdot \vec{S}_{j+1})^2 \right) \quad (2.50)$$

This model can be rewritten in terms of projectors onto total spin 2 subspace of pairs of neighboring sites, i.e

$$H = \sum_{j=1}^L P_j = \sum_{j=1}^L \left(\sum_{m=-2}^2 |T_{2,m}\rangle \langle T_{2,m}| \right)_{j,j+1} \quad (2.51)$$

where P_j acts non-trivially on sites $j, j+1$. Define $\vec{S}_j = (S_j^x, S_j^y, S_j^z)$, then the $|T_{l,m}\rangle$ states are the common eigenstates of $(\vec{S}_j + \vec{S}_{j+1})^2$ and $S_j^z + S_{j+1}^z$ with eigenvalues $l(l+1)$ and m respectively. This relation between the projector and the spin representation of the Hamiltonian can be derived as follows. Define the total spin operator of two neighboring sites as $\vec{S}_j^{\text{tot}} = \vec{S}_j + \vec{S}_{j+1}$. The operator $(\vec{S}_j^{\text{tot}})^2$ has three eigenvalues, 0, 2 and 6. One can then construct an operator in terms of $(\vec{S}_j^{\text{tot}})^2$ that has an eigenvalue of 0 for arbitrary combinations of spin 1 and 0 states, but an eigenvalue of 1 for an arbitrary superposition of spin 2 states. Such an operator is given by $P_j = \frac{1}{24}(\vec{S}_j^{\text{tot}})^2((\vec{S}_j^{\text{tot}})^2 - 2)$. Expanding this expression yields equation 2.50. The ground state of such an Hamiltonian $|G\rangle$ is given by the unique state that does not have any spin 2 component on any bond $(j, j+1)$ which directly implies that the state has energy 0 because of the projector nature of the Hamiltonian. Scarred eigenstates can then be generated by the repeated action of the operator Q^\dagger (see equation 2.52) on the ground state, where the linear subspace W is defined in this case to be the space composed of the states $|G\rangle, Q^\dagger |G\rangle, \dots, (Q^\dagger)^n |G\rangle, \dots$

$$\begin{aligned} |\mathcal{S}_{2n}\rangle &= (Q^\dagger)^n |G\rangle, \\ Q^\dagger &= \sum_{j=1}^L (-1)^j (S_j^+)^2 \end{aligned} \quad (2.52)$$

To prove that the states $|\mathcal{S}_{2n}\rangle$ are indeed eigenstates of H , it is sufficient to show that $[H, Q^\dagger] |\mathcal{S}_{2n}\rangle = 2Q^\dagger |\mathcal{S}_{2n}\rangle$. The proof presented here follows closely the proof given in [37].

First, one has that

$$\begin{aligned} [H, Q^\dagger] &= \left[\sum_{j=1}^L P_j, \sum_{l=1}^L (-1)^l (S_l^+)^2 \right] = \sum_{j=1, l \in (j, j+1)}^L [P_j, (-1)^l (S_l^+)^2] \\ &= \sum_{j=1}^L (-1)^j [P_j, (S_j^+)^2 - (S_{j+1}^+)^2] \end{aligned} \quad (2.53)$$

Now, one can obtain the transitions induced by $(S_j^+)^2 - (S_{j+1}^+)^2$ by computing the matrix elements in the total spin basis of consecutive spins. The common eigenstates of $(S_i^{\text{tot}})^2$ and

$S_i^z + S_{i+1}^z$ are given explicitly by

$$\begin{aligned}
|T_{2,-2}\rangle &= |-1, -1\rangle, & |T_{2,-1}\rangle &= \frac{1}{\sqrt{2}}(|0, -1\rangle + |-1, 0\rangle), \\
|T_{2,0}\rangle &= \frac{1}{\sqrt{6}}(|1, -1\rangle + 2|0, 0\rangle + |-1, 1\rangle), \\
|T_{2,1}\rangle &= \frac{1}{\sqrt{2}}(|1, 0\rangle + |0, 1\rangle), & |T_{2,2}\rangle &= |1, 1\rangle, \\
|T_{1,-1}\rangle &= \frac{1}{\sqrt{2}}(|0, -1\rangle - |-1, 0\rangle), \\
|T_{1,0}\rangle &= \frac{1}{\sqrt{2}}(|1, -1\rangle - |-1, 1\rangle), \\
|T_{1,1}\rangle &= \frac{1}{\sqrt{2}}(|1, 0\rangle - |0, 1\rangle), \\
|T_{0,0}\rangle &= \frac{1}{\sqrt{3}}(|1, -1\rangle - |0, 0\rangle + |-1, 1\rangle).
\end{aligned} \tag{2.54}$$

One can then compute the matrix elements of $(S_j^+)^2 - (S_{j+1}^+)^2$ in this basis, e.g $((S_j^+)^2 - (S_{j+1}^+)^2) |T_{0,0}\rangle = \frac{1}{\sqrt{3}}(|1, 1\rangle - |-1, 1\rangle) = 0$. The computation of all matrix elements then yields

$$\begin{aligned}
(S_j^+)^2 - (S_{j+1}^+)^2 &= 2(-|T_{2,1}\rangle \langle T_{1,-1}| \\
&\quad - \sqrt{2}|T_{2,2}\rangle \langle T_{1,0}| + |T_{1,1}\rangle \langle T_{2,-1}| + \sqrt{2}|T_{1,0}\rangle \langle T_{2,-2}|)_{j,j+1}
\end{aligned} \tag{2.55}$$

With such a representation, the action of the projector on Q^\dagger is easily computed and one obtains that

$$\begin{aligned}
\left[P_{j,j+1}^{(2,1)}, (S_j^+)^2 - (S_{j+1}^+)^2 \right] &= -2(|T_{2,1}\rangle \langle T_{1,-1}| \\
&\quad + \sqrt{2}|T_{2,2}\rangle \langle T_{1,0}| + |T_{1,1}\rangle \langle T_{2,-1}| + \sqrt{2}|T_{1,0}\rangle \langle T_{2,-2}|)_{j,j+1}
\end{aligned} \tag{2.56}$$

One can conveniently subtract and add back the total spin representation of $(S_j^+)^2 - (S_{j+1}^+)^2$ to this expression which yields

$$\begin{aligned}
\left[P_{j,j+1}^{(2,1)}, (S_j^+)^2 - (S_{j+1}^+)^2 \right] &= (S_j^+)^2 - (S_{j+1}^+)^2 \\
&\quad - 4(|T_{1,1}\rangle \langle T_{2,-1}| + \sqrt{2}|T_{1,0}\rangle \langle T_{2,-2}|)_{j,j+1}
\end{aligned} \tag{2.57}$$

From the above expression, one can identify $-4(|T_{1,1}\rangle \langle T_{2,-1}| + \sqrt{2}|T_{1,0}\rangle \langle T_{2,-2}|)_{j,j+1}$ with A_j . Thus, one has that

$$\left[H, Q^\dagger \right] = 2Q^\dagger + \sum_j (-1)^j A_j, \tag{2.58}$$

which will yield the desired result provided $\sum_j (-1)^j A_j |S_{2n}\rangle = 0$ for all n . This is clearly true for $|G\rangle$ and by looking at the terms that appear in $(S_j^+)^2 - (S_{j+1}^+)^2$, one can see that if the initial state $|\Phi_0\rangle$ is a state composed exclusively of total spin 1 and total spin 0 states on any bond i.e the ground state, then repeated application of Q^\dagger produces a state that locally has

weight on $|T_{2,1}\rangle$, $|T_{2,2}\rangle$ and $|T_{1,m}\rangle$ states. This implies that $A_j |S_{2n}\rangle = 0$ since the A_j only give a non-vanishing result when they act on the states $|T_{2,-1}\rangle$, $|T_{2,-2}\rangle$. For each eigenstate $|S_{2n}\rangle$, one can generate $4n$ additional spin rotated eigenstates due to the $SU(2)$ symmetry of the AKLT model. This shows that the repeated action of the operator Q^\dagger onto the ground state creates towers of excited eigenstates. Furthermore, it has been demonstrated [41] that these eigenstates explicitly violate the ETH. For instance, their half-chain entanglement entropy grows slower than a volume law.

Chapter 3

Quantum cellular automata

This section thus provides a brief introduction to quantum cellular automata. Quantum cellular automata form the backbone of the method presented in section 5, which aims at converting quantum cellular automata with non-thermal properties to Hamiltonian system. This is done with the hope of transferring some of the non-thermal properties to the Hamiltonian setting, which is showed to be possible provided some conditions are met.

3.1 Classical cellular automata

Before describing what a quantum cellular automaton is, it is appropriate to first discuss classical cellular automata. The first instance of a classical cellular automaton is due to Von Neumann [65], who spent some time designing systems that discretely update in time a set of discrete variables according to the state of the neighboring variables. In this class of systems, he was able to find examples that are computationally universal, meaning that the model can in principle be used to run any classical program, which was his main motivation for considering such models in the first place. A striking example of a model with this property is Conway's Game of Life [15] which, remarkably, because it is computationally universal, can simulate anything that a conventional computer can simulate, including Conway's Game of Life.

More formally, classical cellular automata describe the discrete time evolution of discrete

variables arranged on a d -dimensional lattice. The lattice sites are denoted by \vec{r}_n . Each local variable is updated to the result of $f(\mathcal{N}(\vec{r}_n))$ which takes as input the lattice sites in a neighborhood of \vec{r}_n denoted by $\mathcal{N}(\vec{r}_n)$.

As an example of a class of classical cellular automata, let us consider all classical one-dimensional automata with binary local variables that are updated according to the state of their nearest neighbors. All these automata have been classified by Wolfram in his book [67]. The plethora of possible local update rules produces many distinct kinds of dynamical behavior. Some of these classical automata have a very predictable behavior whilst others seem to exhibit nearly chaotic yet structured dynamical properties. For instance, consider the automaton given by rule 110 CA. It's corresponding update table is given below

State of three adjacent bits	111	110	101	100	011	010	001	000
Updated middle bits	0	1	1	0	1	1	1	0

See Fig. 3.1 for a visual representation of the time evolution produced by the automaton 110 CA. Classical cellular automata can accurately simulate a wide variety of interesting phenomena including fluid flows [60], biological pattern formation [17] and percolation problems [54] to name only a few. However, as a consequence of their purely classical nature, classical cellular automata are constrained to describe classical phenomena. Quantum cellular automata can be viewed as a natural extension of classical cellular automata to the quantum setting, now allowing for entanglement and complex behaviors only possible in the quantum setting.

3.2 Quantum cellular automata

Intuitively, the definition of quantum cellular automata should encapsulate most of the important properties of quantum systems while exhibiting some features reminiscent of classical cellular automata. For example, the update rule should be unitary, preserve locality and be able to generate entanglement between different regions of the system. By trying to satisfy all these properties simultaneously, one could then conclude that a quantum cellular automaton must satisfy the following criteria.

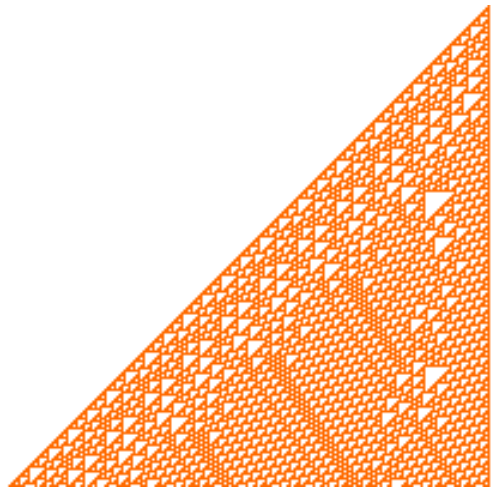


Figure 3.1: Illustration of the time evolution of a classical cellular automaton. Time goes from top to bottom. Each colored cell represents a cell in state one, the cell is assumed to be in state 0 otherwise (colored white). The figure is obtained by initializing a single cell to the state 1 in the middle of the chain, and then time evolving this initial state according to rule 110 which produces a complex, yet structured, time evolution.

A quantum cellular automaton T must be defined on a discrete lattice Γ of quantum systems which may be finite or infinite, possibly with periodic boundary conditions. Each individual quantum system on a given site \vec{r}_n of the lattice is either a qudit or it is taken to be a finite number of fermion modes. It is worth noting that more exotic local quantum systems are possible, but for the purpose of this work, they won't be required.

For finite lattice systems, the Hilbert space is constructed from the tensor product of all the local Hilbert spaces $\mathcal{H}_{\vec{r}_n}$ associated with the n^{th} lattice site \vec{r}_n . Instead of working with the explicit Hilbert space, it is often convenient to work instead with the algebra of observables. Denote by $\mathcal{A}_{\vec{r}_n}$ the algebra of observables at site \vec{r}_n , then the full algebra of observables is given by the tensor product of all the local algebras $\bigotimes_{\vec{r}_n} \mathcal{A}_{\vec{r}_n}$.

For infinite lattices, one quickly runs into problems since quantities such as $(\langle 0|)^{\otimes N} (-|0\rangle)^{\otimes N}$ are not well defined as one takes the limit $N \rightarrow \infty$ (since the sign oscillates). A natural way of fixing such problems is to restrict the set of observables to quasi-local operators by only allowing for operators that can be constructed from a Cauchy sequence of local terms. This approach is called the quasi-local algebra approach. The entire set of quasi-local operators is denoted here by \mathcal{A} . For further details about the theory of quasi-local algebras, see [8], but in this work only finite system sizes are considered so the details of the theory won't be required.

Now, based on the intuition of what a quantum cellular automaton should be, one can see that a natural definition for a quantum cellular automaton T should describe an operation that time evolves discretely the quasi-local algebra of observables while preserving locality in a strict sense (just like for classical cellular automata). Furthermore, the operation T should preserve the commutation relations, just like unitary time evolution would. This leads to the following definition

Definition: (paraphrasing from [18]) A quantum cellular automaton consists of a discrete hypercubic lattice, which may be finite or be \mathbb{Z}^d , with a finite dimensional quantum

system at each site (qudits and/or fermion modes). Evolution takes place over discrete time steps via a locality-preserving automorphism (or unitary matrix for finite systems of finite size).

An automorphism has the property that $T(AB) = T(A)T(B) \forall A, B \in \mathcal{A}$ which implies that it preserves commutation relations in the sense that $[T(A), T(B)] = T([A, B])$. An automorphism can be viewed as nothing more than the natural generalization of conjugation by a unitary matrix to systems of infinite size. Locality is the statement that if an operator $A \in \mathcal{A}$ has support on site \vec{r}_n , then $T(A)$ has support on a neighborhood $\mathcal{N}(\vec{r}_n)$ centered around \vec{r}_n where all sites $\vec{r}'_i \in \mathcal{N}(\vec{r}_n)$ are such that $\|\vec{r}'_i - \vec{r}_n\| \leq l$ for some range $0 \leq l$, see Fig. 3.2

3.2.1 Concrete example of a quantum cellular automaton

Let's now illustrate the above ideas by studying the properties of a given quantum cellular automaton. Consider a quantum cellular automaton that acts on a one-dimensional spin-1/2 chain where the lattice sites \vec{r}_j are labeled by the index j . The individual quantum system at site j is a spin-1/2 and the local algebra is generated by the Pauli matrices acting on that site. Consider a local rule T_j with the following properties

$$\begin{aligned} T_j[X_j] &= Z_j \\ T_j[Z_j] &= Z_{j-1} \otimes X_j \otimes Z_{j+1} \end{aligned} \tag{3.1}$$

for all j . Let's further require T_j to be an homomorphism which directly specifies the image of Y_j . Indeed, in this case one has that

$$T_j(Y_j) = T_j(iX_jZ_j) = iT_j(X_j)T_j(Z_j) = -Z_{j-1} \otimes Y_j \otimes Z_{j+1} \tag{3.2}$$

Now define the quantum cellular automaton T to be the combined action of the local rules on each individual quantum system j . It can be shown that the global rule T constitutes an automorphism by verifying that all commutation rules are preserved. Namely, one has that

$$\begin{aligned} [T(X_j), T(X_k)] &= [Z_j, Z_k] = 0, \\ [T(Z_j), T(Z_k)] &= [Z_{j-1} \otimes X_j \otimes Z_{j+1}, Z_{k-1} \otimes X_k \otimes Z_{k+1}] = 0, \end{aligned} \tag{3.3}$$

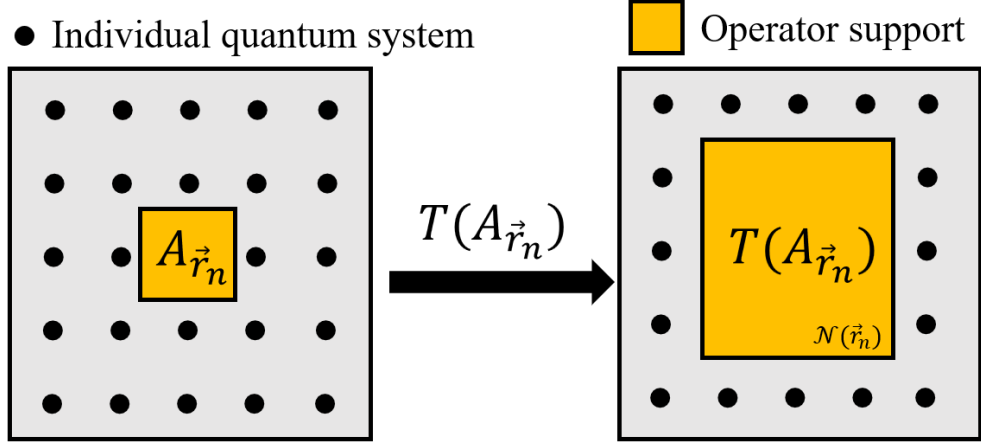


Figure 3.2: Illustration of the action of a quantum cellular automaton T on a local operator $A_{\vec{r}_n}$ with initial support on the quantum system situated at \vec{r}_n . The resulting operator has support only on a neighborhood $\mathcal{N}(\vec{r}_n)$ of \vec{r}_n .

and

$$\begin{aligned} [\mathbb{T}(Z_j), \mathbb{T}(X_k)] &= [Z_{j-1} \otimes X_k \otimes Z_{j+1}, Z_k] = 0, j \neq k \\ \{ \mathbb{T}(Z_j), \mathbb{T}(X_j) \} &= \{ Z^{j-1} \otimes X_j \otimes Z_{j+1}, Z_j \} = 0 \end{aligned} \quad (3.4)$$

Using the above rules, one can compute what the action of T will be when it acts on a product of operators. Consider for instance the operator $\dots I_{-2} \otimes Z_{-1} \otimes Y_0 \otimes X_1 \otimes I_2 \dots$ where ellipsis denote an infinite tensor product of identity matrices. Applying T on such an operator yields

$$\dots T(I_{-2}) \otimes T(Z_{-1}) \otimes T(Y_0) \otimes T(X_1) \otimes T(I_2) \dots \quad (3.5)$$

Expanding and computing the product explicitly, one obtains

$$\dots I_{-3} \otimes Z_{-2} \otimes Y_{-1} \otimes X_0 \otimes I_1 \dots \quad (3.6)$$

Note that the initial operator was merely translated by one site to the left. This quantum cellular automaton thus translated that particular configuration to the left hence giving it its name, the glider.

3.2.2 Floquet driving and quantum cellular automata

As a final note on quantum cellular automata, it is worth discussing a class of physical systems that are accurately described by a quantum cellular automaton. This relation is used

extensively in section 5.

Consider a time dependant Hamiltonian $H(t)$ such that $H(t + \tau) = H(t)$ for some period τ . Writing down the Schrödinger equation for the time evolution operator $U(t, 0)$, $0 \leq t$ for which $|\psi(t)\rangle = U(t, 0)|\psi(0)\rangle$ leads to the differential equation

$$\frac{d}{dt}U(t, 0) = -iH(t)U(t, 0) \quad (3.7)$$

with boundary condition $U(0, 0) = I$. A formal solution to this equation is given by

$$U = \mathcal{T} \exp\left(-i \int_0^\tau dt H(t)\right) \quad (3.8)$$

where \mathcal{T} is the time ordering operator. Consider now a one-dimensional static Hamiltonian

$$H = \sum_j h_j \quad (3.9)$$

where the h_j have local support on sites $j, j + 1$. Further assume a system size of $L = 2n$ for some positive integer n with periodic boundary conditions. Now define the operators A and B to be

$$A = \sum_j^{L/2} h_{2j} \quad B = \sum_j^{L/2} h_{2j+1} \quad (3.10)$$

From A and B , one can then construct the time-dependant Hamiltonian

$$H(t) = \sigma(t, \tau)A + (1 - \sigma(t, \tau))B \quad (3.11)$$

where

$$\sigma(t, \tau) = \begin{cases} 0 & \text{if } t \in [n\tau, (n + 1/2)\tau] \text{ for some } n \in \mathbb{Z} \\ 1 & \text{Otherwise} \end{cases} \quad (3.12)$$

which can be thought of as driving the system with B for a time $\tau/2$, then with A for a time $\tau/2$, and repeating this process indefinitely. For this $H(t)$, an exact solution of 3.8 for $t = \tau$ is given by $e^{-i\frac{A\tau}{2}}e^{-i\frac{B\tau}{2}}$. Further note that the Hamiltonian terms h_{2j} that appear in A commute with each other due to their non-overlapping support, and similarly for B . This implies that $e^{-i\frac{A\tau}{2}}$ and $e^{-i\frac{B\tau}{2}}$ can be written as a product of local unitary matrices

$U_j = e^{-i\frac{h_j\tau}{2}}$ where U_j has support on sites $j, j+1$. This leads to the representation

$$U(\tau, 0) = e^{-i\frac{A\tau}{2}} e^{-i\frac{B\tau}{2}} = \left(\prod_j^{L/2} U_{2j} \right) \left(\prod_j^{L/2} U_{2j+1} \right) \quad (3.13)$$

Furthermore, due to the fact that $H(t + \tau) = H(t)$, one has that

$$U(n\tau, 0) = U(\tau, 0)^n \quad (3.14)$$

for arbitrary positive integers n . This implies that the time evolution resulting from $H(t)$ at times $n\tau$ is fully described by the quantum cellular automaton $T = U(\tau, 0)$. Thus, one can associate a quantum cellular automaton of the form 3.13 with a driven quantum system. Assuming that the automaton $T(\tau) = e^{-i\frac{A\tau}{2}} e^{-i\frac{B\tau}{2}}$ for some chosen period τ is simple enough so that it exhibits non-thermal behavior (e.g the automaton might be chosen to permute computational basis states, in which case the computational basis state never gain entanglement), it might then be worth asking how close this automaton is from the unitary operator $e^{-i\frac{(A+B)\tau}{2}}$ describing the time evolution under the Hamiltonian $A+B$. Provided the two operators are close (with respect to some measure, for instance the operator norm of the difference $e^{-iA\tau/2}e^{-iB\tau/2} - e^{-i(A+B)\tau/2}$), one might then be able to explain the presence of scarred eigenstates in $H = A+B$ by making use of the underlying automaton. A detailed exploration of this idea is presented in section 5.

Chapter 4

Prethermalization

If a given system possesses well separated time scales, then an intermediate stage of thermalization called prethermalization can emerge where the system first relaxes to a prethermal state before eventually reaching true equilibrium. A typical setting for the observation of such a phenomenon is whenever the Hamiltonian is of the form $H = H_0 + \lambda V$ where λ is a dimensionless small parameter which controls the time-scale separation. There are then two relevant time scales at play, one associated with H_0 which is denoted by τ_0 , and one associated with V denoted by τ_V . If the system is time evolved for a time much smaller than τ_V but much larger than τ_0 , then the system reaches a prethermal state associated with thermal eigenstates of H_0 , which will last until t reaches a value comparable to τ_V . The state of the system can be described during the time evolution by its density matrix $\rho(t)$. One can then define $\rho(t) = \rho_{pre}$ when $\tau_0 \ll t \ll \tau_V$ which refers to the prethermal quasi-equilibrium state. True thermalization is only assumed whenever $\rho(t)$ is locally equivalent to ρ_{mc} (i.e partial traces over small sub-regions of the system should be close to each other, and the difference should decay exponentially with system size), the micro-canonical density matrix associated with the full Hamiltonian. It is worth noting that the system might achieve true thermalization when $\tau_0 \ll t \ll \tau_V$, i.e it is possible that $\rho_{pre} = \rho_{mc}$. For example, this will be the case if H_0 satisfies the ETH. Thus, in order to observe prethermalization, the Hamiltonian H_0 is required to break explicitly the ETH. This will be the case if the Hamiltonian H_0 has a large number of conserved quantities preventing full thermalization.

4.1 Generalized Gibbs ensemble

To describe the prethermal state associated with a Hamiltonian H_0 that conserves a large set of operators \mathcal{I}_n which prevent “conventional” thermalization (the different symmetry sectors cannot mix together which leads to anomalies), one can make use of the Generalized Gibbs ensemble which aims at describing the thermal state when taking into account the conservation laws. For instance, the equilibrium density matrix ρ_{GGE} associated with the generalized Gibbs ensemble will be such that the stationary n point correlation functions of a set of local operators $O_a(x)$ are given by [34]

$$\lim_{t \rightarrow \infty} \langle \Psi(t) | \prod_{a=1}^n O_a(x_a) | \Psi(t) \rangle = \text{Tr} \left[\rho_{\text{GGE}} \prod_{a=1}^n O_a(x_a) \right] \quad (4.1)$$

$$|\Psi(t)\rangle = \exp(-iHt) |\Psi(0)\rangle \quad \rho_{\text{GGE}} = \frac{1}{Z} \exp \left(- \sum_m \lambda_m \mathcal{I}_m \right), \quad (4.2)$$

where \mathcal{I}_m denotes a set of conserved operators indexed by the integer m and

$$Z = \text{Tr} \exp \left(- \sum_m \lambda_m \mathcal{I}_m \right) \quad (4.3)$$

is the partition function. A Lagrange multiplier λ_m is associated with each conserved operator \mathcal{I}_m and is obtained upon maximization of the Von-Neumann entropy

$$S = \text{Tr}(\rho_{\text{GGE}} \ln \rho_{\text{GGE}}) \quad (4.4)$$

under the restriction that the expectation value of the conserved operators obtained from ρ_{GGE} agrees with the expectation value of the initial state in the thermodynamic limit, i.e it must be the case that

$$\text{Tr} [\mathcal{I}_m \rho_{\text{GGE}}] = \langle \mathcal{I}_m \rangle (t = 0) \quad (4.5)$$

Importantly, for the generalized Gibbs ensemble conjecture to hold, it is essential to restrict the observables $O_a(x)$ to finite subsystems, it will in general not apply otherwise.

4.1.1 Quantum Newton’s cradle

The first experiment that visualized the effect of integrability on the relaxation dynamics of a quantum system was performed by Kinoshita et al. [31]. The experiment probed the

relaxation dynamics of Rubidium atoms trapped in an optical lattice. The optical lattice was devised to provide strong confinement in two transverse directions, thus producing an array of one-dimensional “tubes”, each filled with N_{tube} Rubidium atoms. The 1D limit was achieved by making sure that the lowest transverse mode excitation energy $\sim \omega_r/2\pi = 67\text{kHz}$ far exceeds all other relevant energy scales in the system. Furthermore, the tubes are separated well enough so that tunneling effects between the tubes are negligible.

The Rubidium atoms are confined along the 1D tubes using an anharmonic potential $U(z)$ where z denotes the distance from the lowest point of the potential $U(z)$, see Fig. 1 of [31]. The system is then quenched into a state with a momentum distribution peaked around $-2k$ and $+2k$, where k is the wave-vector of the 1D lattice. The quenched state can be understood as a state in which half the Rubidium atoms have momentum $+2k$ and the other half have momentum $-2k$, see Fig. 3 of [21]. To understand why such a system might not thermalize, it is worth considering a classical counterpart of the quantum system; Newton’s cradle, see Fig. 1 of [21]. In Newton’s cradle, the masses collide elastically in 1D and only exchange momentum values without ever altering the momentum distribution of the system. In this sense, the system never actually thermalizes. This provides some intuition as to why one might expect a lack of thermalization in the quantum setting. Provided the energy per particle at zero temperature is much smaller than the kinetic energy of the collisions in the quantum setting, then the collisions between the atoms are accurately described by infinitely strong interactions (Tonks–Girardeau limit). In this limit, it is known that the momentum distribution of the 1D gas expanding converges towards that of a trapped 1D Fermi’s gas [21]. In this limit, the system is, in principle, integrable, and the system relaxes according to an appropriate generalized Gibbs ensemble. In the actual experiment, the system is not strictly in the Tonks–Girardeau limit, and in this sense the model is described by an integrable model plus some small perturbation. The momentum distribution $f(p_x)$ is thus expected to converge towards a Gaussian distribution after some given transient time, which corresponds to the prethermal window discussed above. The experiment results reveal that the system does not quickly converge to a thermal state and instead remains in a prethermal state for a large amount of time. This is seen explicitly by probing the one-dimension momentum

distribution $f(p_x)$ which remains non-Gaussian for a large amount of time, see Fig. 3 of [21].

This 1D gas of bosonic atoms is a striking example of prethermalization, where it is observed that the dynamical properties of the system are mainly described by an integrable system for a large prethermal window despite the fact that the model is, strictly speaking, non-integrable.

4.2 Floquet prethermalization

This section discusses the phenomenon of Floquet prethermalization which, as will be shown in section 5.5, is identified as a possible mechanism for the emergence of quantum scars in the PXP model.

One begins by considering a periodic Hamiltonian with a period τ such that $H(t) = H(t+\tau)$. Such systems are expected to obey what is called the Floquet ETH which is the statement that the system should eventually thermalize, although several exceptions are known to exist [53, 35, 36]. Despite this eventual relaxation to equilibrium for most driven quantum systems, one might still try to determine how fast this equilibrium is reached. If the relaxation time is small compared to some relevant time-scale for the experiment, there is then the possibility of Floquet prethermalization where the system first reaches a prethermal quasi-stationary state before relaxing to the true thermal state.

The full time evolution during a single period τ can be captured by a single unitary matrix $U(t, 0)$ as previously defined in equation 3.8. The unitary matrix $U(0, t)$ can be written as the matrix exponential of an Hamiltonian matrix H_F called the Floquet Hamiltonian, i.e $U(t, 0) = e^{-iH_F t}$ which satisfies at time τ

$$e^{-iH_F \tau} \equiv \mathcal{T} e^{-i \int_0^\tau dt H(t)} \quad (4.6)$$

where $H(t)$ is the Hamiltonian of the system at time t and \mathcal{T} is the time ordering operator. The Floquet Magnus expansion is then a formal expression for H_F given by [39]

$$H_F = \sum_{m=0}^{\infty} \Omega_m \tau^m \quad (4.7)$$

with

$$\Omega_m = \sum_{\sigma} \frac{(-1)^{n-\theta[\sigma]} \theta[\sigma]! (n-\theta[\sigma])!}{i^n (n+1)^2 n! \tau^{n+1}} \int_0^{\tau} dt_{n+1} \dots \int_0^{t_2} dt_1 \left[H(t_{\sigma(n+1)}), \left[H(t_{\sigma(n)}), \dots, \left[H(t_{\sigma(2)}), H(t_{\sigma(1)}) \right] \dots \right] \right] \quad (4.8)$$

where $\theta(\sigma)$ is the sign of the permutation σ . Unfortunately, this series in general formally diverges which a priori prevents one from making any meaningful claim about the system based on the first couple terms of the expansion.

Fortunately, it was shown in [39] that the first couple of terms of the BCH expansion might still accurately describe the properties of the systems for a large prethermal time window, even in the presence of strong global driving of the system. One can define the n^{th} order truncated Floquet-Magnus expansion by an Hamiltonian operator $H_F^{(n)}$. It was showed in [33, 38] that one can, under specific circumstances, find an integer n such that

$$e^{-iH_F^{(n)}T} \simeq e^{-iH_F T}, \text{ where } H_F^{(n)} = \sum_{m=0}^n T^m \Omega_m \quad (4.9)$$

which will be approximately valid for transient time scales, see Fig. 1 in [33]. By making use of different bounding techniques [39], one can arrive at the important following theorem making the above claim more rigorous.

Theorem The n_0^{th} order truncated Floquet Hamiltonian $H_F^{(n_0)}$ is almost conserved up to an exponentially long time in the sense that [39]

$$\left\| H_F^{(n_0)}(t) - H_F^{(n_0)} \right\| \leq 16g^2 k 2^{-n_0} N_V t \quad (4.10)$$

where $t = mT$ with a positive integer m , $n_0 = 1/(8gk\tau) - 1$, $\|\dots\|$ is the operator norm, $H_F^{(n_0)}(t) = U^\dagger(t, 0) H_F^{(n_0)} U(t, 0)$ and g is defined such that

$$\text{for any site } i, \quad \sum_{\mathcal{X}: \mathcal{X} \ni i} \|h_{\mathcal{X}}(t)\| \leq g \quad (4.11)$$

where $\mathcal{X} = \{i_1, i_2, \dots, i_{|\mathcal{X}|}\}$ is a set of lattice sites onto which the local Hamiltonian $h_{\mathcal{X}}$ acts non-trivially, where the size of the set is denoted by $|\mathcal{X}|$. k is the largest such $|\mathcal{X}|$.

This important result implies that the truncated Floquet Hamiltonian $H_F^{(n_0)}$ can approximate the dynamics of the full Floquet Hamiltonian for an exponentially large prethermal time window. In section 5, numerical evidence (decrease of the amplitude of BCH terms before observing an increase) in the PXP model suggests that prethermalization might play an important role in the emergence of quantum scars for PXP in particular.

Chapter 5

QMBS from quantum cellular automata

This section first introduces a class of quantum cellular automata that exhibit highly non-thermal behavior despite being strongly interacting many-body systems. It is then shown that some Hamiltonian systems constructed from the automata can host quantum scars provided certain conditions are met. By making use of this relation between quantum cellular automata and scarred Hamiltonians, mechanisms responsible for the emergence of quantum scars in quantum many-body systems are identified. Furthermore, this connection between Hamiltonian systems and quantum cellular automata provides a recipe for engineering new QMBS systems. The results presented in this section are based on Ref. [52], reprinted with permission from Pierre-Gabriel Rozon, Michael J. Gullans, and Kartiek Agarwal. Constructing quantum many-body scar hamiltonians from floquet automata, Volume number 106, Page number 184304, Nov 2022. Copyright (2022) by the American Physical Society.

Automatons have a long and rich history of study, arising from their intriguing dynamical properties in both the classical [67] and quantum settings [22, 32, 66, 27], and are often associated with systems with state space [19, 24, 12] or kinetic constraints [20, 48, 28, 51]. The Floquet automata considered in this work are unitary circuits that effect permutations of computational basis states on a chain of qubits (although more general automata can be adopted). For the automata considered, the Hilbert space is naturally fragmented into

disjoint subspaces of computational basis states which are cycled through with successive applications of the automaton circuit. Thus, all computational basis states revive at fixed (but different) time intervals. It is natural to ask if these automata, which can be described as simple unitary circuits in the quantum setting, can be used to construct QMBS Hamiltonians which show similar revivals. We find that the answer is yes, and the principles uncovered can be used, for instance, to derive the PXP model, reveal timescales that govern the relaxation, and obtain new QMBS models that show revivals for arbitrarily chosen computational basis states.

For concreteness, we focus on automata with a two-layer brickwork circuit, illustrated in Fig. 5.1(a), which is composed of the elementary gate U_0 and whose Floquet unitary is given by $U_F = e^{-iA}e^{-iB}$, where A, B are local Hamiltonians related by translation. Here, A can be thought to be a sum of local, spatially disjoint Hamiltonians $A_j \equiv i \log U_{0,j}$ (to be made more precise later). A naive application of the Baker-Campbell-Hausdorff (BCH) formula to obtain a Hamiltonian from U_F is bound to fail as higher order BCH terms blow up in amplitude quickly while growing more non-local. Instead, we ask when the local Hamiltonian, $H_{\text{eff}} = A + B$, can reproduce dynamics generated by U_F on a *subspace* of chosen ‘orbit’ states, by virtue of forcing higher-order BCH terms to remain small (or ideally vanish) in this subspace. In particular, defining $C_n(A, B)$ as the n^{th} order term in the expansion, we formulate rules that strongly suppress $\|C_n(A, B)P_o\|$, where P_o is the projector onto the orbit subspace. Note that this bounds both $\|P_o C_n P_o\|$, which governs the corrections to the dynamics within the subspace of chosen orbit states, and $\|(\mathbb{1} - P_o)C_n P_o\|$, which governs the leakage from the orbit states into ‘generic’ states. In fact, forcing all $C_n P_o$ terms to vanish identically ensures that the Hamiltonian $H_{\text{eff}} = A + B$ admits certain eigenstates that are eigenstates of both A and B separately¹:—it is these select eigenstates, which if small in number, and possessing low entanglement, become the scarred eigenstates of the Hamiltonian H_{eff} . The latter is naturally the case if A is composed of a set of spatially disjoint local Hamiltonians, for instance, as we assume. In fact, to derive QMBS Hamiltonians, a natural starting point may be to consider Hamiltonians $H = A + B$ and devise rules such that

¹More precisely, the existence of a subspace \mathbb{S} such that $[A^a, B^b]\mathbb{S} = 0$ for arbitrary integers a, b is a sufficient and necessary condition for the existence of common eigenstates of A and B

A, B have a finite set of common, low-entanglement eigenstates. Importantly, the connection to an underlying automaton further guarantees that $e^{iAn} = \mathbb{1}$ for some integer n , and forces the eigenvalues of A (and similarly B) to be equidistant in energy, another crucial property of QMBSs which leads to observable many body revivals. (In a separate work, it will be shown that all mid-spectrum excited states of the spin-1 AKLT model can be found by finding common eigenstates of appropriate partitions [41].)

Beyond providing us with some principles to construct new QMBS Hamiltonians, the reference to automata also sheds light on the possible mechanism of decay of revivals in imperfect QMBSs. Two putative timescales emerge. First, the terms of the BCH expansion neglected in H_{eff} give rise to leakage from ideal transition between orbit states as predicted by the automaton circuit; the corresponding timescale τ_l is governed by the inverse of $\|(1 - P_o)C_nP_o\|$ (for some finite n), and second, a prethermal timescale $\tau_p \sim e^{n_0}$ emerges that justifies the truncation of H_{eff} to finite order—although the rules are designed to suppress BCH terms on orbit states, they eventually begin to grow at some higher order n_0 . We find evidence of such phenomenology in the PXP model. In particular, there is an associated Floquet automaton [27] which yields the PXP Hamiltonian upon truncation of the BCH series. We find that BCH terms initially *decrease* with increasing order n , characteristic of the amplitude of terms in the Floquet-Magnus (FM) expansion [9] in the high frequency limit, with a period $T < 1$. This behavior is suggestive of a prethermalization [39, 33, 1, 4] window $\tau_p \sim e^{1/T}$ wherein a truncated Hamiltonian can be justified. The parameter T is an emergent timescale that comes from the suppression of commutators in our case and is not intrinsic to the two two-layer automaton which has a unit drive period. Next, we also find that adding higher order BCH terms to the PXP model improves revivals, up to the order above which the BCH series starts diverging again. Furthermore, these additional BCH terms correspond well with terms other authors have found using symmetry arguments in helping improve revivals in the PXP model [13, 29]. In this setup, the amplitude of these terms is fixed by the BCH expansion and not numerical optimization.

This manuscript is organized as follows. In Sec. 5.1, we detail the two-layer automata circuits we consider, with $U_F = U_A U_B$, discuss the fragmentation of the Hilbert space into sets of orbits, and the Floquet eigenstates of this system. We then discuss how we define

the local Hamiltonians A , and B from such automata. Sec. 5.2 describes how we obtain a set of rules that can be used to generate scarred eigenstates in the effective Hamiltonian $H_{\text{eff}} = A + B$ and in particular embed certain (arbitrarily chosen) computational basis states in this scarred subspace. Sec. 5.3 then describes a series of new models QMBS-A,B,C that we arrive at, using the methodology proposed, along with the PXP model. In Sec. 5.4, we first provide evidence that the models show scar phenomenology and are non-integrable. The models QMBS-A,B,C exhibit successively stronger revivals (with QMBS-C exhibiting perfect revivals), in accordance with the fact that higher order BCH terms are more strongly suppressed in each successive model as per our construction. In Sec. 5.5, we discuss the amplitude of terms in the BCH expansion which connects the automaton to the Hamiltonian—for the PXP model, we find the amplitude of these terms show similar non-monotonic behavior expected in systems driven at high frequencies, indicating the possibility of a prethermalization window; adding more BCH terms to the PXP model also appears to improve revival strength and regularity. The evidence for such behavior is, however, limited in the other models we study. We end with Sec. 5.6 where we discuss some questions that are raised by this approach and which need further analysis, besides summarizing our findings.

5.1 Underlying cellular automaton and associated Hamiltonian

5.1.1 Physical setting

The quantum cellular automata considered in this work can be represented by a unitary circuit composed of two layers acting on a one-dimensional chain of L qubits with periodic boundary conditions. The two layers combined are denoted by U_F , as shown in Fig. 5.1(a). Each layer is composed of local unitary gates U_0 that permute the computational basis states of the Hilbert space on which they act locally (the gates are chosen to have support on 4 qubits in this work) as well as multiplying them by a phase ph_q , see Fig, 5.2. Furthermore it is assumed that there exists an integer n such that $U_0^n = \mathbb{1}$ which follows naturally from the permutation structure of the unitary U_0 provided the phases accrued also satisfy

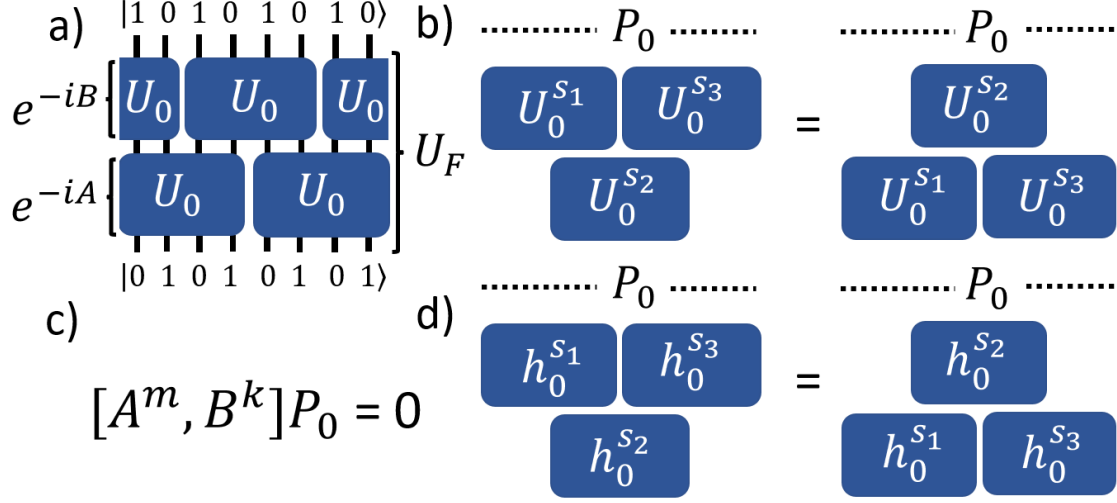


Figure 5.1: a) A quantum cellular automaton (Floquet unitary U_F) that converts one Néel state to another; b) and d) Local commutation rules of Type I and II respectively enforced on the orbit subspace; c) Global rules.

certain conditions; see Sec. 5.1.2. As mentioned in the introduction, having $U_{0,j}^n = \mathbb{1}$, with n finite is key to obtaining a scar subspace with equidistant eigenvalues embedded in an otherwise thermalizing spectrum. In the case of the U_0 considered in this work, U_F itself is a permutation of the set of computational basis states that spawn the entire Hilbert space. This implies that U_F can be decomposed into a set of disjoint cycles containing successive computational basis states obtained upon successive application of U_F to a given state, see Fig. 5.3. This fact can be used to solve exactly for the Floquet eigenstates of U_F , as discussed in Sec. 5.1.2.

The first layer of the circuit can be described as the exponential of a Hamiltonian B such that e^{-iB} yields the first layer of the circuit. Similarly, the second layer is associated with a Hamiltonian A , see Fig. 5.1(a). The exact definition of A and B is given in Sec. 5.1.3.

The sites on which the automata acts are labeled with the index $j \in \{1, 2, 3, 4, \dots, L\}$. The local unitary gate $U_{0,j}$ is defined to act on the sites $\{j, j+1, j+2, j+3\}$. With this notation, the unitaries corresponding to the first and second layers are

$$e^{-iB} = \prod_{j=1}^{L/4} U_{0,4j-1}, \quad e^{-iA} = \prod_{j=1}^{L/4} U_{0,4j-3}; \quad (5.1)$$

see Fig. 5.1 (a).

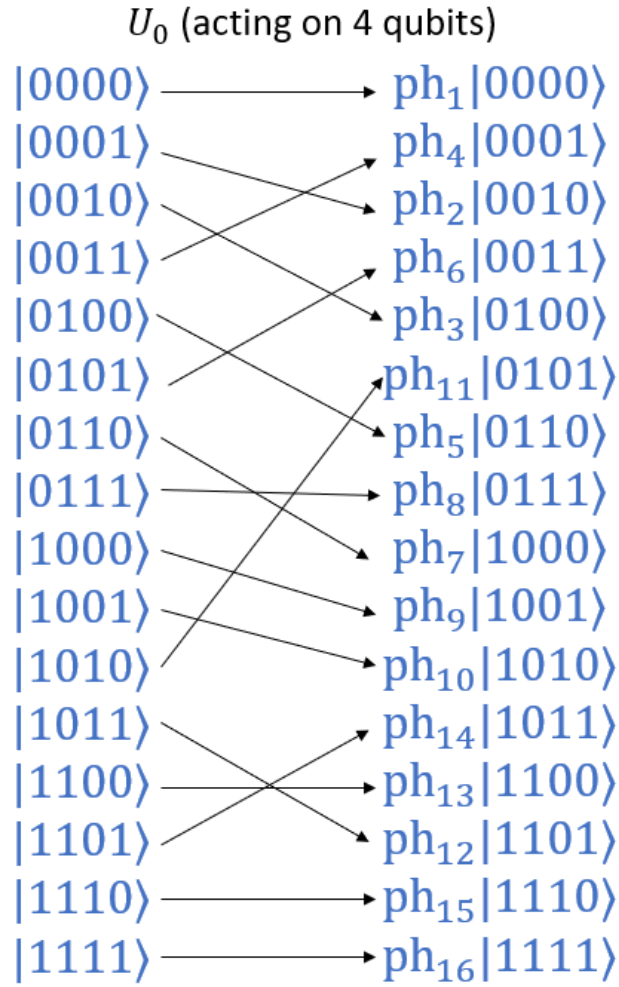


Figure 5.2: Example of a permutation gate U_0 acting on 4 adjacent qubits.

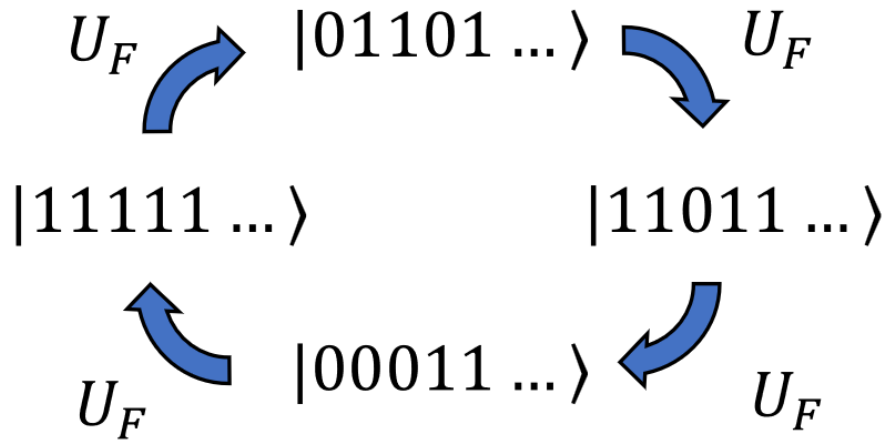


Figure 5.3: Example of a cycle of length 4 produced by the quantum cellular automaton U_F

5.1.2 Eigenstates and eigenvalues of U_F

The eigenstates of U_F can be obtained from the cycles that the computational basis states undergo upon evolution by U_F . Indeed, suppose that U_F produces a cycle of length l given by the sequence of computational basis states $|q\rangle \rightarrow |\sigma(q)\rangle \rightarrow |\sigma^2(q)\rangle \dots |\sigma^{l-1}(q)\rangle \rightarrow |q\rangle$ where $|q\rangle$ represents the q^{th} computational basis state, and $\sigma^n(q)$ corresponds to the n consecutive applications of the permutation σ associated with U_F on the state $|q\rangle$ (U_F simply permutes the computational basis states up to a phase). Supposing that the unitary U_F only has matrix elements 0 or 1 (no phase is acquired due to U_F), one directly observes that the quantum state $|q\rangle + |\sigma(q)\rangle + \dots + |\sigma^{l-1}(q)\rangle$ is an eigenstate of the Floquet unitary with an eigenvalue of 1. More generally, it is easy to show that states of the form

$$|m, q_1\rangle = \frac{1}{\sqrt{l}} \sum_{k=0}^{l-1} e^{i\alpha_k} U_F^k |q_1\rangle \quad (5.2)$$

with

$$\begin{aligned} \beta &= \frac{\Phi + 2\pi m}{l} & \Phi &= -i \log(\langle q_1 | U_F^l | q_1 \rangle) \\ \alpha_k &= -k\beta & m &\in \{0, 1, \dots, l-1\} \end{aligned} \quad (5.3)$$

form a complete orthonormal eigenbasis of U_F , where $|q_1\rangle$ in Eq. 5.2 is a computational basis state appearing in a given cycle of length l and $e^{i\beta}$ is the eigenvalue of the state $|m, q_1\rangle$. For a given $|q_1\rangle$, distinct values of m yield distinct eigenvalues which implies that the obtained states are mutually orthogonal. Eigenstates corresponding to different cycles are composed of different computational basis states, so they necessarily are orthogonal to each other. Thus, a complete orthonormal basis can be obtained by selecting a representative state $|q_1\rangle$ in each cycle, and the eigenvalue m . Note that if an integer n such that $U_0^n = \mathbb{1}$ is to exist, it must be the case that *all* the β are integer fractions of 2π which is equivalent to requiring that all Φ associated with distinct $|q_1\rangle$ are an integer fraction of 2π .

Eqs. (5.2,5.3) show that Floquet eigenstates $|q_1, m\rangle$, with $m \in \{0, \dots, l-1\}$, when viewed as eigenstates of a corresponding Floquet Hamiltonian H_F (such that $e^{-iH_F t} = U_F$), correspond to eigenstates separated by a multiple of the constant energy difference $\Delta E = \frac{2\pi}{l}$. The computational basis states that appear in a given cycle of small length are thus ideal candidates as area-law entanglement states to embed in a physical model related to U_F . How

this can be done is discussed in Sec. 5.2. First, however, we discuss how Hamiltonians A and B are precisely defined from the two-layer automata considered.

5.1.3 Local Hamiltonians from quantum cellular automata

We note that Hamiltonians A and B are not uniquely defined from U_F —there exist multiple Hamiltonians that yield U_F when exponentiated. Since a single layer of U_F is composed of spatially decoupled unitaries U_0 , we can also construct A and B from local Hamiltonians satisfying

$$h_{0,j} = i \log U_{0,j}. \quad (5.4)$$

This equation alone does not uniquely specify $h_{0,j}$, but this ambiguity can be lifted by writing $U_{0,j}$ in terms of the orthonormal Floquet eigenstates obtained from Eq. 5.2 which yields

$$U_{0,j} = \sum_{k=1}^{2^4} e^{i\beta_k} |\beta_k\rangle \langle \beta_k|. \quad (5.5)$$

$|\beta_k\rangle$ are the Floquet eigenstates of $U_{0,j}$ as defined in Eq. 5.2. $h_{0,j}$ is then defined as

$$h_{0,j} \equiv - \sum_{k=1}^{2^4} \tilde{\beta}_k |\beta_k\rangle \langle \beta_k| \quad (5.6)$$

where $\tilde{\beta}_k$ is $-i$ times the principal logarithm of $e^{i\beta_k}$, implying $\tilde{\beta}_k \in (-\pi, \pi]$. The Hamiltonian which we will force to support quantum scars is the strictly local Hamiltonian

$$H = A + B \quad (5.7)$$

with $A = \sum_{j=1}^{L/4} h_{0,4j-3}$ and $B = \sum_{j=1}^{L/4} h_{0,4j-1}$. A can thus be understood as the logarithm of the second layer of U_F and B as the logarithm of the first layer; see Fig. 5.1(a).

5.1.4 Distinction between U_F and $e^{-i(A+B)}$

So far nothing guarantees that the extracted Hamiltonian $A + B$ mimics the underlying quantum cellular automaton in any meaningful way. This is because the original Floquet

unitary $U_F = e^{-iA}e^{-iB}$ and the time evolution operator associated with the $A + B$ Hamiltonian $e^{-i(A+B)}$ at $t = 1$ are not equal in general. The reason for this discrepancy can be understood once we interpret the automaton U_F as the result of a periodic driving of the system. Indeed, successive applications of the Floquet unitary U_F to a quantum state $|\psi\rangle$ is equivalent to the time evolution at even integer times resulting from the stroboscopic driving of the quantum system with the Hamiltonians $H = A$, $H = B$ for equal times. The floquet unitary U_F can alternatively be captured by a Floquet Hamiltonian H_F such that $U_F = e^{-iH_F}$; H_F is formally given by the Floquet-Magnus expansion. In particular, this expansion reduces to the well known Baker-Campbell-Hausdorff (BCH) expansion in the case of the driving described above.

The first few terms of the BCH expansion are given by

$$H_F = A + B - \frac{i}{2}[A, B] - \frac{1}{12}([A, [A, B]] - [B, [A, B]]) + \dots \quad (5.8)$$

The i^{th} BCH term is denoted by C_i , where the 0^{th} order term is $A + B$. For instance,

$$C_0 = A + B \quad C_1 = \frac{-i}{2}[A, B] \quad C_2 = -\frac{1}{12}([A, [A, B]] - [B, [A, B]]), \dots \quad (5.9)$$

Importantly, the amplitude of terms in this series quickly diverges, owing to the proliferation of the number of non-zero commutators of local terms. This implies that H_F cannot generally be approximated by its first order term $A+B$ and thus $e^{-i(A+B)}|\psi\rangle \neq e^{-iA}e^{-iB}|\psi\rangle$ in general. However, as we will show in the next sections, it is possible to obtain sets of rules which, if all or part of them are satisfied, ensure that some of the subspaces associated with cycles of U_F are preserved or approximately preserved by $H = A + B$. One useful set of local rules can be obtained by realizing that the local Hamiltonians $h_{0,j}$ assume a special decomposition in terms of powers of $U_{0,j}$ as we discuss next.

5.2 Rules that guarantee the presence of quantum scars

5.2.1 Writing H as a linear superposition of powers of simple unitary gates

The local unitary gates considered in this work are chosen such that there exists an integer n for which $U_{0,j}^n = \mathbb{1}$. Provided $U_{0,j}^n = \mathbb{1}$, along with the definition of $h_{0,j}$ specified in Eq. 5.6, one can show that

$$h_{0,j} = i \log U_{0,j} = \sum_{k=0}^{m-1} c_k U_{0,j}^k \quad (5.10)$$

for some set of coefficients c_k . An exact recipe for obtaining the coefficients c_k is given in App. C; we note here that in Eq. (5.10), the integer $m \leq n$ (where $U_{0,j}^n = \mathbb{1}$). In other words, it is possible that not all powers of $U_{0,j}$ up to n are required to construct $h_{0,j}$. This is the case for the PXP model for which $U_{0,j}^4 = \mathbb{1}$, but $\mathbb{1}, U_{0,j}, U_{0,j}^2$ are sufficient to obtain $h_{0,j} = \text{PXP}_j$; see Tab. H.1 for a definition of $U_{0,j}$ and $h_{0,j}$ in the PXP model.

5.2.2 Global rules

Eq. (5.10) can be leveraged to construct a set of rules that will ensure that some chosen area law entanglement states are common eigenstates of A and B . Indeed, provided a decomposition of $h_{0,j}$ in terms of powers of $U_{0,i}$, one can rewrite A and B as

$$A = \sum_{j=1}^{L/4} \sum_{k=1}^n c_k U_{0,4j-3}^k, \quad (5.11)$$

$$B = \sum_{j=1}^{L/4} \sum_{k=1}^n c_k U_{0,4j-1}^k. \quad (5.12)$$

Next, consider the subspace spanned by a specific cycle of U_F that has length l and define the projector P_0 to be the projector onto the computational basis states that compose the cycle

$$P_0 = \sum_{k=1}^l |\sigma^k(q)\rangle \langle \sigma^k(q)|. \quad (5.13)$$

The states that appear in this cycle are the area-law entanglement states chosen here to be embedded as a linear superposition of common eigenstates of A and B . A sufficient condition

to embed the subspace spawned by P_0 is to enforce that $e^{-i(A+B)}P_0$ yields the same result as $e^{-iA}e^{-iB}P_0$. For this to be true, it is sufficient to require that

$$[A^a, B^b]P_0 = 0 \quad \forall a, b \quad (5.14)$$

where a, b are positive integers. This set of rules is a necessary and sufficient condition for the existence of a set of common eigenstates [57] of A and B denoted here by \mathbb{S} which will spawn the computational basis states that appear in P_0 . Such rules are dubbed global rules, see Fig. 5.1(c). Satisfaction of all such global rules ensures QMBS phenomenology since the dynamical evolution of the computational basis states that appear in P_0 undergo a periodic cycle in accordance with the dynamical evolution prescribed by the underlying Floquet automaton instead of quickly thermalizing. Furthermore, provided the dimension of the common eigenstate subspace \mathbb{S} grows at most polynomially with system size, then the common eigenstates of A and B will necessarily have low entanglement since linear combinations of such states must spawn the low entanglement states that appear in P_0 . As a consequence, the common eigenstates of A and B appear as scar eigenstates of $H = A + B$ and form scar towers.

Since A and B are sums of spatially decoupled unitary gates, powers of A and B are given by

$$\begin{aligned} A^a &= \left(\sum_{j=1}^{L/4} \sum_{k=1}^n c_k U_{0,4j-3}^k \right)^a \\ B^b &= \left(\sum_{j=1}^{L/4} \sum_{k=1}^n c_k U_{0,4j-1}^k \right)^b \end{aligned} \quad (5.15)$$

and generic terms in $A^a B^b P_0$ take the form

$$\prod_{j=1}^{L/4} U_{0,4j-3}^{\alpha_{4j-3}} \prod_{j=1}^{L/4} U_{0,4j-1}^{\alpha_{4j-1}} P_0 \quad (5.16)$$

up to a multiplicative constant, for some set of positive integers α_j including 0. Thus, in order to satisfy the identity $[B^b, A^a]P_0 = 0$ for arbitrary integers a and b , it is sufficient to require that the expression

$$\prod_{j=1}^{L/4} U_{0,4j-3}^{\alpha_{4j-3}} \prod_{j=1}^{L/4} U_{0,4j-1}^{\alpha_{4j-1}} P_0 = \prod_{j=1}^{L/4} U_{0,4j-1}^{\alpha_{4j-1}} \prod_{j=1}^{L/4} U_{0,4j-3}^{\alpha_{4j-3}} P_0 \quad (5.17)$$

is satisfied for all possible set of α_j . Note that a distinct condition can be obtained by considering the alternate representation

$$A^a = \left(\sum_{j=1}^{L/4} h_{0,4j-3} \right)^a \quad B^a = \left(\sum_{j=1}^{L/4} h_{0,4j-1} \right)^b \quad (5.18)$$

which leads to the condition

$$\prod_{j=1}^{L/4} h_{0,4j-3}^{\alpha_{4j-3}} \prod_{j=1}^{L/4} h_{0,4j-1}^{\alpha_{4j-1}} P_o = \prod_{j=1}^{L/4} h_{0,4j-1}^{\alpha_{4j-1}} \prod_{j=1}^{L/4} h_{0,4j-3}^{\alpha_{4j-3}} P_o. \quad (5.19)$$

As will be discussed next, conditions (5.17) and (5.19) lead to distinct sets of local rules, dubbed rules of type I and II respectively.

5.2.3 Local rules of type I

Conditions (5.17) and (5.19) can be further reduced to simple local rules that only involve a small set of unitary gates. The set of local rules associated with condition (5.17) is given by

$$\begin{aligned} U_{0,j}^{s_1} U_{0,j+4}^{s_3} U_{0,j+2}^{s_2} |\sigma^k(q)\rangle &= U_{0,j+2}^{s_2} U_{0,j}^{s_1} U_{0,j+4}^{s_3} |\sigma^k(q)\rangle \\ \forall s_i \in \{0, 1, 2, \dots, n-1\}, \quad \forall j \in \{1, 3, 5, \dots, L-1\} & \\ U_{0,j}^n &= \mathbb{1} \quad \forall k \in \{1, 2, \dots, l\} \end{aligned} \quad (5.20)$$

where $|\sigma^k(q)\rangle$ are the states that appear in P_0 . These rules are denoted rules of type I [see Fig. 5.1(b)] and a graphical proof that they indeed ensure that Eq. (5.17) is satisfied is provided in Fig. 5.4. A remarkable property of type I rules is that they are finite and independent of the system size if the states $|\sigma^k(q)\rangle$ are translationally invariant. More precisely, given the smallest integer m such that $S^{2m} |\sigma^k(q)\rangle = |\sigma^k(q)\rangle$ where S is the operator translating all sites by one to the right, then the total number of sites j one needs to check for the rules associated with the state $|\sigma^k(q)\rangle$ is reduced to $j \in \{1, 3, \dots, 2m-1\}$.

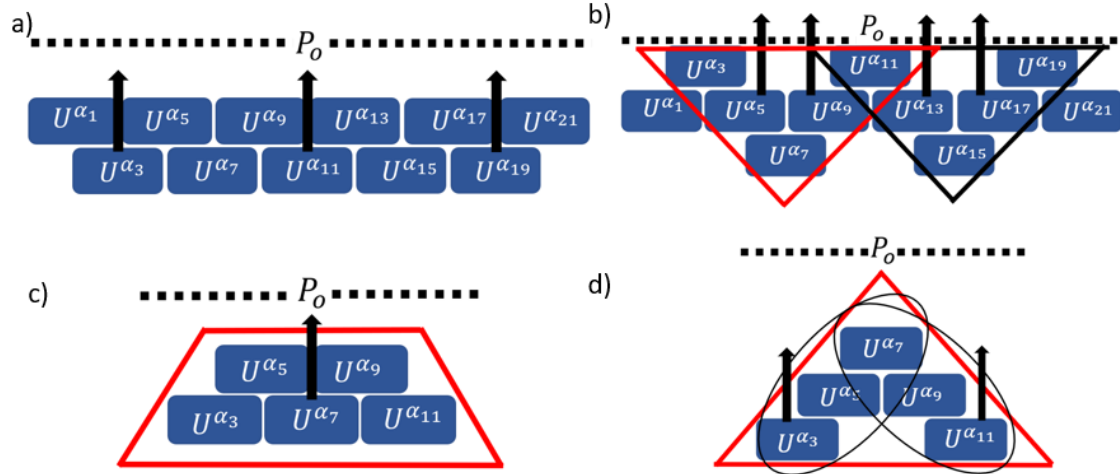


Figure 5.4: a) Half the gates from the second layer are sent forward producing a circuit with three layers. b) Within each triangle (focusing on the red one), gates from the second layer are sent forward. c) Within the resulting configuration, the middle gate of the second layer is sent to the first layer d) The side gates are sent from the third layer to the first layer (Note that this is a 2 step operation for each side gate). The resulting arrangement of gates shows that by making use of the commutation rules, it is possible to send gate $U_0^{\alpha_7}$ from the third layer to the first layer in b). Repeating this procedure on each triangle proves that satisfying the local unitary rules is sufficient to ensure that $[A^a, B^b]P_0 = 0$ for arbitrary integers a and b

5.2.4 Local rules of type II

If condition (5.19) is considered instead of condition (5.17), one obtains a different set of local rules given by

$$\begin{aligned}
 h_{0,j}^{s_1} h_{0,j+4}^{s_3} h_{0,j+2}^{s_2} |\sigma^k(q)\rangle &= h_{0,j+2}^{s_2} h_{0,j}^{s_1} h_{0,j+4}^{s_3} |\sigma^k(q)\rangle \\
 \forall s_i \in \{0, 1, 2, \dots, n-1\} \quad \forall j \in \{1, 3, 5, \dots, L-1\} & \\
 U_{0,j}^n &= \mathbb{1} \quad \forall k \in \{1, 2, \dots, l\}
 \end{aligned}
 \tag{5.21}$$

which are denoted rules of type II, see Fig. 5.1(d). A key distinction with rules of type II is that nothing ensures the existence of an integer n such that $h_{0,j}^n = \mathbb{1}$. However, it is easy to see from the decomposition (5.10) that $h_{0,j}^n$ can always be written as a linear superposition of smaller powers of $h_{0,j}$; this restricts s_i to be less than n ; see App. G for more details. As discussed in Sec. 5.2.1, there is a possibility that not all powers of $U_{0,j}$ up to n are actually required to build $h_{0,j}$. This is also the case when considering a decomposition of $h_{0,j}$ in terms of smaller powers of itself. Indeed, there can exist an integer m smaller than n such that $h_{0,j}^m$ can be written as a linear superposition of smaller powers of $h_{0,j}$ which can further reduce the set of integers s_i one actually needs to check. For instance, this is true in the PXP model for which $h_{0,j}^3 = \frac{\pi^2}{4} h_{0,j}$. See Tab. H.1 for the definition of the $h_{0,j}$ associated with the PXP model.

Another key distinction between rules of type I and rules of type II is that whenever a rule of type I is broken, BCH terms at all orders become non-vanishing. While since the BCH expansion is organised in terms of commutators of $h_{0,j}$, higher powers of $h_{0,j}$ in commutators only emerge at higher order in the BCH expansion. Thus, satisfying lower powers of the type II rules may be important in enforcing prethermal behavior and stabilising scar phenomenology in the truncated Hamiltonian (although there is no distinction between the two set of rules when all of them are satisfied).

A final reason to consider type II rules is that one could in principle completely ditch any reference to automata and try to find Hamiltonians which satisfy these local rules to yield common eigenstates with low entanglement—the real purpose of the connection to an underlying automaton is to ensure scar phenomenology and to restrict the search for $h_{0,j}$ to Hamiltonians which yield a finite set of distinct operators $h_{0,j}^i$ with $i \in \{0, \dots, n-1\}$

5.3 Building models that satisfy local rules

It was shown in Sec. 5.2 that satisfying all local rules is sufficient to ensure the protection of the subspace spanned by the states that appear in P_0 .

We note that the rules rely on two choices: i) the unitary U_0 which is determined, in the case we consider, by the permutation it generates over computational basis states, along with the phases accrued, and ii) the set of computational basis states $|\sigma^k(q)\rangle$, $k = 1, \dots, l$, we choose to embed in the putative scar subspace, the projector to which is given by P_0 . Now, given the above structure, we note that the rules of type I, given in Eq. (5.20), are either exactly satisfied (for a given choice of s_1, s_2, s_3 and $|\sigma^k(q)\rangle$, or the left and right hand side of Eq. (5.20) produce entirely different computational basis states and/or phases. Thus, we can simply count the number of rules that are satisfied. The situation is trickier for the set of local rules given in Eq. (5.21), in that the local Hamiltonians $h_{0,j}$ will generically produce entangled states upon acting on computational basis states in P_0 , and it may be useful to quantify the violation of the rules using a suitable inner product between the left and right hand sides of Eq. (5.21). For simplicity, for a search of model Hamiltonians with scar subspaces which we perform next, we restrict ourselves to rules of type I and simply enumerate the number of rules (out of a maximum determined by enumerating the allowed values of s_1, s_2, s_3, k).

5.3.1 Explicit model search

There is a total of $16!$ permutations of the set of computational basis states that spawn the 4 qubits Hilbert space on which $U_{0,j}$ acts and if phase is allowed, the space of possibilities is effectively infinite. The size of the search space makes it prohibitively hard to study exhaustively. To remedy this problem, we choose to restrict U_0 to act trivially on the rightmost qubit while also preventing phase from being acquired. This produces a set of $8!$ possible unitary gates which can be studied exhaustively. The search space was further reduced by considering unitary gates such that $U_{0,j}^6 = \mathbb{1}$. The chosen subspace to protect is given by the two Néel states $|q\rangle = |1, 0, 1, \dots\rangle$, $|\sigma(q)\rangle = |0, 1, 0, \dots\rangle$, such that $U_F |q\rangle = |\sigma(q)\rangle$, $U_F |\sigma(q)\rangle = |q\rangle$. This constrained search results in three models presented in Tab. 5.1

which satisfy 70/350, 246/350 and 350/350 of the applicable type I rules, respectively. The unitary gates are represented in Tab. 5.1 by a permutation and a phase map (in this case trivial) which are defined in App. A. The total number of relevant rules for each model is discussed in App. B

5.3.2 PXP model

Outside of this search, the PXP model is also studied in association with an underlying automaton. The circuit geometry is different due to the fact that the PXP model has a unit cell composed of one qubit, i.e $U_F = \prod_j^{L/2} U_{0,2j-1} \prod_j^{L/2} U_{0,2j}$ and U_0 in this case is a Toffoli gate which acts on three qubits. Note also that adjacent gates $U_{0,j}, U_{0,j+2}$ commute in the PXP model, so the first and second layer can be seen as a product of decoupled gates and the formalism developed in Sec. 5.2 applies. Finally, for this model, the protected cycle is composed of three states instead of two and given by $|q\rangle = |1, 1, 1, 1, \dots\rangle$, $|\sigma(q)\rangle = |0, 1, 0, 1, \dots\rangle$, $|\sigma^2(q)\rangle = |1, 0, 1, 0, \dots\rangle$.

5.4 Numerical signature of quantum scars

5.4.1 Revival strength and signs of quantum scarring

As intuitively expected, the number of type I rules that are satisfied is correlated with the strength of the revivals. For instance, QMBS-B shows stronger, longer lasting and more coherent revivals compared to QMBS-A as can be seen in Fig. 5.5 where the revivals are studied by considering the participation ratio (PR) of the time-evolved state $e^{-i(A+B)t} |\mathbb{Z}_2\rangle$ where $|\mathbb{Z}_k\rangle = |\underbrace{0, 1, 1, \dots, 1}_k, \underbrace{0, 1, 1, \dots, 1}_k, \dots\rangle$. The PR is evaluated in the basis of computational basis states $|q\rangle$ and is defined as $\text{PR} [|\psi\rangle] = \sum_{q=1}^{2^L} |\langle q|\psi\rangle|^4$ where $|\psi\rangle$ is assumed to be normalized. A PR close to 1 indicates that the system is largely in one computational basis state while a $\text{PR} \sim 1/N_{\text{eff}}$, where the effective dimension N_{eff} is defined here as the number of computational basis states connected to the Néel state by a matrix elements of some given power of H (for the exact value of N_{eff} in all the models studied, see App. E), implies relaxation. For comparison, the revival of a computational basis state that is not a Néel state

QMBS-A	
Permutation	$((3, 13, 11, 7, 9, 5), (4, 14, 12, 8, 10, 6))$
Phase	$(1, 1, 1, 1, 1, 1, 1, 1, 1, 1, 1, 1, 1, 1, 1, 1)$
$h_{0,j}$ decomposition	$(\frac{\pi}{6} + i\frac{\pi}{2\sqrt{3}})U_{0,j} + (-\frac{\pi}{6} - i\frac{\pi}{6\sqrt{3}})U_{0,j}^2 + \frac{\pi}{12}U_{0,j}^3 - \frac{\pi}{12}U_{0,j}^0 + \text{h.c}$
$U_{0,j}^n = I$	$n = 6$
Orbit	$ q\rangle = 1, 0, 1, 0, \dots\rangle, \sigma(q)\rangle = 0, 1, 0, 1, \dots\rangle$
Rule ratio type I	$70/350$
QMBS-B	
Permutation	$((1, 15), (2, 16), (3, 9, 5), (4, 10, 6), (7, 13, 11), (8, 14, 12))$
Phase	$(1, 1, 1, 1, 1, 1, 1, 1, 1, 1, 1, 1, 1, 1, 1, 1)$
$h_{0,j}$ decomposition	$(\frac{\pi}{6} + i\frac{\pi}{2\sqrt{3}})U_{0,j} + (-\frac{\pi}{6} - i\frac{\pi}{6\sqrt{3}})U_{0,j}^2 + \frac{\pi}{12}U_{0,j}^3 - \frac{\pi}{12}U_{0,j}^0 + \text{h.c}$
$U_{0,j}^n = \mathbb{1}$	$n = 6$
Orbit	$ q\rangle = 1, 0, 1, 0, \dots\rangle, \sigma(q)\rangle = 0, 1, 0, 1, \dots\rangle$
Rule ratio type I	$246/350$
QMBS-C	
Permutation	$((3, 5), (4, 6), (7, 15, 9), (8, 16, 10), (11, 13), (12, 14))$
Phase	$(1, 1, 1, 1, 1, 1, 1, 1, 1, 1, 1, 1, 1, 1, 1, 1)$
$h_{0,j}$ decomposition	$(\frac{\pi}{6} + i\frac{\pi}{2\sqrt{3}})U_{0,j} + (-\frac{\pi}{6} - i\frac{\pi}{6\sqrt{3}})U_{0,j}^2 + \frac{\pi}{12}U_{0,j}^3 - \frac{\pi}{12}U_{0,j}^0 + \text{h.c}$
$U_{0,j}^n = \mathbb{1}$	$n = 6$
Orbit	$ q\rangle = 1, 0, 1, 0, \dots\rangle, \sigma(q)\rangle = 0, 1, 0, 1, \dots\rangle$
Rule ratio type I	$350/350$
PXP	
Permutation	$((11, 15), (12, 16))$
Phase	$(1, 1, 1, 1, 1, 1, 1, 1, 1, 1, i, i, 1, 1, i, i)$
$h_{0,j}$ decomposition	$(\frac{\pi}{4} + i\frac{\pi}{4})U_{0,j} - \frac{\pi}{8}U_{0,j}^2 - \frac{\pi}{8}I + \text{h.c}$
$U_0^n = \mathbb{1}$	$n = 4$
Orbit	$ q\rangle = 1, 1, 1, 1, \dots\rangle, \sigma(q)\rangle = 0, 1, 0, 1, \dots\rangle, \sigma^2(q)\rangle = 1, 0, 1, 0, \dots\rangle$
Rule ratio type II	$38/48$

Table 5.1: Characteristics of the models

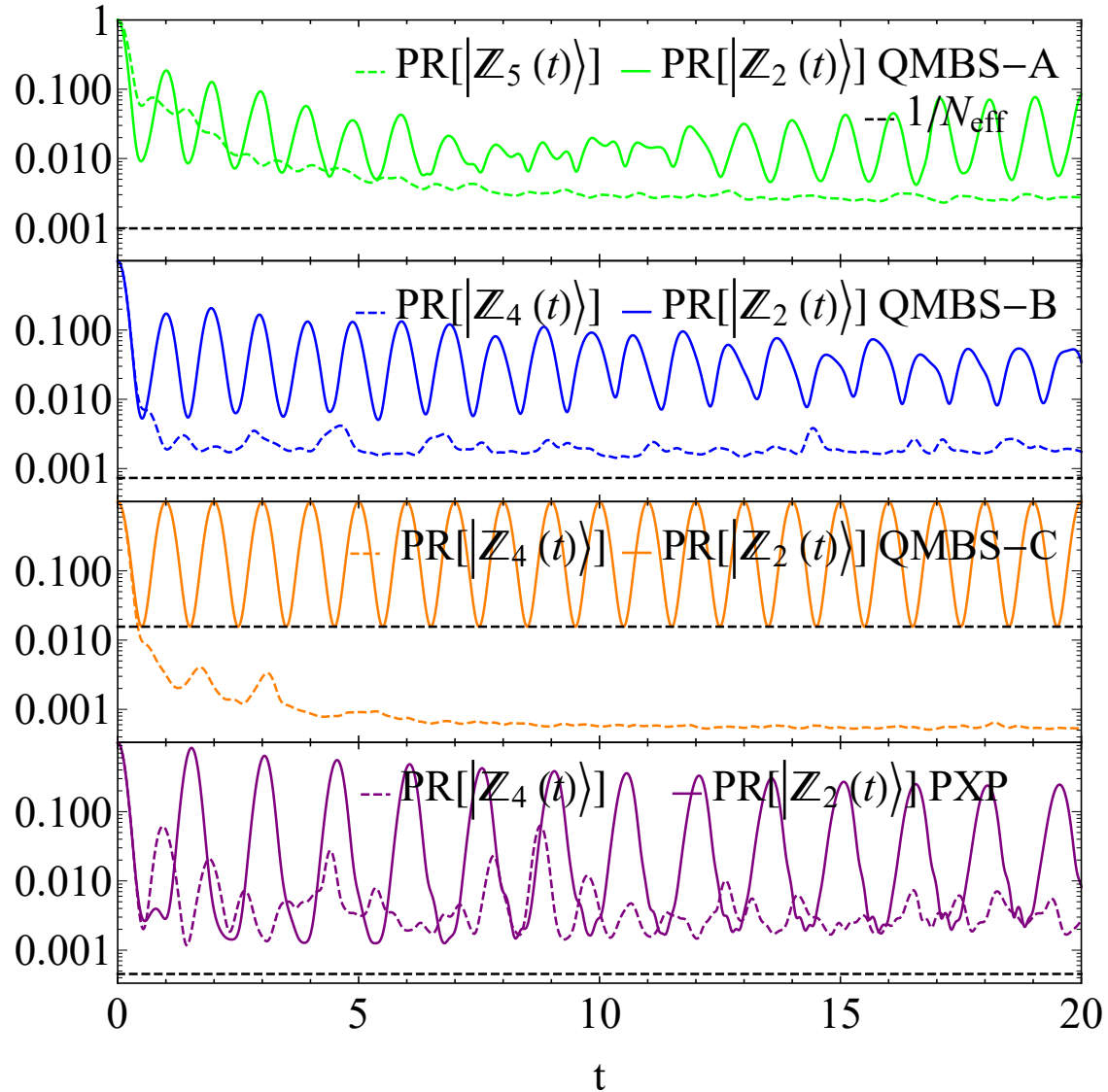


Figure 5.5: Revivals of the Néel state (solid line) and of a generic state (dashed line) showed on a log scale as seen from the PR of the time-evolved state for the various models studied. $L = 10, 12, 12, 16$ and $N_{\text{eff}} = 1024, 1366, 64, 2207$ for QMBS-A, QMBS-B, QMBS-C and PXP respectively.

is showed in Fig. 5.5, in which case it can be seen that the state quickly thermalizes. The exact scar model QMBS-C supports a spectrum generating algebra like many other exact QMBS models, and can also be viewed as an exact embedding which is discussed in App. D.

The presence of quantum scars in the models QMBS-A/B/C can also be seen from distribution plots of the inverse participation ratio $\text{IPR}[|\psi\rangle] = 1/\text{PR}[|\psi\rangle]$ of the eigenstates of the Hamiltonian $H = A + B$ for each model against their eigenenergies, as shown in Fig. 5.7 which reveals the presence of low IPR states that are exactly equidistant in energy for the QMBS-C model and approximately equidistant in energy for the PXP, QMBS-B and QMBS-A model. Furthermore, we also identify states which have a large overlap with the Néel states; these appear to coincide with the low IPR eigenstates (indicated by black x in the figure). This strongly indicates a correlation between the number of rules of type I/II satisfied in the models and the presence of low IPR states (scar eigenstates) in the spectrum. Finally, a finite-size scaling of the revivals in the PR of the time-evolved Néel states is shown in Fig. 5.6. The minima appears to coincide well with the inverse effective Hilbert space dimension $\sim 1/N_{\text{eff}}$, indicating near complete relaxation at intermediate times. The maxima corresponding to revivals, on the other hand, decreases with increasing system size but only as $-\log(N)$ suggesting that the phenomena should be robust in the large L limit.

5.4.2 R-statistic and effective Hilbert space dimension

The level repulsion statistic, obtained as the ratio of the minimum to the maximum energy differences between successive eigenstates, $r_n = \min(\Delta E_{n+1}/\Delta E_n, \Delta E_n/\Delta E_{n+1})$ where $\Delta E_n = E_n - E_{n-1}$, $E_n \leq E_{n+1}$, can be used as a metric to determine if a given model is integrable or not, which is key to showing that the approximate scars presented here are not due to integrability. By computing all the r_n values for a given set of eigenvalues (extracted from a given symmetry sector of H) and constructing the associated probability density $P(r)$, one expects $P(r)$ to be Poissonian if the model is integrable, and characteristic of GOE/GUE ensembles if the model is non-integrable [5]. The most prominent feature of $P(r)$ for non-integrable models is suppression of $P(r)$ at r values near 0 which indicates level repulsion, a characteristic feature of non-integrable models. One can see in Fig. 5.8 that the models QMBS-A and QMBS-B show strong level repulsion and appear to closely follow

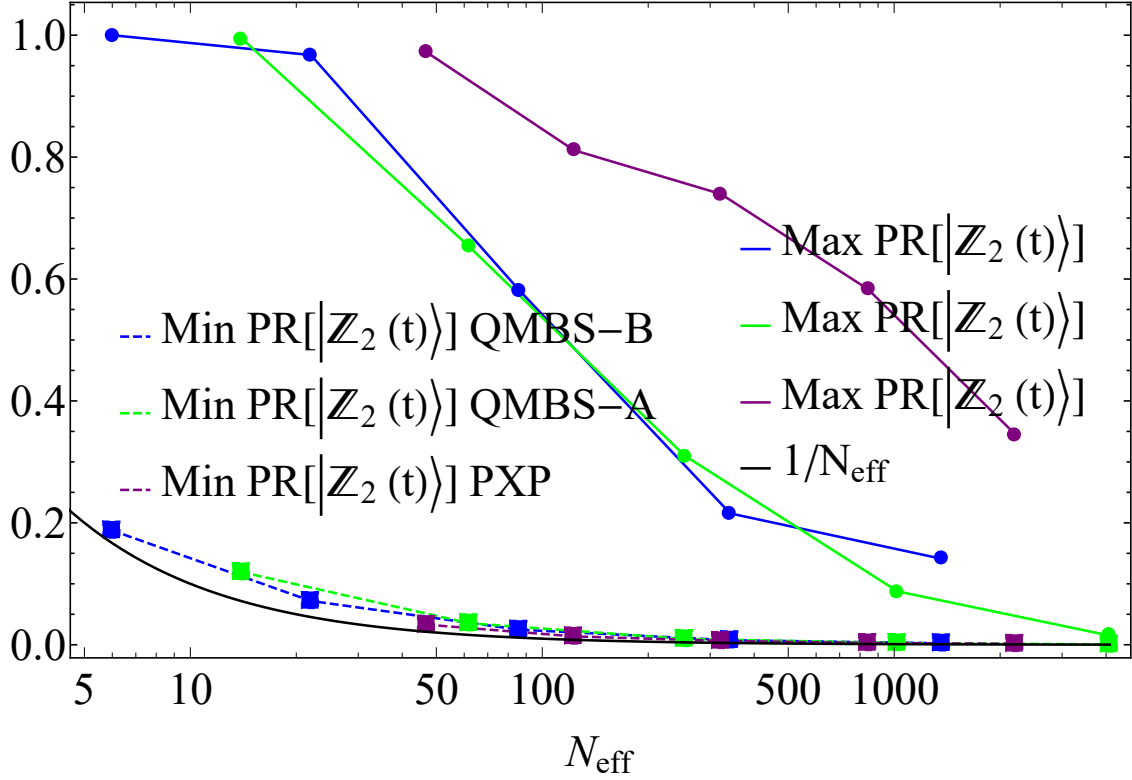


Figure 5.6: The maximum and minimum PR of the time evolved Néel states in the time range $t \in (10, 300)$ versus the effective Hilbert space dimension N_{eff} . The minimum closely follows the inverse effective Hilbert space dimension (red line) for all models. Satisfaction of more rules of type II/I appears to produce revivals that scale better with system size.

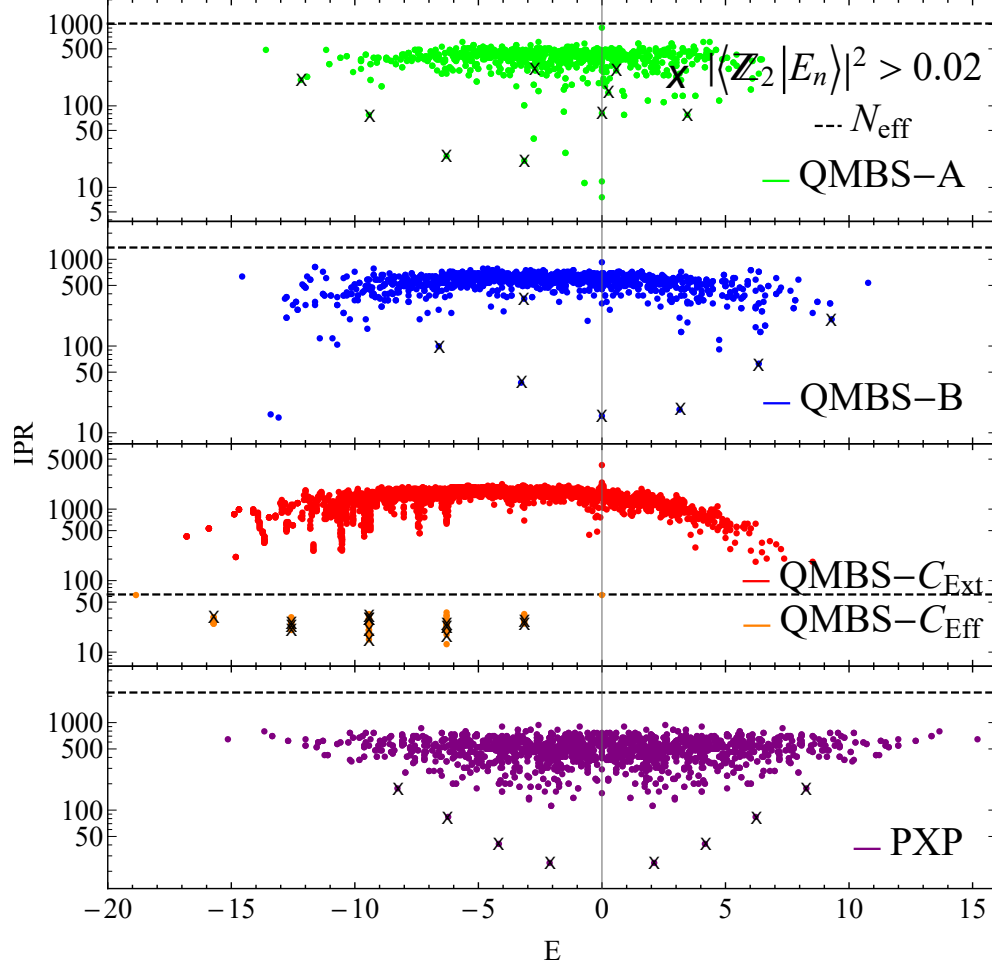


Figure 5.7: Scatter plot of IPR vs. eigenstate energy in the 4 models studied in the main text. The states marked by an x are eigenstates that have an overlap amplitude with $|\mathbb{Z}_2\rangle$ larger than 0.02. Such states appear to be approximately equally separated in energy for all the models QMBS-A/B/C which is a hallmark of quantum scarring. Similar behavior is observed in the PXP model as well noted in Ref [63]. The scar signatures appear to be more pronounced provided a larger number of rules are satisfied. The Hamiltonians used to compute the eigenstates are restricted to the computational basis states appearing in the Kyrlov subspace associated with the Néel states, except for QMBS-C for which the full Hamiltonian is used to illustrate the embedding. Red dots in the QMBS-C panel show the IPR vs. energy of the eigenstates outside the Kyrlov subspace, whilst the orange dots show the IPR vs. energy of the eigenstates inside the Kyrlov subspace. $N_{\text{eff}} = 2207, 1024, 1366, 64$, $L = 16, 12, 10, 12$ for PXP, QMBS-A, QMBS-B, QMBS-C respectively. See Sec. 5.4.2 for a precise definition of N_{eff}

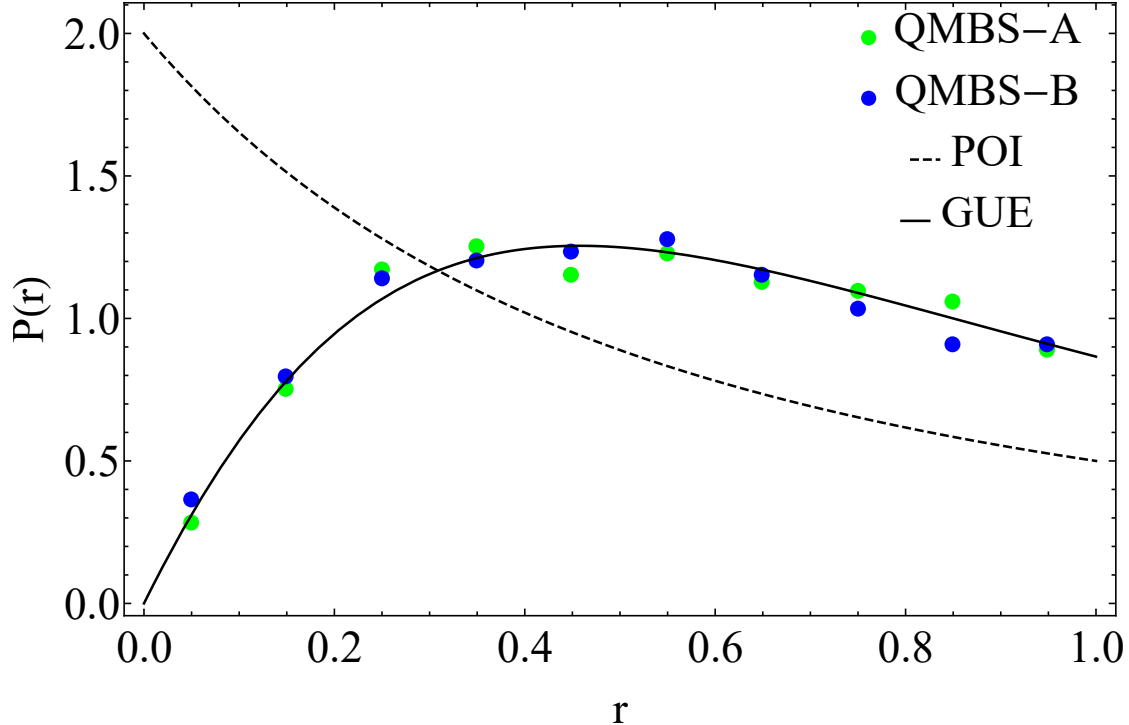


Figure 5.8: Non-integrability of model QMBS-A and QMBS-B can be seen in the suppression of $P(r)$ at small r values. Eigenvalues for QMBS-A and B are computed in the basis of computational basis states that appear in the Krylov subspace associated with the Néel states. Furthermore, the Hamiltonian is restricted to the common $+1$ eigenspace of S^2 and U_{SM} for $L = 16, 18$ which yields 4115 and 4863 eigenvalues for QMBS-A, QMBS-B respectively.

GOE predictions indicating that they are non-integrable which rules out integrability as the reason for the presence of quantum scars in the models. For a detailed discussion of the symmetry sector (containing the scar states) studied, see App. E.

5.5 BCH expansion and revivals

An important natural question in our construction is how accurately the truncated Hamiltonian $H = A + B$ captures the dynamics we expect from the associated automaton unitary $U_F = e^{-iA}e^{-iB}$. In particular, of key interest to us is ensuring that the truncated Hamiltonian captures the dynamics of the automaton in the *scar subspace*. It is clear that this is

the case if all terms in the BCH expansion, C_n , vanish on the scar subspace. Since we do not know what this subspace is exactly in our construction, instead we examine the action of C_n on the subspace of orbit states that our construction is designed to embed on to the scar subspace—recall the projector onto this subspace is denoted by P_0 .

In what follows, we will examine the typical matrix element of C_n as a function of the order of the BCH expansion n , connecting i) orbit states to other orbit states, ii) orbit states to generic states, and iii) generic states to other generic states. We will examine these terms by numerically computing $\|P_0 C_n P_0\|/l$, $\|(1 - P_0) C_n P_0\|/(l N_{\text{eff}})^{1/2}$ and $\|(1 - P_0) C_n (1 - P_0)\|/N_{\text{eff}}$, respectively. Here, $\|X\|$ denotes the Frobenius norm of the matrix X , and we divide this norm by $N_{\text{eff}} - l \approx N_{\text{eff}}$ (the Hilbert space dimension of generic states), or l (the Hilbert space dimension of orbit states) or a composite of the two to obtain the value of the typical matrix element.

We note a priori that ultimately, we would like the truncated Hamiltonian $H = A + B$ to mimic the dynamics of the Floquet automaton on a putative scar subspace on which the selected orbit states have significant overlap. Although this is true when all matrix elements of BCH terms C_n connecting scar states to generic states vanish, it is not obvious that examining the magnitude of terms in the BCH expansion is always the correct way of probing this aspect of the dynamics. For one, it may be the case that the BCH expansion may be reorganized in a way that appropriate linear combinations of C_n have small matrix elements connecting orbit states to generic states even though individually the C_n themselves have fairly large matrix elements. Second, here we attempt to examine the matrix elements between orbit states and generic computational basis states—even if these matrix elements are significant, it does not preclude the possibility that matrix elements of C_n between scar *eigenstates* of $H = A + B$ and other generic states have small amplitude. The latter depends on how well the scar eigenstates actually embed the intended orbit states. We will see that in the PXP model, where rules of type II are satisfied, the BCH expansion does indeed show suppression of matrix elements between orbit states and generic states, order by order. With this clarification, we can now discuss our numerical findings.

5.5.1 Amplitude of BCH terms and possible prethermal behavior in the PXP model

In Fig. 5.9, we plot the typical amplitude of the matrix elements of the n^{th} order BCH term C_n connecting various states in the Hilbert space. The following observations can be made—i) BCH terms connecting orbit states are heavily suppressed in the perfect scar model QMBS-C, and the PXP model, while they are suppressed only at certain specific orders in QMBS-A and QMBS-B, ii) matrix elements connecting orbit states to generic states decrease with n at first for the PXP model, before eventually increasing again, iii) in the PXP model, even matrix elements connecting generic states to other generic states surprisingly show this phenomenology, iv) for QMBS-A/B, matrix elements connecting the scar subspace to generic states are smaller but of a similar magnitude to matrix elements between generic states, and v) in QMBS-C, the matrix elements connecting orbit states to generic states vanish exactly; this is to be expected as this is an exact scar model.

Even though QMBS-A/B states show strong revivals only in the chosen orbit states, an order by order examination of terms in the BCH expansion does not reflect this fact—indeed, the matrix elements between orbit states and generic states is of the same order as those connecting generic states. As alluded to above, it may be possible to reorganize the BCH expansion in terms of linear combinations of various C_n , such that we do see suppression of matrix elements (between orbit states and generic states). We have not attempted this, but note that a natural reason for the failure of BCH expansion to capture this phenomena may be because these models were designed to strongly obey rules of type I—breaking this rules implies that for some set of powers, the local unitaries corresponding to the automata do not commute; see Eq. (5.20). Since the local Hamiltonian is constructed as a linear combination of all powers of these local unitaries [Eq. (5.10)], the BCH terms will be non-zero at all orders as soon as any of the type I rules (defined by the set of powers of the local unitaries) are broken. Note that in QMBS-C, all rules of type I are satisfied, it is an exact scar model, and it is thus not surprising that BCH terms at all orders have no matrix element connecting the scar states and generic states.

The PXP model is different in that rules of type II can be enumerated naturally for

this model, given the rather simple form of the local Hamiltonian term, and most of these rules are satisfied. As a result, we expect the BCH expansion to be more useful in this case. Specifically, in the PXP model, the norm of BCH terms first *decreases* with n before eventually increasing. This is characteristic of the FM expansion for systems driven at high frequencies and which concomitantly possess a prethermal window over which an effective Floquet Hamiltonian can be obtained by truncating the FM expansion. We explore this in more detail next.

5.5.2 Prethermal behavior in the PXP model

An interesting phenomenon that can occur whenever a quantum system is driven is Floquet prethermalization, which describes a prethermal time window inside which the driven quantum system reaches a prethermal quasi-steady state before slowly drifting towards true equilibrium. In particular, the length of that prethermal time window goes as $e^{1/\tau}$ where τ is the driving period. Such a prethermal window is normally accompanied by the norm of BCH expansion terms $\|C_n\|$ first decreasing with n , up to some order n_0 , before increasing with n . The duration of the prethermal window is then $\mathcal{O}(e^{1/n_0})$. Such a pattern is naturally obtained in the case of high frequency driving, for instance when $U_F = e^{-iA\tau}e^{-iB\tau}$ for small τ , such that the lowest BCH terms largely decrease in n as $n\tau^n$. In a many-body setting, eventually, the number of terms in the commutator in C_n blows up as $n!$, which ultimately suppresses the decays from τ^n at $n_0 \approx O(1/\tau)$. As a corollary, one can truncate the BCH expansion to order n_0 and expect the truncated Hamiltonian to mimic the Floquet unitary dynamics up to times $\approx e^{n_0}$. In this case, $\tau = 1$, and one cannot expect a prethermal regime on account of the frequency of the drive. However, by enforcing the commutator of A, B to vanish on a subspace, one may expect a similar decrease of the norm of BCH terms before an eventual increase.

Indeed, as seen in Fig. 5.9, we do see that the amplitude of matrix elements connecting scar states to generic states decreases with the order of expansion n before again increasing. Thus, there is an effective, emergent, time period $T_{\text{eff}} < 1$ which we may attribute to the fact that BCH terms C_n , which are composed of nested commutators of A and B , are suppressed on the orbit subspace. Perhaps what is surprising is that the same behavior is in fact even

seen for matrix elements between generic states in the computational subspace.

The latter suggests that the prethermal dynamics may be applicable to not just the scar subspace, but to the full Hilbert space of the PXP model. To verify this, we examine the local autocorrelator, $|\langle Z_i(t) \rangle - \langle Z_i \rangle_{m.c.}|^2$, where $\langle Z_i \rangle_{m.c.}$ indicates the microcanonical average over a fixed energy window $\Delta E = 0.4$ centered around the average energy $E = \langle \psi | H | \psi \rangle$ and Z_i is the Pauli σ_z operator acting on a particular spin i of the system, which we choose arbitrarily.

Although many-body revivals of generic states decay rapidly, particularly in the PXP model, autocorrelations of local Z_i continue to have long time revivals in any state. One may attribute this to the presence of a prethermal window—the dynamics of spins due to the underlying Floquet automaton show revivals, and within the prethermal window, this behavior is mimicked by the truncated, strictly local, Floquet Hamiltonian which in this case is the PXP model.

To give further credence to this picture, we study the effect of adding the first few decreasing BCH terms to $H_{\text{eff}} = A + B = H_{\text{PXP}}$. We find that adding these terms in fact improves many-body revivals (both the revival strength and the regularity). Thus, one can think of the *absence* of such terms in the truncated Hamiltonian $A + B$ as a perturbation away from the quasi-local Floquet Hamiltonian which captures the dynamics of the ideal Floquet automaton most faithfully; these terms lead to decay of revivals; see Fig. 5.11.

Continuing with the analogy with Floquet systems driven at a high frequency and which exhibit a prethermalization window, we note the absence of terms $C_1, C_2, \dots, C_{n_0=6}$ in our truncated Hamiltonian $H_{\text{eff}} = A + B$ can lead to decay of many-body revivals. We estimate this revival time by computing a Fermi's Golden Rule rate of decay of a scar eigenstate of $H_{\text{eff}} = A + B$ into non-scarred states. This rate is given by the typical matrix element Γ in C_2 (which provides the largest coupling in the case of the PXP model; see Fig. 5.9) coupling this state to other states in the Hilbert space, multiplied by the number of states within an energy window Γ around this chosen scar state $\sim \Gamma/\delta$, where δ is the many-body level spacing. The term $\|(1 - P_0)C_2P_0\|^2 / (N_{\text{eff}}l)$ yields the norm squared

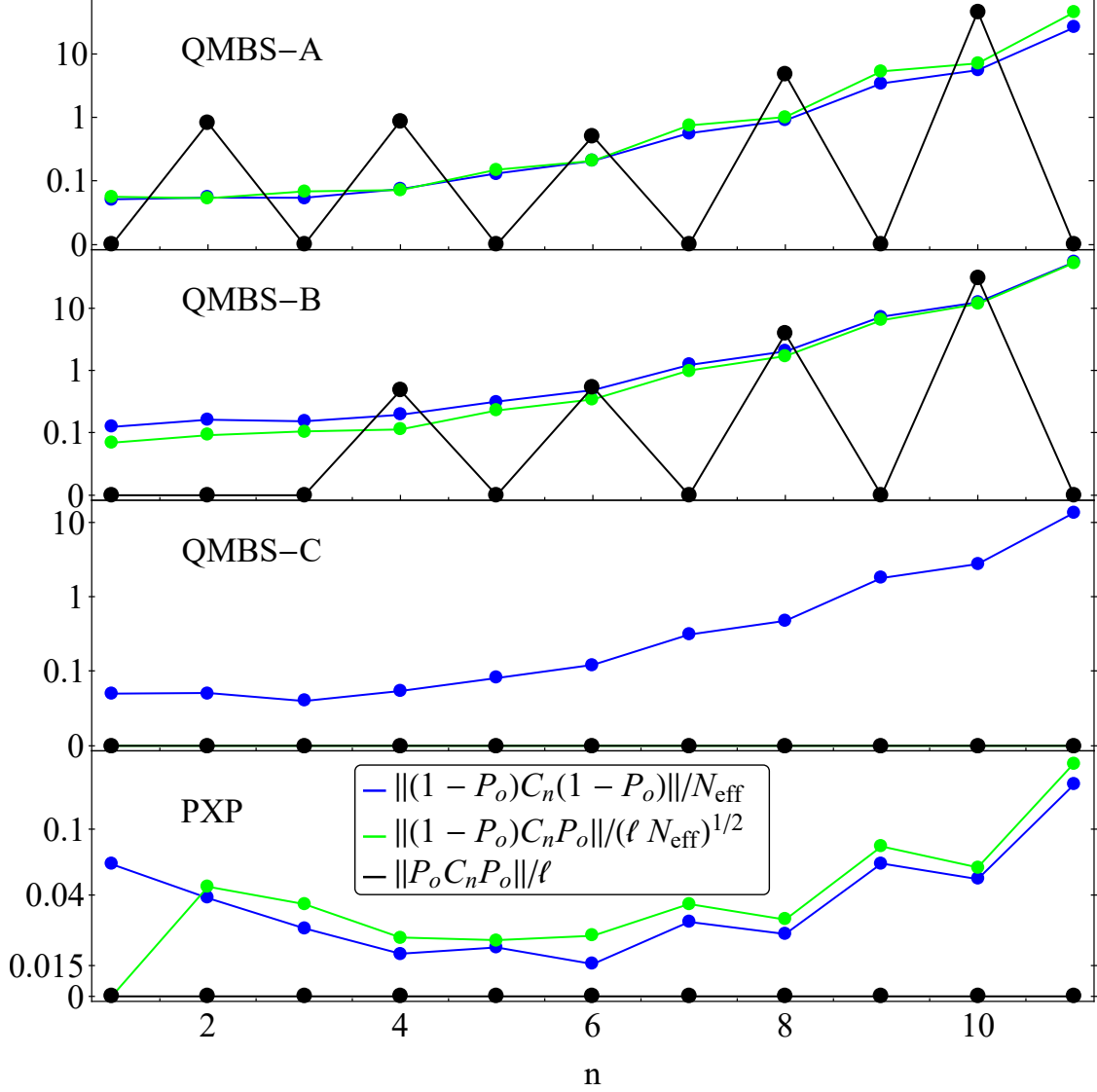


Figure 5.9: Leakage from orbit states, characterized by $\|(I - P_0)C_n P_0\|$ (green) and norm of the neglected terms C_n projected to the subspace of generic-states (blue) and orbit states (black). The amplitude of the BCH terms is normalized by the square-root of the number of matrix elements in the considered subspace, where l is the length of the orbit to preserve and N_{eff} is the number of computational basis states connected to the Néel state by a matrix elements of some given power of H . The C_n are computed from the Hamiltonian terms A and B in the basis of computational basis states that appear in the Krylov subspace except for QMBS-C for which the calculation was performed on the full Hilbert space for illustrating the embedding. $N_{\text{eff}} = 2207, 4096, 1366, 64$, $L = 16, 12, 12, 12$ for the PXP, QMBS-A, QMBS-B and QMBS-C model respectively. For the blue curve in QMBS-C, $N_{\text{eff}} = 4096 - 64$ is used.

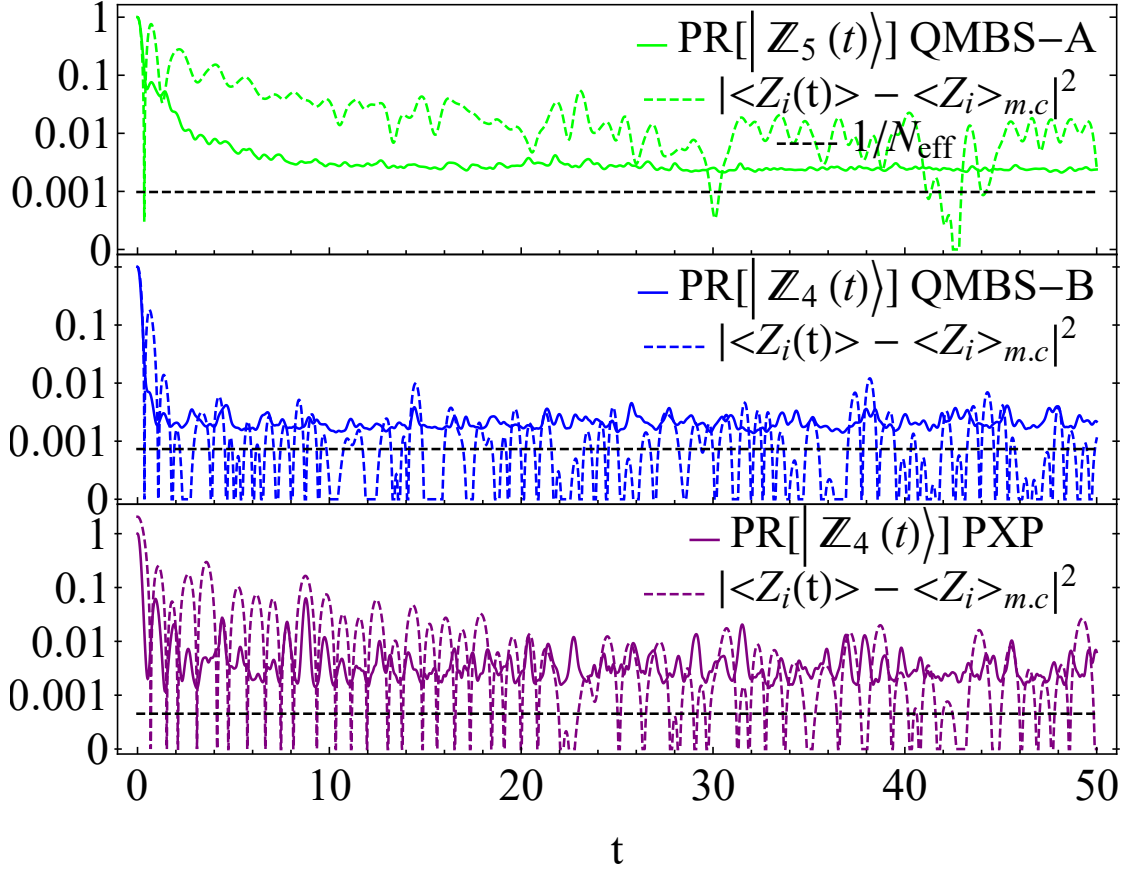


Figure 5.10: PR of generic states evolved in time and time evolution of $|\langle Z_i(t) \rangle - \langle Z_i \rangle_{m.c}|^2$ where $\langle Z_i \rangle_{m.c}$ is the micro-canonical average computed with an energy window ΔE of 0.4 centred around the average energy of the considered generic state. QMBS-A and PXP show signs of prethermalization which manifest themselves as a slow decay of $\langle Z_i(t) \rangle$ towards the micro-canonical average.

of a typical matrix element of the operator C_2 . To estimate the many-body level spacing, we note that the scar eigenstate does not couple to all states in the Hilbert space. Some of the C_i terms break full translational symmetry and parity, but S^2 , translation by two qubits, remains a conserved operator for all C_i . Thus, we can estimate the density of states $1/\delta$ within a given symmetry sector by $2N_{\text{eff}}/(L\Delta_{E_{\text{PXP}}})$ where $\Delta_{E_{\text{PXP}}} \approx 30$ is the bandwidth of the PXP model for $L = 16$. The approximate decay rate is then given by $1/\tau \approx 2\pi(2N_{\text{eff}}/(L\Delta_{E_{\text{PXP}}}))\|(1 - P_0)C_2P_0\|^2/(N_{\text{eff}}l) \approx 0.1$. This agrees approximately with an extrapolation of the numerical stimulated peak of many-body revivals to large times.

(Note that for the PXP model, the terms within the Néel subspace are also small for reasons of locality, which prevents C_n from leading to transitions between the Néel states) and symmetry (which prevents an energy offset between the Néel states due to particle-hole symmetry and translational symmetry in PXP). The latter likely aids stronger revivals and could be useful ingredients [29, 13] in searching for other approximate QMBS models using the methods outlined here.

5.5.3 BCH terms in the PXP model

We now examine these BCH terms for the PXP model in more detail. In particular, the first few orders are given by

$$\begin{aligned}
C_0 + C_1 + C_2 &= \left(-\frac{\pi}{2} + \frac{\pi^3}{96}\right) \sum_j P_j X_{j+1} P_{j+2} \\
&+ i\frac{\pi^2}{8} \sum_j (-1)^{j+1} (P_j S_{j+1}^+ S_{j+2}^- P_{j+3} - P_j S_{j+1}^- S_{j+2}^+ P_{j+3}) - \\
&\frac{\pi^3}{192} \sum_j (P_j X_{j+1} P_{j+2} Z_{j+3} + Z_j P_{j+1} X_{j+2} P_{j+3}) + \\
&\frac{\pi^3}{48} \sum_j (P_j S_{j+1}^+ S_{j+2}^- S_{j+3}^+ P_{j+4} + P_j S_{j+1}^- S_{j+2}^+ S_{j+3}^- P_{j+4}),
\end{aligned} \tag{5.22}$$

see App. F for a detailed derivation of this result. Note that up to support over 4 qubits, these corrections correspond to two terms, one which acts trivially on the orbit subspace,

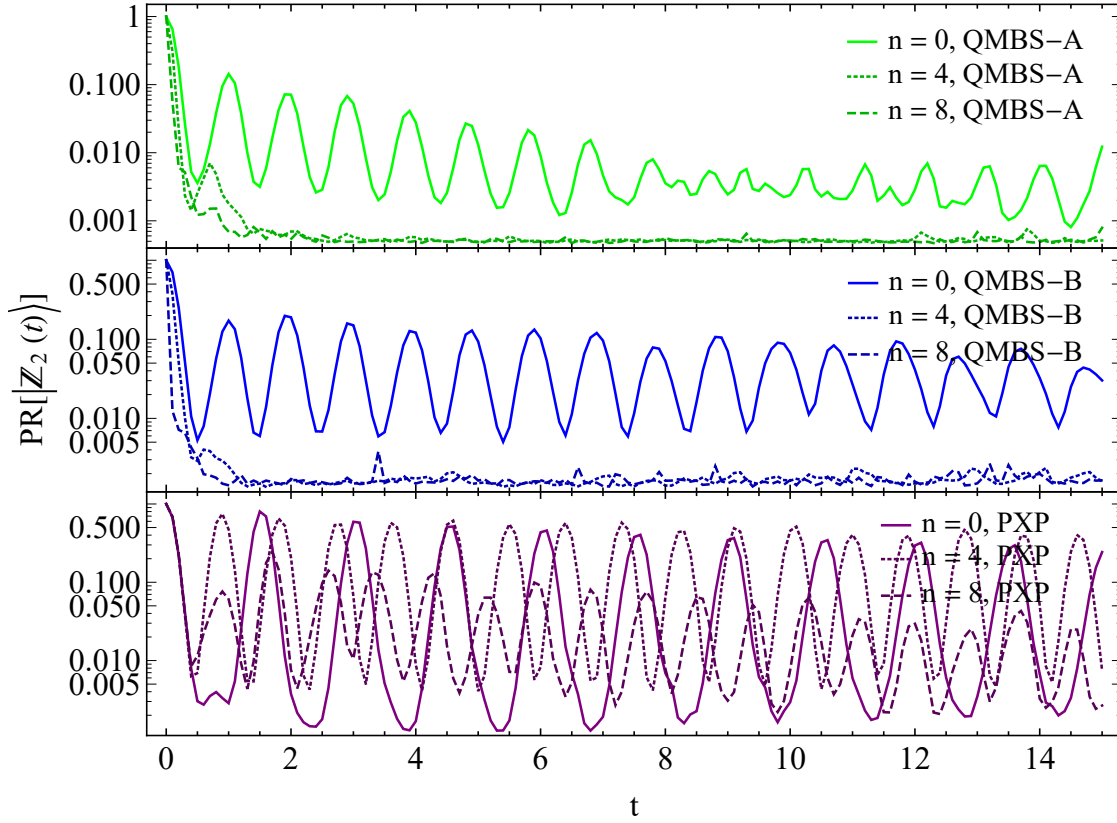


Figure 5.11: Revivals seen in models with additional BCH terms C_n added to $A+B$. Revivals improve when adding up to fifth order of BCH terms in the PXP model but worsen upon adding further higher orders. In contrast, revivals only decrease when adding further terms in QMBS-A/B. $L = 12, 12, 16$ for QMBS-A, QMBS-B and PXP respectively.

and the other, $(P_j X_{j+1} P_{j+2} Z_{j+3} + Z_j P_{j+1} X_{j+2} P_{j+3})$, was identified in both Refs. [29, 13] as a term that leads to better revivals and/or integrability of the model. This term was added to the PXP model with a variable amplitude which was optimized to improve integrability in Ref. [29] and revivals in Ref. [13]. Here the magnitude of these terms is obtained without numerical optimization, and is given by that obtained from the BCH expansion. The ratio of the amplitude of this term to the PXP term is ≈ 0.129 , which is about 6 times larger than that obtained in Ref. [29] and 2 times larger than that obtained in Ref. [13].

Finally, it is observed numerically that revivals in the PXP model improve upon adding BCH terms to an even order, while usually degrading upon adding terms to one additional order. This trend continues up to $n = 6$ after which revivals degrade with every successive order, see Fig. 5.11. This can be attributed to renewed divergence of the BCH terms in the scar subspace beyond $n = 6$.

5.5.4 PXP with and without phase

The phase that states accrue as they evolve under the Floquet automata can play a very important role. Fig. 5.12 highlights the stark difference in revival strength from automata with unitaries enforcing the same permutation but one in which the phase is trivial, and the second in which it is non-trivial. The second one corresponds to the usual PXP Hamiltonian. One can see that the former model exhibits smaller revivals which further corroborates the intuition that the amplitude of $\|(1 - P_o)C_n(P_o)\|$ is correlated with the strength of the revivals. For instance, the first leakage term fully vanishes in the PXP model, but it doesn't in the related model. (Note that a continuum of models between these two extremes was studied in [43],[44].)

5.6 Discussion and outlook

In this work, we show a method for engineering quantum many-body scar Hamiltonians by establishing a connection between quantum cellular automata $U_F = e^{-iA}e^{-iB}$ and the Hamiltonian $H = A + B$ obtained by carefully taking the matrix logarithm of each layer of U_F . Generally, the dynamics generated by U_F and H are unrelated. In particular, one can

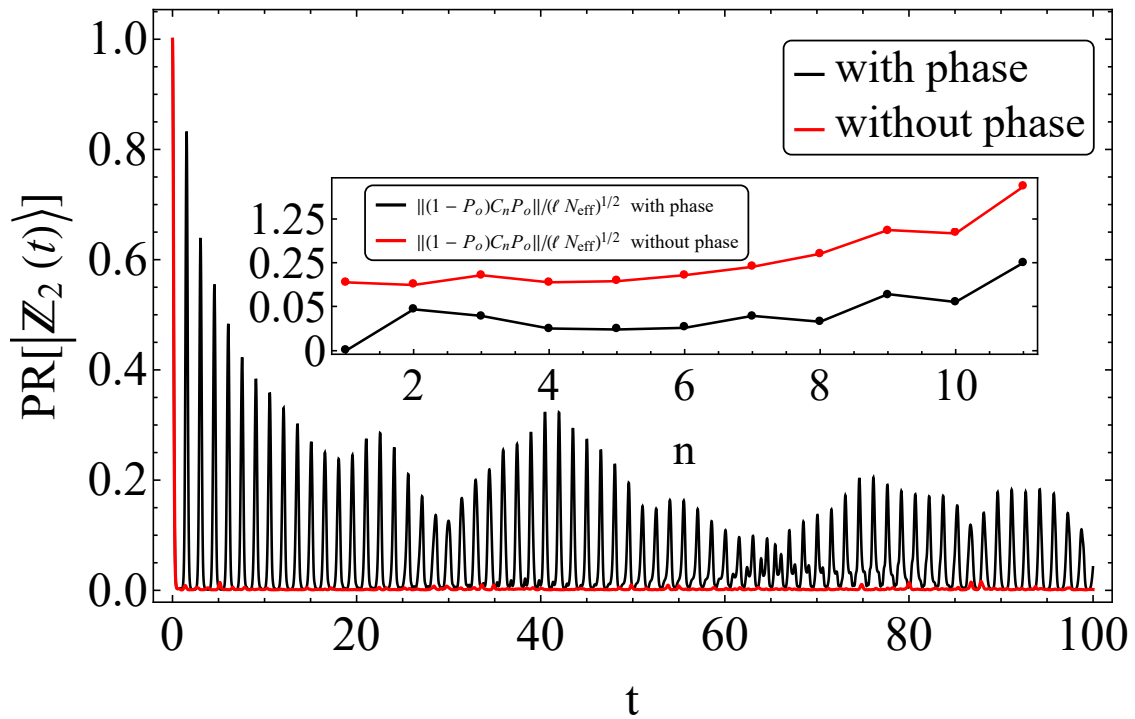


Figure 5.12: Overlap amplitude squared of $|Z_2\rangle$ with $e^{-i(A+B)t}|Z_2\rangle$ for models where phase is trivial vs non-trivial. Insets show how the effective leakage changes between models with trivial and non-trivial phase.

view H as a Hamiltonian obtained by truncating the BCH expansion $U_F = e^{-i(A+B)-iC_1-iC_2\dots}$ to zeroth order. Although for a generic interacting system, these terms C_n rapidly diverge, we devise two sets of rules, dubbed rules of type I and type II, that force these terms to vanish on a small subspace of states that are part of a cycle of U_F of finite length l .

We then construct models QMBS-A/B/C that successively satisfy more of the local rules of type I, which enforce that certain local commutators of the unitaries in U_F vanish on a cycle composed of the two Néel states. The PXP model is more naturally interpreted as satisfying a large number of rules of type II; these rules enforce that local commutators of the Hamiltonian vanish on a cycle of length 3 composed of the two Néel states and a vacuum state. The models QMBS-A/B/C satisfy successively more rules and exhibit concomitantly stronger revivals, with QMBS-C being an exact scar model.

We also examined, order by order, the typical matrix element in C_n connecting scar states to generic states. The amplitude of these terms is ideally heavily suppressed as it causes leakage from the scar subspace to generic states. We find that these terms decrease with increasing n in the PXP model, before again beginning to diverge at order $n_0 = 6$. This behavior is characteristic of prethermalization phenomena in Floquet systems driven at high frequencies. Although in this case the drive frequency is putatively 1, the observed behavior of the BCH terms suggests an emergent timescale $T_{\text{eff}} < 1$ and a prethermal window $\tau_p \sim e^{1/T_{\text{eff}}}$. In fact, even matrix elements of BCH terms connecting different generic states in the PXP model appear to show the same behavior. We find evidence of prethermal behavior in the PXP model by looking at autocorrelators of local spin Z_i . This operator shows revivals even in generic states, and long after many-body revivals of this generic state have decayed. We can also recover a timescale for decay of many-body revivals by computing a Fermi's Golden rule rate of decay based on the amplitude of matrix elements connecting orbit states to generic states in the BCH terms neglected.

The BCH expansion does not appear to be the correct way to understand leakage out of the scar subspace (and thus, many-body revivals) in the case of QMBS-A/B. Here, order by order, matrix elements connecting scar states to generic states can be of the same order as those connecting different generic states. This seems to contradict the fact that the orbit states are special and distinct from generic states because only these states show many-body

revivals. A natural explanation is that the BCH expansion may be reorganized in a way such that linear combinations of various C_n may have a small matrix element connecting orbit states to generic states even though individually the C_n have sizeable matrix elements. This requires further exploration.

We note that we may interpret the results of our work without directly appealing to Floquet automata. The rules devised effectively ensure that a putative scar Hamiltonian H can be decomposed into a partition $A+B$, where scar states are common eigenstates of A and B . If A and B are composed of physically disjoint terms, they naturally possess eigenstates of low entanglement. If $e^{inA} = e^{inB} = \mathbb{1}$, for some integer n , the eigenvalues of A and B are equidistant. Ensuring that commutators of A, B vanish on a certain (scar) subspace ensures that there exist a limited number (scaling at most polynomially in the system size L) of common eigenstates of A, B that are equidistant in energy. If we can somehow embed further low-entanglement states in this subspace, as we do, then one obtains a scar subspace of low-entanglement eigenstates.

In many ways, this work is a first step in leveraging the properties of non-thermal quantum cellular automata to construct quantum many-body scars. Some questions emerge naturally from this work. For instance, the choice of partitioning of the Hamiltonian into two parts A and B where A concerns the ‘even’ gates, and B the ‘odd’ gates is rather arbitrary. Nothing prevents one from choosing a different decomposition of H which would ultimately lead to a distinct automaton being associated with H . Provided this new automaton satisfies all or a large number of local rules for some specific states $|\psi\rangle$, it might be possible to identify additional quantum scar towers in the same model. We note here that in related work, we show that the mid-spectrum scar states in the AKLT model for instance can be obtained by considering various partitions of this model. Another interesting avenue for future work would be to study local unitary gates $U_{0,j}$ that are not simple permutation gates with phase. The construction presented here in principle applies to any unitary gate $U_{0,j}$ that satisfies the property $U_{0,j}^n = \mathbb{1}$ for some integer n regardless of the internal structure of $U_{0,j}$. Such an approach might lead to quantum scars with more complex structures. An interesting avenue for doing so would be to consider Clifford gates as the local unitary gates $U_{0,j}$ which, despite generating entanglement are entirely described by an underlying classical automaton which

acts as a permutation of the set of products of Pauli matrices rather than the computational basis states themselves.

5.7 Acknowledgements

The authors acknowledge useful discussions with Sarang Gopalakrishnan, Thomas Iadecola, Sanjaya Modugalya and Shivaji Sondhi. KA would like to acknowledge the hospitality of the Aspen Center for Physics where some of the ideas in this work were developed. PGR acknowledges graduate funding support from NSERC and FRQNT. MJG acknowledges support from the National Science Foundation (QLCI grant OMA-2120757). KA acknowledges funding support from NSERC, FRQNT, and the Tomlinson Scholar Award.

Chapter 6

Conclusion and outlook

In this work, an explicit method for weakly breaking the ETH by explicitly embedding scarred eigenstates in an otherwise thermalizing model was presented. As discussed in section 2, quantum scars come in a wide variety of shape and sizes.

The first example of quantum scars discussed in this work is the quantum Bunimovich stadium which showcases a non-trivial relationship between a quantum system and an underlying classical system that possesses unstable periodic orbits responsible for the emergence of quantum scars.

In the many-body setting, quantum scars can be the result of a multitude of different, but not necessarily mutually exclusive, phenomena. For example, the existence of a spectrum generating algebra, as described in 2.7, generates a set of scarred eigenstates by applying repeatedly a special operator Q^\dagger to a known eigenstate of H which is contained in a restricted linear subspace W of the Hilbert space. Spectrum generating algebras generate scarred eigenstates that are mutually separated in energy by a multiple of a constant energy spacing ΔE .

Another construction method that can be used to design QMBSs is the embedding method introduced in [58] which was discussed in 2.5. This method aims to embed special low-entangled eigenstates (i.e., scarred eigenstates) into an otherwise thermal spectrum, thereby

weakly or strongly breaking the ETH depending on the number of embedded non-thermal states.

Interestingly, there are also models, such as the PXP model, that have no known exact embedding or spectrum generating algebra. Instead, quantum scars in these models can be understood as the approximate conservation of a Krylov subspace. For example, this can be seen in the PXP model as the fact that the forward scattering approximation is almost exact when the initial state is one of the Néel states, which consequently produces an almost conserved subspace from which approximate scarred eigenstates of the Hamiltonian can be extracted. Remarkably, using matrix product state methods and the time-dependent variational principle, it was shown in [25] that PXP scars can alternatively be understood via a relation to the unstable orbits of an underlying classical system.

Finally, the presence of quantum scars can also be due to the proximity of a given model to an integrable parent model, as was discussed in section 2.4 where a nearly integrable parent model of the PXP model was introduced.

Systems with quantum scars generally exhibit unusual dynamical properties when the system is initialized in special highly excited low-entanglement states. This is due to the fact that the scarred eigenstates themselves usually have low-entanglement and thus generate a subspace of weakly entangled states. Generally, the scarred eigenstates have eigenvalues that are either exactly or approximately separated by some energy interval ΔE . This fact results in exact or approximate periodic dynamics provided the system is quenched in low entanglement states that lie within the scar subspace.

A setting where one can design strongly interacting many-body quantum systems with similar unusual dynamical properties is the setting of quantum cellular automata, where a quantum cellular automaton is defined as a local automorphism acting on the space of the algebra of quasi-local observables as defined in section 3. If the quantum cellular automaton is assumed to be composed of a two-layer circuit, with each layer constructed from individual

quantum gates $U_{0,j}$, then, provided that the local unitary gates $U_{0,j}$ are permutations, the whole Hilbert space can be decomposed into dynamically decoupled orbits. In this sense, this special class of quantum cellular automata do not thermalize. The question then becomes whether it is possible to convert such quantum cellular automata into Hamiltonian systems with the hope of transferring some of the non-thermal properties of the automaton to the Hamiltonian framework. This work boils down to an attempt to do the above.

As was shown in the main text, the connection established in this work between quantum cellular automata and quantum many body scars provides a novel approach to understanding and engineering approximate and exact quantum many-body scars. It was showed that there exist set of rules that either apply to the local Hamiltonian terms $h_{0,j}$ or to the unitary gates $U_{0,j}$ composing the automata. If (almost all) all the rules are satisfied, the static local Hamiltonian $A + B$ extracted from the automaton has (approximate)perfect revivals.

Because the automata considered here are derived from classical permutations, an exhaustive search was possible provided some degrees of freedom were fixed. Such a search revealed three models that satisfy progressively more rules. It was showed numerically that satisfying more rules of type II works towards making the revivals better. Crucially, one observes approximate revivals in models like QMBS-B without the need of any explicit small parameter λ controlling the strength of the revivals and is reminiscent of the celebrated PXP model. Furthermore, a calculation of the inverse participation ratio of the eigenstates versus the energy in the models QMBS-C, QMBS-B and QMBS-A revealed tower-like structures reminiscent of quantum scars.

Since the automata studied in this work can alternatively be interpreted as the dynamical evolution resulting from a Floquet driving protocol, it was also interesting to try to understand the properties of the system by making use of the Floquet prethermalization framework, which was discussed in section 4.2. Floquet prethermalization describes situations where the dynamics of the Floquet drive is approximated for an exponentially long time by an appropriately truncated Floquet Hamiltonian. If the amplitude of the BCH terms

first decreases before increasing, a prethermal regime may be observed. This result is used in this work to justify the relationship between the PXP model and its underlying automaton. Indeed, BCH terms computed in the PXP model first decrease up to a certain order n_0 before increasing which is a strong sign of Floquet prethermalization. Additionally, it was showed that some terms in the BCH expansion correspond to terms known to improve the revivals in the PXP model, thus further reinforcing the prethermalization picture.

In many ways, this work is a first step in leveraging properties of non-thermal quantum cellular automata to construct quantum many-body scars and a lot of interesting questions naturally emerged from this attempt. For instance, the choice of partitioning of the Hamiltonian into two parts A and B where A concerns the “even” gates, and B the “odd” gates is rather arbitrary. Nothing prevents one from choosing a different decomposition of H which ultimately leads to a distinct automaton being associated with H . Provided this new automaton satisfies all or a large number of local rules for some other states, one might be able to identify additional quantum scars. Furthermore, the decomposition of the Hamiltonian into two parts is also arbitrary. One might instead consider the decomposition $H = A+B+C$ and consider the automaton $e^{-iA}e^{-iB}e^{-iC}$. It would be interesting to determine what is the relevant set of local rules associated with automaton composed of more than 2 layers and if a distinct structure can allow one to find further quantum scars.

As another interesting avenue for future research, it might be interesting to study local unitary gates $U_{0,j}$ that are not simple permutation gates. The construction presented here in principle applies to any unitary gate $U_{0,j}$ that satisfies the property $U_{0,j}^n = I$ for some integer n regardless of the internal structure of $U_{0,j}$. Using more exotic quantum gates $U_{0,j}$ might lead for instance to quantum scars with more complex structures. It might also be interesting to consider Clifford gates as the local unitary gates $U_{0,j}$ which, despite generating entanglement, are ultimately described by an underlying classical automaton of the space of quasi-local local algebras (instead of the space of computational basis states).

Another interesting development would be to determine the analytical relation between the

timescale for the decay of the revivals and the number/type of rules satisfied. The results presented here are mostly qualitative in the sense that it was observed numerically that satisfying more rules improves revivals, but more rigorous results on the timescale for the decay would obviously be desirable. It would also be interesting to determine if there exists a fundamental difference between satisfying rules of type II versus rules of type I, for instance, it would be interesting to see if it is possible to associate a Floquet prethermalization picture with both type of rules.

In addition to the many open questions highlighted above, this work also suggests that quantum cellular automata and their unusual dynamical properties could be a powerful tool for studying various quantum systems. For example, quantum cellular automata might be particularly useful for analyzing fragmented [40] models, which host structures that appear quite similar in nature to the many disjoint cycles naturally arising from the U_F Floquet automaton studied in this work.

Appendix A

Permutation and phase map representation

In order to characterize the unitary matrices $U_{0,j}$ and their properties, it is convenient to introduce a compact way of representing them. Since the $U_{0,j}$ act as a permutation on the computational basis states on which they act as well as multiplying them by a phase, they can be represented using the cycle notation of a permutation as well as a phase map. One can associate the computational basis states with integers between 1 and 16 by converting their base 2 bit string representation to an integer, +1. Explicitly,

$$|0000\rangle \rightarrow |1\rangle \quad |0001\rangle \rightarrow |2\rangle \quad \dots \quad |1111\rangle \rightarrow |16\rangle. \quad (\text{A.1})$$

The state $|0\rangle$ is understood to be the +1 eigenstate of $2S_z$ and the $|1\rangle$ state is the -1 eigenstate of $2S_z$ where S_z is the standard z spin operator for a spin 1/2 particle. The phase map is represented by an array of length 16 $(\text{ph}_1, \text{ph}_2, \dots, \text{ph}_{16})$ with the understanding that the q^{th} component ph_q of this array is the complex number by which the q^{th} computational basis state is multiplied when acted upon by $U_{0,j}$, i.e $U_{0,j}|q\rangle = \text{ph}_q|\sigma(q)\rangle$, see Fig. 5.2. The transitions between computational basis states are represented with the cycle notation of a permutation, e.g if the permutation matrix $U_{0,j}$ generates the transitions $(1 \rightarrow 3 \rightarrow 8 \rightarrow 1)$, $(2 \rightarrow 4 \rightarrow 2)$ and sends all other states to themselves (possibly with a phase), then one can compactly represent the above transitions by $((1, 3, 8), (2, 4))$ where it is understood that consecutive integers n_i, n_{i+1} in a cycle (n_1, n_2, \dots, n_l) represent a transition from n_i to n_{i+1} .

The cycle is periodic in the sense that the last integer that appears in the cycle denoted above by n_l is mapped to n_1 . Any computational basis state that do not appear in a cycle is assumed to be mapped to itself.

Appendix B

Total number of relevant rules

Some of the rules that appear in Eq. 5.20 are trivially satisfied. Indeed, for the rules to be non-trivial, it must be the case that s_2 is non zero, and that at least one of s_1 or s_3 is non-zero. Most generally, this yields a total of $l(n-1)(n^2-1)(L/2)$ rules where l is the length of the cycle to be preserved and L is the system size. If the states $|\sigma^n(q)\rangle$ spanning the subspace to be protected are such that $S^2|\sigma^n(q)\rangle = |\sigma^n(q)\rangle$ where S is the operator translating all sites by one to the right, then the number of relevant rules is reduced to $l(n-1)(n^2-1)$ and is independent of system size. In the remainder of this work, for a given system, the number of satisfied rules is presented as a fraction of the total number of relevant rules, i.e. it will be presented as (Number of satisfied rules) / (Total number of relevant rules).

In the geometry where $U_F = \prod_i^{L/4} U_{0,4j-3} \prod_j^{L/4} U_{0,4j-1}$ and with P_0 composed of the two Néel states, one has a total number of relevant rules given by $l(n-1)(n^2-1)$ where $n = 6$, $l = 2$, so a total of 350 relevant rules. The PXP model is special since the local Hamiltonian has the property that $h_{0,j}^3 = \frac{\pi^2}{4} h_{0,j}$, so it is worth considering rules of type II instead. The total number of relevant rules of type II for the PXP model is given by $(n-1)(n^2-1) + (n-1)(n^2-1)2$ with $n = 3$, so a total of 48 rules. The first term counts the rules associated with the fully polarized state $|1111\dots\rangle$, the second term counts all the rules associated with the state $|1010\dots\rangle$. Note that since the Néel states are such that $|1010\dots\rangle = S|0101\dots\rangle$, one directly obtains that satisfying all the rules for one of the two Néel states (taking into account that the Néel states are not translationally invariant) ensures that the rules are satisfied for the other Néel state as well, so no additional rules

need to be taken into account.

Appendix C

Decomposing Hamiltonian's in terms of powers of simple unitary matrices

The coefficients c_k that appear in Eq. 5.10 can be found by writing Eq. 5.10 with a set of orthonormal eigenvectors. Doing so, one obtains

$$\sum_{s=1}^{2^4} -\tilde{\beta}_s |\beta_s\rangle \langle \beta_s| = \sum_{s=1}^{2^4} \left(\sum_{k=1}^n e^{ik\beta_s} c_k \right) |\beta_s\rangle \langle \beta_s| \quad (\text{C.1})$$

where $|\beta_s\rangle$ is an eigenstate of U_F with eigenvalue β_s . This yields the matrix equation

$$M\vec{c} = -\vec{\beta}, \quad M_{s,k} = e^{ik\beta_s}, \quad (\text{C.2})$$

$$s \in \{1, 2, \dots, 2^4\}, \quad k \in \{1, 2, \dots, n\}$$

with $\vec{c} = (c_1, c_2, \dots, c_n)$ and $\vec{\beta} = (\tilde{\beta}_1, \tilde{\beta}_2, \dots, \tilde{\beta}_{2^4})$. In this form, it is not obvious that Eq. C.2 always admits a solution, but it turns out that a solution does indeed always exist.

To construct it, consider the following set of states

$$\sum_{k=0}^{n-1} e^{i\alpha_k} U_{0,j}^k |q\rangle \quad (\text{C.3})$$

for some set of real numbers α_k . Note that since n is such that $U_{0,j}^n = \mathbb{1}$, this sequence of states is a closed loop upon successive applications of U_F . It is easy to see that the choice $\alpha_k = -k\gamma$, where γ is one of the n roots of unity, yields an eigenstate of U_F with eigenvalue $e^{i\gamma}$. Note that all the generated eigenstates produced by Eq. C.3 for a given $|q\rangle$

have distinct eigenvalues and are thus orthogonal, but Eq. 5.2 suggests that one should only be finding l eigenstates where l is the length of the cycle. Furthermore, eigenstates built from different cycles are necessarily orthogonal to each other since they contain different computational basis states. For this to be possible, it must be the case that some of the eigenstates produced with C.3 are equal to the vector $\vec{0}$. One can deduce from the previous sections that the only non-zero eigenstates will be the ones for which γ is given by $\gamma = \frac{\Phi + 2\pi m}{l}$, see Eq. 5.3. The redundant eigenstates can safely be added to the eigenstate decomposition of $U_{0,j}$ and $i \log U_{0,j}$ just like if they were non-zero vectors which is key to solving for the vector \vec{c} . Doing so yields

$$\begin{aligned} & \sum_{s=1}^{nN_{\text{Cycles}}} -\tilde{\gamma}_s |\gamma_s\rangle \langle \gamma_s| = \\ & \sum_{s=1}^{nN_{\text{Cycles}}} \left(\sum_{k=1}^n e^{ik\gamma_s} c_k \right) |\gamma_s\rangle \langle \gamma_s| \end{aligned} \quad (\text{C.4})$$

where $|\gamma_s\rangle$ are eigenstates of $U_{0,j}$ with eigenvalue $e^{i\gamma_s}$ now also including the redundant eigenstates. $\tilde{\gamma}_s$ is equal to $-i$ times the principal logarithm of $e^{i\gamma_s}$ and N_{Cycles} is the total number of cycles composing $U_{0,j}$. From this, one obtains the matrix equation

$$\begin{aligned} \Gamma \vec{c} &= -\vec{\gamma} & \Gamma_{s,k} &= e^{ik\gamma_s} \\ s &\in \{1, 2, \dots, nN_{\text{Cycles}}\} & k &\in \{1, 2, \dots, n\} \end{aligned} \quad (\text{C.5})$$

with $\vec{c} = (c_1, c_2, \dots, c_n)$, $\vec{\gamma} = (\tilde{\gamma}_1, \tilde{\gamma}_2, \dots, \tilde{\gamma}_{nN_{\text{Cycles}}})$. Remarkably, $\frac{\Gamma^\dagger}{nN_{\text{cycles}}}$ is an inverse of Γ

$$\begin{aligned} \frac{(\Gamma^\dagger \Gamma)_{k,m}}{nN_{\text{cycles}}} &= \sum_{s=1}^{nN_{\text{cycles}}} \frac{\Gamma_{s,k}^* \Gamma_{s,m}}{nN_{\text{Cycles}}} \\ &= \sum_{s=1}^{nN_{\text{cycles}}} \frac{e^{-i\gamma_s(k-m)}}{nN_{\text{Cycles}}} = \delta_{k,m} \end{aligned} \quad (\text{C.6})$$

To see why Eq. C.6 is valid, note that the sum over s runs over the augmented eigenvalues γ_s associated with each cycle composing $U_{0,j}$. k and m both take values between 1 and n , so their difference $k - m$ takes values in the range $[-n + 1, n - 1]$. γ_s is one of the n roots of unity modulo 2π . One can then decide to order the eigenvalues by choosing $\gamma_s = \frac{2\pi s}{n}$, $s \in \{1, 2, \dots, nN_{\text{cycles}}\}$ where say the n first eigenvalues are associated with the first cycle,

the n next with the second cycle, so on and so forth. Eq. C.6 then reads

$$\begin{aligned}
& \frac{1}{nN_{\text{cycles}}} \sum_{s=1}^{nN_{\text{cycles}}} e^{-i\frac{2\pi s(k-m)}{n}} \\
&= \frac{N_{\text{cycles}}}{nN_{\text{cycles}}} \sum_{s=1}^n e^{-i\frac{2\pi s(k-m)}{n}} \\
&= \frac{1}{n} \left(\frac{1 - e^{2\pi(k-m)(n+1)/n}}{1 - e^{2\pi(k-m)/n}} - 1 \right)
\end{aligned} \tag{C.7}$$

which always yields 0 provided $(k - m)$ is not a multiple of n . As seen above, $(k - m)$ takes values in the range $[-n + 1, n - 1]$, so one obtains an indeterminate result only when $k = m$, in which case it can directly be seen that the result is 1. This implies that the coefficients c_k are given by

$$\vec{c} = \frac{\Gamma^\dagger}{nN_{\text{Cycles}}} \vec{\gamma} \tag{C.8}$$

which provides an explicit method for decomposing $i \log(U_{0,j})$ as a linear superposition of powers of $U_{0,j}$. Remarkably, the vector \vec{c} only depends on the order of the unitary matrix n , so distinct unitary matrices with the same order n assume the same decomposition.

Appendix D

QMBS-C as an embedded spectrum generating algebra

The full Hamiltonian corresponding to the model QMBS-C is given by

$$H = \sum_{j=1}^{L/2} \left(\frac{\pi}{2} P_{2j} X_{2j} X_{2j+1} P_{2j} + \right. \\ \left. (1 - P_{2j}) H_{\text{ext},2j-1} (1 - P_{2j}) - \frac{\pi}{2} I \right) \quad (\text{D.1})$$

with $P_{j+1} = (I - Z_{j+1} Z_{j+2})/2$. $H_{\text{ext},j}$ is given in Tab. [H.1](#), but the exact form of $H_{\text{ext},j}$ turns out to be irrelevant. Let's begin by showing that [D.1](#) is an embedded model. Note first that the set of projectors P_{2j} and the Hamiltonian all mutually commute, a state of the system can thus be an eigenstate of all P_{2j} simultaneously. This fact allows one to directly connect the model [D.1](#) to the embedding method presented in [\[58\]](#). The arbitrary Hamiltonian terms h_j correspond to $H_{\text{ext},j}$ and the Hamiltonian H' is $\sum_j \frac{\pi}{2} P_{2j} X_{2j} X_{2j+1} P_{2j}$. For a state $|\psi\rangle$ to be a +1 eigenstate of the P_{2j} , it must be the case that qubits sitting on sites $2j, 2j+1$ have opposite spin. The subspace spanned by such states has dimension $2^{L/2}$ and includes for instance the two Néel states. The effective Hamiltonian acting on this subspace is given by

$$H_{\text{eff}} = \sum_{j=1}^{L/2} \left(\frac{\pi}{2} X_{2j} X_{2j+1} - \frac{\pi}{2} I \right) \quad (\text{D.2})$$

which is obtained by setting all P_{2j} to I . The full Hamiltonian H hosts a spectrum generating algebra, see Ref. [37] for an introduction to the topic. Indeed, consider the operator

$$Q^\dagger = \sum_{j=1}^{L/2} Z_{2j}(I - X_{2j}X_{2j+1}) \quad (\text{D.3})$$

and consider the linear subspace W spanned by the $2^{L/2}$ states that are in the common $+1$ eigenspace of the P_{2j} . This operator can be seen to be responsible for a spectrum generating algebra. Indeed one has that

$$([H, Q^\dagger] - \epsilon Q^\dagger)W = 0 \quad (\text{D.4})$$

which follows from

$$\begin{aligned} & [H, Q^\dagger]W \\ &= \sum_{j=1}^{L/2} \left[\frac{\pi}{2} P_{2j} X_{2j} X_{2j+1} P_{2j}, Z_{2j}(I - X_{2j}X_{2j+1}) \right] W \\ &= \pi \sum_{j=1}^{L/2} Z_{2j}(I - X_{2j}X_{2j+1})W = \pi Q^\dagger W \end{aligned} \quad (\text{D.5})$$

where the second equality comes from $(I - P_{2j})W = 0$, $P_{2j}W = W$ and $Q^\dagger W \subset W$. One can see from the above that $\epsilon = \pi$. This shows that QMBS-C hosts a spectrum generating algebra. QMBS-C is thus an example of a model where one observes an embedded spectrum generating algebra in an otherwise fully thermal Hamiltonian.

Appendix E

Symmetry sectors of QMBS-A/B

The relevant symmetries of the QMBS-B and QMBS-A model are invariance under S^2 and invariance under the unitary operator

$$U_{SM} = \left(\prod_{i=1}^L X_i \right) SM \quad (\text{E.1})$$

where S is the operator that shifts all sites by one to the right and M is the mirror operation about the center bond. Furthermore, both models possess the anti-unitary symmetry RSM where R is the complex conjugation operation, which implies time reversal symmetry (which explains why the GOE ensemble is the best fit for $P(r)$). In order to compute the R-statistic, one must restrict the Hamiltonian to a given symmetry sector, which is chosen in this case to be the common $+1$ eigenspace of S^2 and U_{SM} , which for instance contains the state $\frac{1}{\sqrt{2}}(|1010\dots\rangle + |0101\dots\rangle)$. Furthermore, one must also restrict the Hamiltonian to the set of computational basis states that appear in the Krylov subspace associated with the Néel states. For QMBS-B, one can see that the local Hamiltonian $h_{0,j}$ can only lower or increase the total spin $Z_{\text{tot}} = \sum_i Z_i$ by multiples of three, see Tab. H.1. Thus, the total number of accessible computational basis states starting from the Néel state is given by the set of all computational basis states that have a total spin Z_{tot} which is separated from $Z_{\text{tot}} = 0$ by some multiple of 3 (the Néel states are such that $Z_{\text{tot}} = 0$). In QMBS-A, no such restrictions exist. In QMBS-C, the total number of accessible states from the Néel states is given by $2^{L/2}$, see App. D for a more precise definition. Finally, the PXP model is restricted to the well known Fibonacci subspace [63]. The effective dimension N_{eff} is defined here as the

number of computational basis states connected to the Néel state by a matrix elements of some given power of H . It is given here for all the models studied in this work.

$$\begin{aligned}
N_{\text{eff,PXP}} &= F_{L+1} + F_{L-1} \\
N_{\text{eff,QMBS-A}} &= 2^L \\
N_{\text{eff,QMBS-B}} &= \sum_{k=-\lfloor L/3 \rfloor}^{\lfloor L/3 \rfloor} \frac{L!}{(\frac{L}{2} + 3k)! (\frac{L}{2} - 3k)!} \\
N_{\text{eff,QMBS-C}} &= 2^{L/2}
\end{aligned} \tag{E.2}$$

where F_n is the n^{th} Fibonacci number and L is the system size. Note that the above is only well defined for even system sizes, the Néel states do not exist otherwise.

Appendix F

Exact PXP BCH terms

The first order BCH term C_1 is given by

$$-\frac{i}{2}[A, B] = \sum_{j \in \text{odd}, k \in \text{even}} -\frac{i}{2}[h_j, h_k] \quad (\text{F.1})$$

Note that h_j and h_k commute unless $k = j - 1$ or $k = j + 1$ which yields

$$[A, B] = -\frac{i}{2} \sum_{j \in \text{odd}} ([h_j, h_{j-1}] + [h_j, h_{j+1}]). \quad (\text{F.2})$$

This can be rewritten as

$$\begin{aligned} [A, B] &= -\frac{i}{2} \sum_{j \in \text{odd}} [h_j, h_{j+1}] + \frac{i}{2} \sum_{j \in \text{even}} [h_j, h_{j+1}] = \\ &\quad -\frac{i}{2} \sum_j (-1)^{i+1} [h_j, h_{j+1}] \end{aligned} \quad (\text{F.3})$$

which shows that the first order correction $[A, B]$ yields the same term on even and odd sites, but with an alternating sign. Let's now compute the matrix form of $[h_j, h_{j+1}]$. One readily obtains that the only non-zero matrix elements resulting from this computation are the following transitions

$$\begin{aligned} |1011\rangle &\rightarrow -\frac{\pi^2}{4} |1101\rangle \\ |1101\rangle &\rightarrow \frac{\pi^2}{4} |1011\rangle \end{aligned} \quad (\text{F.4})$$

all other computational basis states are mapped to 0. Recall that the class of possible deformations introduced in [29] are

$$\begin{aligned}
& \sum_j Z_j \quad \sum_j Z_j Z_{j+2} \quad \sum_j Z_j Z_{j+3} \\
& \sum_j P_{j-1} X_j P_{j+1} \quad \sum_j P_{j-1} Y_j P_{j+1}, \\
& \sum_j P_{j-1} X_j P_{j+1} Z_{j+2} \quad \sum_j Z_{j-2} P_{j-1} X_j P_{j+1} \\
& \sum_j P_{j-1} Y_j P_{j+1} Z_{j+2} \quad \sum_j Z_{j-2} P_{j-1} Y_j P_{j+1} \\
& \sum_j P_{j-1} S_j^+ S_{j+1}^- P_{j+2} \quad \sum_j P_{j-1} S_j^- S_{j+1}^+ P_{j+2}
\end{aligned} \tag{F.5}$$

The above commutator can be written as

$$[h_j, h_{j+1}] = -\frac{\pi^2}{4} (P_j S_{j+1}^+ S_{j+2}^- P_{j+3} - h.c.) \tag{F.6}$$

which yields for the first order BCH term

$$C_1 = \frac{i\pi^2}{8} \sum_j (-1)^{j+1} (P_j S_{j+1}^+ S_{j+2}^- P_{j+3} - h.c.) \tag{F.7}$$

Note that the above makes it explicit that the first commutator vanishes when acting on the orbit states and is a consequence of the first order rules being respected in PXP. Next, consider higher order terms in the expansion that act non-trivially on only 4 qubits. Using the notation $\alpha_j = -\frac{\pi^2}{4} (P_j S_{j+1}^+ S_{j+2}^- P_{j+3} - P_j S_{j+1}^- S_{j+2}^+ P_{j+3})$ one can write the second order term as

$$C_2 = -\frac{1}{12} ([A, \sum_j (-1)^{j+1} \alpha_j] - [B, \sum_j (-1)^{j+1} \alpha_j]) \tag{F.8}$$

This expression can be recast as

$$-\frac{1}{12} [\sum_j (-1)^{j+1} h_j, \sum_k (-1)^{k+1} \alpha_k] \tag{F.9}$$

Focusing only on terms with support on 4 qubits, one obtains the terms

$$-\frac{1}{12} \sum_j ([h_j, \alpha_j] - [h_{j+1}, \alpha_j]) \tag{F.10}$$

Computing first $[h_j, \alpha_j]$ one obtains that the non zero matrix elements produce the transitions

$$\begin{aligned} |1111\rangle &\rightarrow -\frac{\pi^3}{8} |1101\rangle \\ |1101\rangle &\rightarrow -\frac{\pi^3}{8} |1111\rangle \end{aligned} \quad (\text{F.11})$$

and all other matrix elements vanish. This implies that

$$[h_j, \alpha_j] = \frac{\pi^3}{16} (-P_{j+1}X_{j+2}P_{j+3} + Z_jP_{j+1}X_{j+2}P_{j+3}) \quad (\text{F.12})$$

The second term gives

$$[h_{j+1}, \alpha_j] = \frac{\pi^3}{16} (P_jX_{j+1}P_{j+2} - P_jX_{j+1}P_{j+2}Z_{j+3}) \quad (\text{F.13})$$

By combining the results, one finds that the terms with support on 4 qubits for the second order term in the BCH expansion are

$$\begin{aligned} -\frac{\pi^3}{192} \sum_i &(-P_{j+1}X_{j+2}P_{j+3} + P_jX_{j+1}P_{j+2}Z_{j+3} \\ &-P_jX_{j+1}P_{j+2} + Z_jP_{j+1}X_{j+2}P_{j+3}) \end{aligned} \quad (\text{F.14})$$

One can complete the above calculation by also computing terms that will have support on 5 qubits which are given by

$$-\frac{1}{12} \sum_j (-[h_{j-1}, \alpha_j] + [h_{j+2}, \alpha_j]) \quad (\text{F.15})$$

It can be seen that first the term $[h_{j-1}, \alpha_j]$ produces the following transitions

$$\begin{aligned} |10101\rangle &\rightarrow \frac{\pi^3}{8} |11011\rangle \\ |11011\rangle &\rightarrow \frac{\pi^3}{8} |10101\rangle \end{aligned} \quad (\text{F.16})$$

The other term $[h_{j+2}, \alpha_j]$ yields the same transitions, but with an added minus sign on both transition which yields for the terms with support on 5 qubits

$$\frac{\pi^3}{8} \frac{1}{6} \sum_j (P_jS_{j+1}^+S_{j+2}^-S_{j+3}^+P_{j+4} + h.c) \quad (\text{F.17})$$

Up to second order, one thus obtains for the BCH expansion

$$\begin{aligned}
C_0 + C_1 + C_2 &= \left(-\frac{\pi}{2} + \frac{\pi^3}{96}\right) \sum_j P_j X_{j+1} P_{j+2} \\
&+ i \frac{\pi^2}{8} \sum_j (-1)^{j+1} (P_j S_{j+1}^+ S_{j+2}^- P_{j+3} - P_j S_{j+1}^- S_{j+2}^+ P_{j+3}) - \\
&\frac{\pi^3}{192} \sum_j (P_j X_{j+1} P_{j+2} Z_{j+3} + Z_j P_{j+1} X_{j+2} P_{j+3}) + \\
&\frac{\pi^3}{48} \sum_j (P_j S_{j+1}^+ S_{j+2}^- S_{j+3}^+ P_{j+4} + P_j S_{j+1}^- S_{j+2}^+ S_{j+3}^- P_{j+4})
\end{aligned} \tag{F.18}$$

F.0.1 Classification of the BCH terms

The BCH terms obtained from the PXP model can be classified according to which symmetries they respect. The PXP model has three important symmetries which are inversion symmetry about the central bound, time reversal symmetry and a particle-hole like symmetry due to anti-commutation with the operator $\mathcal{P} = \prod_i Z_i$.

The first order BCH term $[A, B]$ yields $\frac{i}{2} \frac{\pi^2}{4} \sum_j (-1)^{j+1} (P_j S_{j+1}^+ S_{j+2}^- P_{j+3} - \text{h.c.})$ which vanishes on the orbit subspace. This term breaks inversion symmetry, time reversal symmetry and doesn't anti-commute with \mathcal{P} .

The second order BCH terms is composed of two terms. The first one with support on 4 qubits takes the form $-\frac{1}{24} \frac{\pi^3}{8} \sum_j (P_j X_{j+1} P_{j+2} Z_{j+3} + Z_j P_{j+1} X_{j+2} P_{j+3})$. Such a term respects all symmetries and was shown to improve revivals [13] and integrability [29]. The second term with support on 5 qubits is given by $\frac{1}{6} \frac{\pi^3}{8} \sum_i (P_j S_{j+1}^+ S_{j+2}^- S_{j+3}^+ P_{j+4} + \text{h.c.})$. This term also respects all symmetries. Note that both these terms act non-trivially on the orbit subspace.

Appendix G

Closing condition for $h_{0,j}$

Provided the fact that there exist an integer n such that $U_{0,j}^n = \mathbb{1}$ and given the decomposition of $h_{0,j}$ in terms of powers of $U_{0,j}$

$$h_{0,j} = \sum_{k=0}^{n-1} c_k U_{0,j}^k \quad (\text{G.1})$$

it is natural to ask if the local Hamiltonian's $h_{0,j}$ satisfy a closing relation similar to the $U_{0,j}$ closing relation. More precisely, does there exist an integer m such that

$$h_{0,j}^m = \sum_{k=0}^{m-1} \alpha_k h_{0,j}^k \quad (\text{G.2})$$

which would restrict the total number of rules of type II one needs to satisfy in order to obtain QMBS phenomenology. First, consider the decomposition of $h_{0,j}^m$ in terms of powers of $U_{0,j}^k$

$$h_{0,j}^s = \sum_{k=0} c_k^{(s)} U_{0,j}^k \quad (\text{G.3})$$

where $c_k^{(s)}$ denotes the coefficients associated with the s^{th} power of $h_{0,j}$ and $h_{0,j}^0 \equiv I$. It is straightforward to see that the coefficients $c_k^{(s)}$ for $1 \leq s$ are given explicitly by

$$M^{s-1} \vec{c} = \begin{pmatrix} c_0^{(s)} \\ c_1^{(s)} \\ \vdots \\ c_{n-1}^{(s)} \end{pmatrix} \quad (\text{G.4})$$

where

$$M = \begin{pmatrix} c_0 & c_{n-1} & \dots & c_2 & c_1 \\ c_1 & c_0 & c_{n-1} & \dots & c_2 \\ \vdots & & \ddots & & \vdots \\ c_{n-1} & c_{n-2} & c_{n-3} & \dots & c_0 \end{pmatrix} \quad \vec{c} = \begin{pmatrix} c_0 \\ c_1 \\ \vdots \\ c_{n-1} \end{pmatrix} \quad (\text{G.5})$$

It is a known fact that for any matrix M of size l by l , then one has that M^l can always be written as a linear superposition of smaller powers of the matrix M . This has the important implication that there exist a set of coefficients α_k such that

$$h_{0,j}^n = M^n \vec{c} = \sum_{k=0}^{n-1} \alpha_k M^k \vec{c} = \sum_{k=0}^{n-1} \alpha_k h_{0,j}^k \quad (\text{G.6})$$

which shows that the local Hamiltonian $h_{0,j}$ closes on itself once the power n is reached.

Appendix H

Spin representation of the models

The spin representation of the model QMBS-A/B/C and the PXP model is presented in this section using the convention

$$\begin{aligned} Z|1\rangle &= -|1\rangle & Z|0\rangle &= |0\rangle \\ S^+|0\rangle &= |1\rangle & S^-|1\rangle &= |0\rangle \end{aligned} \tag{H.1}$$

One has $X = 2S_x$, $Y = 2S_y$ and $Z = 2S_z$ where S_j are the standard spin operators acting on a spin 1/2 particle.

QMBS-A	
Permutation	((3, 13, 11, 7, 9, 5), (4, 14, 12, 8, 10, 6))
Phase	(1,1,1,1,1,1,1,1,1,1,1,1,1,1,1)
$h_{0,j}$ decomposition	$(\frac{\pi}{6} + i\frac{\pi}{2\sqrt{3}})U_{0,j} + (-\frac{\pi}{6} - i\frac{\pi}{6\sqrt{3}})U_{0,j}^2 + \frac{\pi}{12}U_{0,j}^3 - \frac{\pi}{12}U_{0,j}^0 + \text{h.c}$
$U_{0,j}$ spin representation	$(S_j^+ S_{j+1}^+ S_{j+2}^- + S_j^+ S_{j+1}^- S_{j+2}^-) + \left(\frac{(I - Z_j)}{2} S_{j+1}^- S_{j+2}^+ + S_j^- S_{j+1}^+ \frac{(I - Z_{j+2})}{2} \right)$ $+ (S_j^- S_{j+1}^+ \frac{(I + Z_{j+2})}{2} + \frac{(I + Z_j)}{2} S_{j+1}^- S_{j+2}^+) + (S_j^+ S_{j+1}^+ S_{j+2}^+ + S_j^- S_{j+1}^- S_{j+2}^-)^2$
QMBS-B	
Permutation	((1, 15), (2, 16), (3, 9, 5), (4, 10, 6), (7, 13, 11), (8, 14, 12))
Phase	(1,1,1,1,1,1,1,1,1,1,1,1,1,1,1)
$h_{0,j}$ decomposition	$(\frac{\pi}{6} + i\frac{\pi}{2\sqrt{3}})U_{0,j} + (-\frac{\pi}{6} - i\frac{\pi}{6\sqrt{3}})U_{0,j}^2 + \frac{\pi}{12}U_{0,j}^3 - \frac{\pi}{12}U_{0,j}^0 + \text{h.c}$
$h_{0,j}$ spin representation	$\frac{\pi}{4}(S_j^+ S_{j+1}^+ S_{j+2}^- + S_j^- S_{j+1}^- S_{j+2}^-) + i\frac{4\pi}{6\sqrt{3}}(S_j^- S_{j+1}^+ + S_{j+1}^- S_{j+2}^+ + S_{j+2}^- S_j^+)$ $-\frac{\pi P_j}{4} + \text{h.c}$ $P_j = (S_j^+ S_{j+1}^+ S_{j+2}^+ + S_j^- S_{j+1}^- S_{j+2}^-)^2$
QMBS-C	
Permutation	((3, 5), (4, 6), (7, 15, 9), (8, 16, 10), (11, 13), (12, 14))
Phase	(1,1,1,1,1,1,1,1,1,1,1,1,1,1,1)
$h_{0,j}$ decomposition	$(\frac{\pi}{6} + i\frac{\pi}{2\sqrt{3}})U_{0,j} + (-\frac{\pi}{6} - i\frac{\pi}{6\sqrt{3}})U_{0,j}^2 + \frac{\pi}{12}U_{0,j}^3 - \frac{\pi}{12}U_{0,j}^0 + \text{h.c}$
$h_{0,j}$ spin representation	$\frac{\pi}{2}P_{j+1}X_{j+1}X_{j+2}P_{j+1} + (I - P_{j+1})H_{\text{ext},j}(I - P_{j+1}) - \frac{\pi}{2}I,$ $H_{\text{ext},j} = i\frac{4\pi}{6\sqrt{3}}(K_{j+1} + (I - K_{j+1})X_j)(K_j + (I - K_j)X_{j+1}X_{j+2}) + \frac{\pi}{4}I + \text{h.c}$ $P_{j+1} = (I - Z_{j+1}Z_{j+2})/2, \quad K_j = (I + Z_j)/2$
PXP	
Permutation	((11, 15), (12, 16))
Phase	(1,1,1,1,1,1,1,1,1,1,i,i)
$h_{0,j}$ decomposition	$(\frac{\pi}{4} + i\frac{\pi}{4})U_{0,j} - \frac{\pi}{8}U_{0,j}^2 - \frac{\pi}{8}I + \text{h.c}$
$h_{0,j}$ spin representation	$-\frac{\pi}{2}P_j X_{j+1} P_{j+2}, \quad P_j = (I - Z_j)/2$

Table H.1: Spin representation of the models

Bibliography

- [1] Dmitry Abanin, Wojciech De Roeck, Wen Wei Ho, and François Huveneers. A rigorous theory of many-body prethermalization for periodically driven and closed quantum systems. *Communications in Mathematical Physics*, 354(3):809–827, 2017.
- [2] Ian Affleck, Tom Kennedy, Elliott H Lieb, and Hal Tasaki. Rigorous results on valence-bond ground states in antiferromagnets. In *Condensed Matter Physics and Exactly Soluble Models*, pages 249–252. Springer, 2004.
- [3] Kartiek Agarwal, Ehud Altman, Eugene Demler, Sarang Gopalakrishnan, David A Huse, and Michael Knap. Rare-region effects and dynamics near the many-body localization transition. *Annalen der Physik*, 529(7):1600326, 2017.
- [4] Kartiek Agarwal and Ivar Martin. Dynamical enhancement of symmetries in many-body systems. *Physical Review Letters*, 125(8):080602, 2020.
- [5] Y. Y. Atas, E. Bogomolny, O. Giraud, and G. Roux. Distribution of the ratio of consecutive level spacings in random matrix ensembles. *Phys. Rev. Lett.*, 110:084101, Feb 2013.
- [6] D.M. Basko, I.L. Aleiner, and B.L. Altshuler. Metal-insulator transition in a weakly interacting many-electron system with localized single-particle states. *Annals of Physics*, 321(5):1126 – 1205, 2006.
- [7] Hannes Bernien, Sylvain Schwartz, Alexander Keesling, Harry Levine, Ahmed Omran, Hannes Pichler, Soonwon Choi, Alexander S Zibrov, Manuel Endres, Markus

- Greiner, et al. Probing many-body dynamics on a 51-atom quantum simulator. *Nature*, 551(7682):579–584, 2017.
- [8] Ola Bratteli and Derek W. Robinson. *Operator Algebras and Quantum Statistical Mechanics*. Springer Berlin Heidelberg, 1997.
- [9] Marin Bukov, Luca D’Alessio, and Anatoli Polkovnikov. Universal high-frequency behavior of periodically driven systems: from dynamical stabilization to floquet engineering. *Advances in Physics*, 64(2):139–226, 2015.
- [10] L. A. Bunimovich. On the ergodic properties of nowhere dispersing billiards. *Communications in Mathematical Physics*, 65(3):295 – 312, 1979.
- [11] W J Caspers, K M Emmett, and W Magnus. The majumdar-ghosh chain. twofold ground state and elementary excitations. *Journal of Physics A: Mathematical and General*, 17(13):2687–2696, sep 1984.
- [12] John T Chalker. Spin liquids and frustrated magnetism. *Topological Aspects of Condensed Matter Physics: Lecture Notes of the Les Houches Summer School: Volume 103, August 2014*, 103:123, 2017.
- [13] Soonwon Choi, Christopher J. Turner, Hannes Pichler, Wen Wei Ho, Alexios A. Michailidis, Zlatko Papić, Maksym Serbyn, Mikhail D. Lukin, and Dmitry A. Abanin. Emergent SU(2) dynamics and perfect quantum many-body scars. *Physical Review Letters*, 122(22):220603, June 2019.
- [14] J. M. Deutsch. Quantum statistical mechanics in a closed system. *Phys. Rev. A*, 43(4):2046–2049, 1991.
- [15] J H Conway E R Berlekamp and R K Guy. *Winning Ways for Your Mathematical Plays, Volume 2*. Academic Press, London, 1982.
- [16] J. Eisert, M. Cramer, and M. B. Plenio. Colloquium: Area laws for the entanglement entropy. *Rev. Mod. Phys.*, 82:277–306, Feb 2010.

- [17] G.Bard Ermentrout and Leah Edelstein-Keshet. Cellular automata approaches to biological modeling. *Journal of Theoretical Biology*, 160(1):97–133, January 1993.
- [18] Terry Farrelly. A review of quantum cellular automata. *Quantum*, 4:368, nov 2020.
- [19] Michael E Fisher. Statistical mechanics of dimers on a plane lattice. *Physical Review*, 124(6):1664, 1961.
- [20] Glenn H Fredrickson and Hans C Andersen. Kinetic ising model of the glass transition. *Physical review letters*, 53(13):1244, 1984.
- [21] M. Girardeau. Relationship between systems of impenetrable bosons and fermions in one dimension. *Journal of Mathematical Physics*, 1(6):516–523, 1960.
- [22] Sarang Gopalakrishnan and Bahti Zakirov. Facilitated quantum cellular automata as simple models with non-thermal eigenstates and dynamics. *Quantum Science and Technology*, 3(4):044004, 2018.
- [23] Eric J. Heller. Bound-state eigenfunctions of classically chaotic hamiltonian systems: Scars of periodic orbits. *Phys. Rev. Lett.*, 53:1515–1518, Oct 1984.
- [24] Christopher L Henley. The “coulomb phase” in frustrated systems. *Annu. Rev. Condens. Matter Phys.*, 1(1):179–210, 2010.
- [25] Wen Wei Ho, Soonwon Choi, Hannes Pichler, and Mikhail D. Lukin. Periodic orbits, entanglement, and quantum many-body scars in constrained models: Matrix product state approach. *Phys. Rev. Lett.*, 122:040603, Jan 2019.
- [26] David A. Huse, Rahul Nandkishore, and Vadim Oganesyan. Phenomenology of fully many-body-localized systems. *Phys. Rev. B*, 90:174202, Nov 2014.
- [27] Thomas Iadecola and Sagar Vijay. Nonergodic quantum dynamics from deformations of classical cellular automata. *Phys. Rev. B*, 102:180302(R), Nov 2020.
- [28] Josef Jäckle and Siegfried Eisinger. A hierarchically constrained kinetic ising model. *Zeitschrift für Physik B Condensed Matter*, 84(1):115–124, 1991.

- [29] Vedika Khemani, Chris R. Laumann, and Anushya Chandran. Signatures of integrability in the dynamics of rydberg-blockaded chains. *Physical Review B*, 99(16):161101(R), April 2019.
- [30] Hyungwon Kim, Tatsuhiko N. Ikeda, and David A. Huse. Testing whether all eigenstates obey the eigenstate thermalization hypothesis. *Phys. Rev. E*, 90:052105, Nov 2014.
- [31] Toshiya Kinoshita, Trevor Wenger, and David S. Weiss. A quantum newton's cradle. *Nature*, 440(7086):900–903, April 2006.
- [32] Katja Klobas, Bruno Bertini, and Lorenzo Piroli. Exact thermalization dynamics in the “rule 54” quantum cellular automaton. *Physical Review Letters*, 126(16):160602, 2021.
- [33] Tomotaka Kuwahara, Takashi Mori, and Keiji Saito. Floquet–magnus theory and generic transient dynamics in periodically driven many-body quantum systems. *Annals of Physics*, 367:96–124, 2016.
- [34] Tim Langen, Thomas Gasenzer, and Jörg Schmiedmayer. Prethermalization and universal dynamics in near-integrable quantum systems. *Journal of Statistical Mechanics: Theory and Experiment*, 2016(6):064009, June 2016.
- [35] Achilleas Lazarides, Arnab Das, and Roderich Moessner. Periodic thermodynamics of isolated quantum systems. *Physical Review Letters*, 112(15), April 2014.
- [36] Achilleas Lazarides, Arnab Das, and Roderich Moessner. Fate of many-body localization under periodic driving. *Phys. Rev. Lett.*, 115:030402, Jul 2015.
- [37] Daniel K. Mark, Cheng-Ju Lin, and Olexei I. Motrunich. Unified structure for exact towers of scar states in the affleck-kennedy-lieb-tasaki and other models. *Phys. Rev. B*, 101:195131, May 2020.
- [38] Takashi Mori. Floquet resonant states and validity of the floquet-magnus expansion in the periodically driven friedrichs models. *Physical Review A*, 91(2), February 2015.

- [39] Takashi Mori, Tomotaka Kuwahara, and Keiji Saito. Rigorous bound on energy absorption and generic relaxation in periodically driven quantum systems. *Physical review letters*, 116(12):120401, 2016.
- [40] Sanjay Moudgalya, B Andrei Bernevig, and Nicolas Regnault. Quantum many-body scars and hilbert space fragmentation: a review of exact results. *Reports on Progress in Physics*, 85(8):086501, jul 2022.
- [41] Sanjay Moudgalya, Stephan Rachel, B Andrei Bernevig, and Nicolas Regnault. Exact excited states of nonintegrable models. *Physical Review B*, 98(23):235155, 2018.
- [42] Sanjay Moudgalya, Nicolas Regnault, and B. Andrei Bernevig. η -pairing in hubbard models: From spectrum generating algebras to quantum many-body scars. *Phys. Rev. B*, 102:085140, Aug 2020.
- [43] Bhaskar Mukherjee, Sourav Nandy, Arnab Sen, Diptiman Sen, and K. Sengupta. Collapse and revival of quantum many-body scars via floquet engineering. *Physical Review B*, 101(24):245107, June 2020.
- [44] Bhaskar Mukherjee, Arnab Sen, Diptiman Sen, and K. Sengupta. Dynamics of the vacuum state in a periodically driven rydberg chain. *Physical Review B*, 102(7):075123, August 2020.
- [45] Rahul Nandkishore and Sarang Gopalakrishnan. General theory of many body localized systems coupled to baths. *arXiv preprint arXiv:1606.08465*, 2016.
- [46] Nicholas O’Dea, Fiona Burnell, Anushya Chandran, and Vedika Khemani. From tunnels to towers: Quantum scars from lie algebras and q -deformed lie algebras. *Phys. Rev. Research*, 2:043305, Dec 2020.
- [47] Arijeet Pal and David A. Huse. Many-body localization phase transition. *Phys. Rev. B*, 82:174411, Nov 2010.
- [48] Richard G Palmer, Daniel L Stein, Elihu Abrahams, and Philip Warren Anderson. Models of hierarchically constrained dynamics for glassy relaxation. *Physical Review Letters*, 53(10):958, 1984.

- [49] Marcos Rigol, Vanja Dunjko, and Maxim Olshanii. Thermalization and its mechanism for generic isolated quantum systems. *Nature (London)*, 452(7189):854–858, 2008.
- [50] Marcos Rigol, Vanja Dunjko, Vladimir Yurovsky, and Maxim Olshanii. Relaxation in a completely integrable many-body quantum system: An ab initio study of the dynamics of the highly excited states of 1d lattice hard-core bosons. *Phys. Rev. Lett.*, 98:050405, Feb 2007.
- [51] Felix Ritort and Peter Sollich. Glassy dynamics of kinetically constrained models. *Advances in physics*, 52(4):219–342, 2003.
- [52] Pierre-Gabriel Rozon, Michael J. Gullans, and Kartiek Agarwal. Constructing quantum many-body scar hamiltonians from floquet automata. *Phys. Rev. B*, 106:184304, Nov 2022.
- [53] Angelo Russomanno, Alessandro Silva, and Giuseppe E. Santoro. Periodic steady regime and interference in a periodically driven quantum system. *Physical Review Letters*, 109(25), December 2012.
- [54] Roberto H. Schonmann. On the behavior of some cellular automata related to bootstrap percolation. *The Annals of Probability*, 20(1), January 1992.
- [55] Michael Schreiber, Sean S. Hodgman, Pranjal Bordia, Henrik P. Lüschen, Mark H. Fischer, Ronen Vosk, Ehud Altman, Ulrich Schneider, and Immanuel Bloch. Observation of many-body localization of interacting fermions in a quasirandom optical lattice. *Science*, 349(6250):842–845, 2015.
- [56] Maksym Serbyn, Dmitry A Abanin, and Zlatko Papić. Quantum many-body scars and weak breaking of ergodicity. *Nature Physics*, 17(6):675–685, 2021.
- [57] Dan Shemesh. Common eigenvectors of two matrices. *Linear Algebra and its Applications*, 62:11–18, 1984.
- [58] Naoto Shiraishi and Takashi Mori. Systematic construction of counterexamples to the eigenstate thermalization hypothesis. *Phys. Rev. Lett.*, 119:030601, Jul 2017.

- [59] Jacob Smith, Aaron Lee, Philip Richerme, Brian Neyenhuis, Paul W Hess, Philipp Hauke, Markus Heyl, David A Huse, and Christopher Monroe. Many-body localization in a quantum simulator with programmable random disorder. *Nature Physics*, 12(10):907–911, 2016.
- [60] J. A. Somers. Direct simulation of fluid flow with cellular automata and the lattice-boltzmann equation. *Applied Scientific Research*, 51(1-2):127–133, June 1993.
- [61] Mark Srednicki. Chaos and quantum thermalization. *Phys. Rev. E*, 50(2):888–901, 1994.
- [62] Bill Sutherland. *Beautiful models: 70 years of exactly solved quantum many-body problems*. World Scientific, 2004.
- [63] C. J. Turner, A. A. Michailidis, D. A Abanin, Maksym Serbyn, and Z Papić. Quantum scarred eigenstates in a rydberg atom chain: Entanglement, breakdown of thermalization, and stability to perturbations. *Physical Review B*, 98(15):155134, 2018.
- [64] Christopher J Turner, Alexios A Michailidis, Dmitry A Abanin, Maksym Serbyn, and Zlatko Papić. Weak ergodicity breaking from quantum many-body scars. *Nature Physics*, 14(7):745–749, 2018.
- [65] J. von Neumann. *Theory of Self-Replicating Automata*. University of Illinois Press, Champaign, Illinois, 1966.
- [66] Joseph W. P. Wilkinson, Katja Klobas, Tomaž Prosen, and Juan P. Garrahan. Exact solution of the floquet-PXP cellular automaton. *Physical Review E*, 102(6):062107, December 2020.
- [67] Stephen Wolfram. Cellular automata as models of complexity. *Nature*, 311(5985):419–424, 1984.